Winter 12-1-2011

Strength of Polycrystalline Ceramics under Shock Compression

Jianbin Zhu
University of Nebraska-Lincoln, zhu_jianbin@yahoo.com

STRENGTH OF POLYCRYSTALLINE CERAMICS

UNDER SHOCK COMPRESSION

by

Jianbin Zhu

A DISSERTATION

Presented to the Faculty of

The Graduate College at University of Nebraska

In Partial Fulfillment of Requirements

For the Degree of Doctor of Philosophy

Major: Engineering (Engineering Mechanics)

Under the Supervision of Professor Ruqiang Feng

Lincoln, Nebraska

December, 2011

STRENGTH OF POLYCRYSTALLINE CERAMICS UNDER SHOCK COMPRESSION

Jianbin Zhu, Ph.D.

University of Nebraska, 2011

Advisor: Ruqiang Feng

Determinations of Some polycrystalline ceramics' strength properties and inelastic deformation mechanisms in the shocked state are critically important to the design and optimization of armor structures involving these materials. In this work, multiscale modeling and simulations have been carried out to study strength of the effects of polycrystalline microstructure, crystal anisotropy, porosity, and their interactions with microscopic deformation/damage mechanisms on the responses of several polycrystalline ceramics under shock compression and to extract their shock strengths from the wave profiles measured in the related plate impact shock wave experiments.

With a mesoscopic computational model, the roles of intragranular microplasticity and deformation twinning, intergranular microdamage, and voids in the inelastic deformations and shock strengths of two polycrystalline α–phase aluminum oxides, Lucalox and AD995 have been examined. The results show that microplasticity by combined (primary) prismatic and (secondary) basal slips can well capture the characteristic features observed experimentally for shocked Lucalox. For AD995, the results show that porosity has a much more significant role than glassy grain boundaries in causing its lower shock strength than Lucalox. Its shock response can be well modeled by a combination of void-induced intense basal twinning and prismatic slip. The

mesoscopic model has also been used to extract from the available experimental data the crystal elasticity and plasticity properties of aluminum oxynitride (AlON).

At the macroscopic level, a homogeneous continuum model, which combines nonlinear elasticity and pressure-dependent plasticity for effective strength description has been proposed. A procedure for determining the material parameters via matching the model simulations with the available shock wave profile measurements has been demonstrated for AlON and for a polycrystalline α–6H silicon carbide (SiC-N).

Finally, a new finite element piezoresistance model for interpreting the measurement of a manganin stress gauge has been developed and calibrated with the longitudinal gauge measurements obtained in the shock-compressed SiC-N. The calibrations for the gauge in both the longitudinal and lateral configurations have been obtained. This enables the determination of ceramic shock strength directly from the gauge measurements in the two configurations.

ACKNOWLEDGEMENTS

It has been a long and difficult journey for the completion of my dissertation and subsequent Ph.D. There are many individuals who have been instrumental in helping me. No words can adequately express my appreciation and my love, and I will be forever grateful to all of you for believing in me and helping me realize this dream.

First and foremost I want to thank my advisor Dr. Ruqiang Feng, for his professional guidance, patience, flexibility, genuine caring and concern, and faith in me during the dissertation process when I am attending to life while also earning my Ph.D. I appreciate all his contributions of time, ideas, and funding to make my Ph.D. experience productive and stimulating.

I would like to thank my reading committee members: Dr. Joseph A. Turner, and Dr. Florin Bobaru for their time, interest, and helpful comments. I would also like to thank the other two members of my oral defense committee, Dr. Mehrdad Negahban, and Dr. Zhaoyan Zhang for their time and insightful questions.

I would also like to thank all the people who were involved in this research and my study at the University of Nebraska-Lincoln: Dongmei Zhang, Chaojun Wang, Ashwani Kumar Goel, and Yun Zeng. I appreciate the assistance offered by Ms. Kathie Hiatt.

I would like to acknowledge the support provided by the U.S. Army Research Office and Laboratory. Without them, the completion of this project may never have been realized.

Thanks also to my mother, Tongxiu Zhang, and my father, Xiemin Zhu. They have taught me about hard work and self-respect, about persistence and about how to be independent. Mom, especially, was a great role model of resilience, strength and character. Both have always expressed how much they love me. Thanks for instilling in me the importance of a good education and for taking away any excuse to fail. I love you.

And finally, I want to thank my wife, Minong, and my children, Mingyin and Samuel, for many years of support and encouragement as I completed this life-long goal. Thank you for your unwavering faith, patience, understanding, love, and commitment to me over the years. You are my constant sources of strength and hope. I am grateful that we share our lives together, forever. I love you.

TABLE OF CONTENTS

LIST OF FIGURES

LIST OF TABLES

CHAPTER 1

INTRODUCTION

1.1 Background and Motivation

Over the past 20 years high performance ceramic materials developed to the point where they are able to replace metals in many applications, such as military armors, automobile defense, cutting tools, turbine blade coatings, fuel rods, space, and aeronautical industries. Compared with metals, ceramics have low densities and very high compressive strengths, superior hardness, corrosion and wear resistances, and high melting temperature. The unique combination of light weight and extremely high effective strength under shock compression has made some polycrystalline ceramics excellent candidates for advanced armor applications. These typical polycrystalline ceramics include two polycrystalline α-phase aluminum oxides (α-Al_2O_3), Lucalox (99.9% pure and dense) and AD995 (99.5% pure and 97% dense), polycrystalline aluminum oxynitride (AlON), and ploycrystalline silicon carbide (SiC). Compressive strengths of these ceramics are critically important to ceramic armor design**.** However, when shocked beyond the elastic limit, these materials lose tensile strength indicating

complex deformation/damage mechanisms in the inelastically shocked materials. Determinations of their strength properties and inelastic deformation mechanisms in the shocked state are also critically important to the design and optimization of armor structures involving these materials.

Typically, the popular experimental techniques for measuring the dynamic strength response of ceramics under shock loading conditions are plate impact shock wave experiments (e.g., Gust and Royce, 1971; Kipp and Grady, 1989; Feng et al., 1998). In the previous researches, such experiment had been carried out to investigate the compressive strength response of these polycrystalline ceramics.

The dynamic stress-wave response of polycrystalline α-Al_2O_3 (Lucalox) was measured under the shock loading to about 16GPa by the plate impact experiment (Munson and Lawrence, 1979), in which it is shown that the Hugoniot elastic limit (HEL) of polycrystalline α-Al_2O_3 is 9.1GPa. In the previous study in our group, the compressive strength of polycrystalline α–Al_2O_3 had been analyzed by Zhang (2005) by using a 100-grain square polycrystal model, and the result showed that the simulated macroscopic compressive strength response compared well with the experimental measurement by considering material model of nonlinear elastic and crystal plasticity with slip systems of basal and pyramidal slips. However a question of the slip systems that are used in the study comes out because some researchers show that prismatic slip is more important and easily activated than pyramidal slip (Cadoz et al., 1984; Heuer et al., 1998). Thus a further analysis whether the compressive strength response of polycrystalline α–Al_2O_3

changes or not when pyramidal slip is replaced by prismatic slip is needed to carry out tp answer the question.

Coors AD995, another type α–phase aluminum oxides with 99.5% pure and 97% dense, is an armor material relatively cheap to produce. The dynamic strength response of polycrystalline AD995 has been obtained (Dandekar & Bartowski, 1993; Reinhart & Chhabildas, 2003). However, the measurement shows that it has a lower strength than Lucalox , 15-30% reduction in the Hugoniot elastic limit (HEL) and more significant reduction in the post-HEL strength (Dandekar & Bartowski, 1993; Reinhart & Chhabildas, 2003). It is not yet clear whether it is caused by glassy grain boundaries, or voids, or something else**.** To understand the causes of the reduction, it is necessary to examine the roles of microplasticity, glassy grain boundaries and voids in the inelastic deformations and the strength of polycrystalline AD995 and to develop an exact polycrystal model with voids for the analysis.

Shock compression of AlON has been reported by Cazamias et al. (2001) to 15 GPa, by Vaughan et al.(2001) to 21 GPa, by Sekine et al. (2003) from 61 to 180 GPa, and by Thornhill et al.(2006) from 5-89 GPa. These studies included the Hugoniot Elastic Limit (HEL), Hugoniot measurements to 180 GPa and phase transition, shear strength, and spall strength. In recent year, the plate impact experiments of AlON were performed by Thornill et al. (2006). The wave form profile of interface particle velocity has been measured and the compression stresses have been analyzed by jump condition method. However, the results of longitudinal stress and mean stress are conflicting. The strength of polycrystalline AlON is still not clear. In addition, what are the strength properties of

polycrystalline AlON to describe the material inelastic deformation? Hence, modeling and simulation of the strength of polycrystalline AlON is also necessary.

Piezoresistance gauges have been used extensively in shock wave research, primarily for longitudinal stress measurement, since the early 1960s. Both experimental and analytical studies have been carried out to understand the electromechanical response of manganin gauge. In particular, the studies by Gupta and co-workers have provided a fairly complete phenomenological model for piezoresistance response and the methodologies to evaluate the model constants. Thus, the gauge resistance change can be calculated quite accurately if the mechanical state of the gauge is known and the model constants have been determined. However, the interest in using piezoresistance gauges in shock wave experiments is motivated by the reverse problem: determination of a particular stress component in the sample from the measured resistance change history (Feng, Gupta and Wong, 1997). To calibrate the longitudinal gauge measurements obtained in the shock-compressed SiC-N, it is necessary to develop a new finite element piezoresistance model for interpreting the measurement of a commercial manganin stress gauge embedded in a plate impact target.

In summary, polycrystalline ceramics are very important materials for advanced structural engineering purposes. The compressive strength response of ceramics is important for characterizing and modeling the material inelastic deformation at high stresses and high strain rates. The understanding of the compression strength and the study of strength properties and the mechanism of material inelastic deformation for

polycrystalline ceramics are still far from satisfactory. The specific outstanding scientific issues that motivate this dissertation research are as follows:

(1) How do the polycrystalline microstructure and the different activated slip systems for general plastic deformation in ceramic crystals influence the strength of polycrystalline α-Al_2O_3?

(2) What is the difference between the inelastic deformation of shocked AD995 and that of shocked α-Al_2O_3? What are the roles of microplasticity, glassy grain boundaries and voids in the inelastic deformation and strength of polycrystalline AD995? Which one is the dominant factor of the 15-30% reduction in the HEL and more signification reduction in the post-HEL strength?

(3) What is the shock strength response of polycrystalline ALON? What are the strength properties and the base of elastic constants for polycrystalline ALON?

(4) What is a new finite element piezoresistance model for interpreting the measurement of a commercial manganin stress gauge embedded in a plate impact target?

1.2 Objectives

The goal of this work is to gain good understanding of the strengths of polycrystalline ceramics and the inelastic deformation in these materials by investigating the compressive strengths of polycrystalline ceramics under shock compression. To address the above scientific issues, detailed analysis with physics-based material

modeling and topologically accurate numerical simulation is required. Accordingly, two sets of research objectives are identified.

The first set of objectives is aimed at the development of a computational modeling methodology that enables micromechanical analysis of polycrystalline ceramics with topologically accurate microstructural modeling:

(1) To develop a microstructural model that simulates explicitly the microstructure of polycrystalline ceramics, and a meshing technique that generates microstructure-preserving numerical meshes to enable the use of numerical solutions such as the finite element (FE) method for detailed micromechanical analysis.

(2) To develop material models and related numerical algorithms that can accurately and efficiently capture the nonlinear anisotropic crystal elasticity and in-grain crystal plasticity that may be encountered in the micromechanical analyses of interest.

The second set of objectives is aimed at understanding of the micromechanisms governing the inelastic deformations of two ceramics, polycrystalline AD995 alumina and ALON under quasistatic uniaxial-strain compression:

(1) To determine whether or not microplasticity by limited slip systems can induce significant macroscopic inelastic deformations of polycrystalline AD995 alumina under uniaxial-strain compression.

(2) To examine the roles of porosity and weak boundary in the deformations, of polycrystalline AD995 alumina during shock compression.

(3) To develop a good understanding of the shock strength of ALON and determine the material properties and elastic constants of polycrystalline ALON.

Finally, a new finite element piezoresistance model for interpreting the measurement of a commercial manganin stress gauge embedded in a plate impact target is developed and calibrated with the longitudinal gauge measurements obtained in the shock-compressed SiC-N.

1.3 Technical Approaches and Significance

Voronoi polycrystal is a widely used topologically accurate microstructure model for analyzing the micromechanical behavior of polycrystalline ceramics (Kumar et al., 1996). In this work, an algorithm of developing Voronoi tessellation by Xue (2003) is adopted for the microstructural modeling. Two-dimensional (2-D) Voronoi cells with boundary layers and with or without porosity are constructed within a square plate. Three-dimensional (3-D) Voronoi cells without boundary layers are constructed within a cubic space. Voronoi cells with randomly assigned crystallographic orientations represent the aggregate of Voronoi polycrystal (Zhang et al., 2005).

The FE mesh generation follows grain-wise meshing approach. For 2-D modeling with grain boundary layers, a triangular FE mesh is laid out in the grain boundary layers by commercial software ABAQUS/CAE, bridging the neighboring grain core meshes consistently. The processes of voids generating are: (1) some random elements are selected to be deleted; (2) the total volume of these deleted element is calculated; (3) processes (1) and (2) are repeated until the total volume of the deleted elements is up to

the percentage of voids; (4) the remanding element numbers are re-arranged. FE generation for 3-D models is the following (Xue, 2003): First, a triangular element mesh is generated for all the grain faces globally based on the Voronoi-Delaunay duality principle (Sloan, 1993). Second, a grain-wise triangular surface mesh is laid out for each grain. Third, all of the grain-wise surface mesh is input into com mercial software HyperMesh, and the tetrahedral FE volume mesh is constructed. Finally, the volume mesh with nodes sharing consistency at grain faces is assembled. Such a mesh preserves the microstructure of polycrystalline ceramics and enables micromechanical analysis. Further, a multi-scale study on the statistical representation of polycrystal models is carried out to test the sufficient number of grains for 2-D and 3-D Voronoi polycrystal models.

The material modeling consists of nonlinear elasticity, crystal plasticity and grain boundary material model. Crystal elasticity considers general anisotropy and pressure-dependent second-order nonlinearity. The rain boundary material is treated as glassy isotropic (Longy and Cagnoux, 1989), which has the same mechanical properties as the corresponding polycrystalline material, so that the elasticity for the grain boundary material is also nonlinear due to pressure. For the modeling of crystal plasticity, a simple model of rate-independence is adopted for the calculations without the consideration of incremental path. Since the to-be-studied ceramics are in hexagonal structure, hexagonal-structured slip systems, basal and prismatic, may be considered for crystal slip. The modeling of crystal plasticity is extended to allow modeling and simulation of crystal slip and crystal deformation twinning. The grain boundary material is predicted by the

Drucker-Prager model with a pressure-saturated ceiling, and the flow-surface treatment is adopted based on the Johnson-Holmquist model (Johnson and Holmquist, 1994). The constitutive relation of the material assumes additive formulation of elastic and inelastic strains. The technique is by FE method in conjunction with user-defined code via ABAQUS user-program interface. The implementation of constitutive model is achieved by adopting a stress-based Newton-Raphson iteration (Zhang et al., 2005).

Micromechanical analysis is carried out respectively for polycrystalline α-Al_2O_3 (Lucalox), AD995 and AlON under uniaxial-strain compression. Plate impact experimental simulations on AlON are carried out based on the published experimental results. For the analysis of polycrystalline α-Al_2O_3, a solution technique by FE method with user subroutine with ABAQUS/standard is used based on a 600-grain 3-D Voronoi polycrystal model. Material modeling of nonlinear elasticity with crystal plasticity by basal slip and prismatic slip is employed. Steady-state macroscopic response of longitudinal, mean and lateral stresses versus applied longitudinal strain up to twice the HEL is predicted. Also, the influence of critical resolved shear stress (CRSS) for basal slip or prismatic slip is discussed. Microscopic analysis includes the distribution of longitudinal stress and the distribution of effective plastic strain. For the analysis of polycrystalline AD995, three types of 200-grain 2-D porous Voronoi polycrystal FE models with triangular, square and random shape voids are constructed and examined for their performance and mesh dependency for modeling and analysis of microplasticity-driven void collapsing in AD995 under shock compression. Material modeling of nonlinear elasticity with crystal plasticity by basal slip, prismatic slip and twinning

deformation is employed. The roles of ground boundary and voids in the inelastic deformation and strength of AD995 are examined and the strength of polycrystalline AD995 is analyzed. Microscopic analysis includes the distribution of longitudinal stress and the distribution of effective plastic strain. For the analysis of AlON, 2-D plate impact experimental simulations on AlON are carried out with the axi-symmetric FE model. The material strength model considers a pressure–dependent material strength model that combines the Drucker-Prager plasticity with a limited strength cap and nonlinear bulk modulus. The results of wave profiles, optimized parameters for material strength model, and the shock strength response of AlON are obtained. In addition, a 3-D analysis of 600-grain cubic VP-FE model that considers elasticity, nonlinear elasticity and crystal plasticity is carried out to determine the ambient elastic constants C_{ij} of polycrystalline AlON and other parameters for the material model.

It should be pointed out that there is available experimental measurements of material strength in shocked AD995 alumina (Dandekar & Bartowski, 1993), et al., 1998), and hence the calculated results can be compared with experimental data. For AlON, however, there are no measured longitudinal stresses to compare with. Therefore, to study the dynamic behavior in shocked AlON, material strength should be determined first of all. Material strength is determined by plate impact experimental simulations. In conjunction with the experimental simulated material strength, the base of ambient elastic constants C_{ij} of polycrystalline AlON is estimated and microplasticity analysis with a 600-grain 3-D Voronoi polycrystal model by ABAQUS/Standard is carried out.

The method for measuring the longitudinal and lateral stress is suggested by experimental simulations on polycrystalline SiC-N. The gage used is a manganin pressure sensor, a special gage with manganin foil grid for measuring hydrostatic pressure and for shock wave studies. A new finite element piezoresistance model for interpreting the measurement of a commercial manganin stress gauge embedded in a plate impact target is developed. Experimental designs and simulations are performed. The deformation and resistance change of the gage are simulated. The methods can also be used to design the stress gauge measurement for the polycrystalline AlON.

The research for strengths of polycrystalline ceramics under shock compression is significant for the technical reasons that it is the first time simulations of material response using a topological accurate polycrystal model (Voronoi tessellations) is performed, crystal slip system interactions and twinning deformation are considered; and the nonlinear elastic and plastic anisotropy of the crystals are included. The computational methodology developed in this work is capable of being extended to micromechanical analysis of other polycrystalline materials. The results of the research have a major impact on the scientific understanding of the mechanisms governing the inelastic deformation, damage and failure in ceramics due to high strain rates, and are very useful for development and design of high strength ceramics for armor applications or applications involving other extreme conditions.

1.4 Organization of the Dissertation

This dissertation has seven chapters. In Section 1.5, which is the last section of this chapter, a literature review is given. The part of the modeling methodology and the method of multi-scale analysis are presented in Chapter 2, in which construction of the 2-D and 3-D Voronoi polycrystals and the related numerical mesh generations for microstructure modeling are described first. Derivations of the material models for nonlinear crystal elasticity, crystal plasticity and grain boundary are then presented. A multi-scale study to verify proper crystal number densities for the 2-D and 3-D polycrystal models is also included in the chapter. Chapter 3 presents the analysis for the strength of polycrystalline α-Al_2O_3 (Lucalox) under shock compression. The 3-D microstructural modeling and solution technique by FE method with user-subroutine by ABAQUS/standard is presented along with the numerical simulations for the response of α-Al_2O_3 undergoing basal-slip only and both basal and prismatic slip. Chapter 4 presents the analysis for the strength of polycrystalline AD995 under shock compression. First, a crystal plasticity model of polycrystalline AD995 that is extended from that of polycrystalline α-Al_2O_3 to allow modeling and simulation of crystal slip and crystal deformation twinning is described. Second, the study of three types of porous polycrystal models is presented to examine their performance and voids collapsing. Third, examination of the roles of glass ground boundary and voids is presented. In the last part of Chapter 3, the compressive strength of polycrystalline AD995 with different critical resolved shear stress (CRSS) for slip systems is presented. In Chapter 5, the analysis for the strength of AlON under shock compression is presented. First 2-D analysis of the

strength on AlON by plate impact experimental simulations with a pressure–dependent material strength model that combines the Drucker-Prager plasticity with a limited strength cap is presented. The determination of the ambient elastic constants C_{ij} of polycrystalline AlON by using a 600-grain 3-D Voronoi polycrystal model is then presented. Preliminary microplasticity analysis is also included in this chapter. Chapter 6 presents the development of a new finite element piezoresistance model for interpreting the measurement of a commercial manganin stress gauge embedded in a plate impact target and the calibrations for the gauge in both the longitudinal and lateral configurations This enables the determination of ceramic shock strength directly from the gauge measurements in the two configurations. . Finally, the main conclusions of this research are summarized in Chapter 7.

1.5 Literature Review

Ceramic materials are increasingly being used in the industry for commercial and military applications. An overview of ceramic applications is presented by the American Ceramic Society on their web site (2005). For example, ceramic materials are used in aerospace applications for thermal protection for rocket exhaust systems; ceramic tiles are used for insulation of space shuttles and engines; and coatings are embedded into the windshield glass of airplanes. Presently, ceramic materials are being tested for use in engine components. Benefits include better performance, lighter weight engines, and better fuel consumption. Ceramic materials are also used in medical applications for replacement of human body parts (tooth, hips, knees, shoulders, elbows, fingers, to

replace diseased heart valves). When used in implants, they stimulate bone growth and tissue formation; provide protection from immune system (Omonbude and Faraj, 2004).

Advanced ceramic materials have been considered for armor applications in law enforcement, homeland security, and the military for over 30 years. But in recent years they have became an integral part of light and strong materials. Such properties of advanced ceramic materials as high strength, light weight, penetration resistance are important for civil and military applications. Ceramic materials provide significant resistance to penetration not only in solid, but also in fractured and powdered states. Therefore, it is important to study compressive strength of polycrystalline ceramics and to develop an exact microstructure model and material modeling to understand the mechanisms of inelastic under shock compression. The review includes the studies of compression strengths, microstructure polycrystal model and material modeling of polycrystalline ceramics.

1.5.1 Compression Strengths of Ceramics

Ceramics materials have proven to be good choices for many armor applications due to their high dynamic strength. Experimental techniques for measuring the compression strengths of ceramics under dynamics loading conditions have been studied for several decades. Gust and Royce (1971) used the HEL measurement to characterize the dynamic yield strengths of B_4C, beryllium oxide (BeO), and Al_2O_3. The measured HEL was 15.4 for B_4C and 8.2 GPa for BeO. For several different Al_2O_3 materials, the measured HEL ranged from 6.1 to 13.4 GPa, depending on the impurity content and material processing. Under one-dimensional strain conditions, Munson and Lawrence

(1979) measured the dynamic stress-wave response of polycrystalline α-Al_2O_3. The measured HEL is 9.1 GPa. Kipp and Grady (1989) used shock compression data and hydrodynamic estimation to investigate the shock strengths of various ceramics including SiC, AlN, titanium diboride (TiB_2), and zirconium dioxide (ZrO_2). In their studies, elastic-plastic behavior was assumed for the response of ceramics deformed under shock wave compression. Dandekar and Bartkowski (1993) measured shock response of A D995 Alumina by plane shock wave experiments. The result of HEL is 6.71 GPa. Feng et al. (1998) determined the HEL of α–6H SiC to be ~11.5 GPa under shock compression, and determined from the measured longitudinal and lateral stresses a value of ~4.5 GPa for the maximum shear stress of at the HEL. It was also found that the maximum shear stress increases with shock compression and reaches ~7 GPa at twice the HEL. More recently, Thornhill et al. (2005) measured the wave profiles of interface particle velocity by plate impact experiment on AlON, but the compression strength of polycrystalline AlON is still not clear.

Studies on the underlying micromechanisms of inelastic deformations of shocked ceramics are important for good understanding of compression strengths of ceramics, but the studies are limited and mostly speculative. Grady (1996, 1998) proposed that the cause for high HEL and high post-HEL strength in shocked ceramics is a strain-rate dependent brittle-to-ductile transition. Another theory suggested by Feng et al. (1998) emphasizes the high inertial confinement accompanying plane shock wave loading. Under high confining stresses, in-grain slipping in certain crystallographic systems may

become more favorable than shear cracking because the high confinement significantly increases the frictional resistance against the later process.

1.5.2 Polycrystal Modeling of Ceramics

To effectively carry out micromechanical analysis of polycrystalline materials, a good polycrystal microstructure modeling is essential to characterize the heterogeneity due to grain-to-grain topological variations and crystal anisotropy. Furthermore, the microstructure model should contain sufficient microstructual elements to represent statistically the macroscopic response of the material in bulk.

A polycrystalline material may be globally isotropic and homogeneous but is typically anisotropic and heterogeneous. An important need is the proper modeling of the microscale anisotropy and heterogeneity, i.e., the spatial variation of the physical properties and geometrical characteristics. For instance, the physical property may be orientation-dependent and hence anisotropic with respect to loading. In particular, there exist elastic anisotropy (the elastic properties of a crystal are direction-dependent) and plastic anisotropy (slip system activation and the slip magnitude are direction-dependent). Thus, heterogeneity results from different crystallographic orientations at different locations. Similarly, heterogeneity also results from the variation of crystal geometry (shape and size) with position. The coupling of mechanical anisotropy and topological variation can exert a significant and complex influence on the microstructural stresses and also on microscale processes such as microcrack nucleation. Wu and Niu (1995) showed that crack nucleation in a two-dimensional (2-D) Voronoi model of polycrystalline ice was significantly affected by the elastic anisotropy and the

randomness in the geometrical microstructure. Teng and Lin (1995) showed that crystal elastic anisotropy has a significant effect on fatigue crack initiation in an intermetallic nickel-aluminum polycrystal comprised of regular hexagons. We conjecture that heterogeneity will also influence the deformation of ceramics under shock compression.

For decades, people have modeled various microstructures, idealized or realistic, to investigate the micromechanics in polycrystals. A simple idealized microstructure is an aggregate of square or cubic grains. Baczmanski et al. (1994) used several thousand square grains for the prediction of residual stresses and texture development in plastically deformed steel. Hexagonal grains have also been used as idealized polycrystals, e.g., Evans (1978) examined the residual stresses at triple junctions due to thermal expansion anisotropy in a polycrystalline aggregate of planar hexagonal grains. Furthermore, Ortiz and Suresh (1993) showed that an accurate estimate of residual stresses required at least two hundred regular hexagonal grains, and the stress distributions were essentially Gaussian, when a set of random distortions was assigned to the grains.

Idealized polycrystals, however, cannot characterize the shape and size variations of polycrystalline materials, and therefore realistic microstructures are needed for accurate micromechanical analysis. A Voronoi tessellation, which is a topologically accurate model of the microstructure of polycrystalline metals and ceramics (Kumar and Kurtz, 1994; Kumar et al., 1996), has been extensively used in the last two decades. Wu and Niu (1995) verified the Gaussian nature of the stress distributions due to elastic anisotropy in polycrystalline ice modeled by 2-D Voronoi tessellations. Using a similar model, Wu and He (1999) predicted the cracks resulted from the pile-ups of extrinsic

grain boundary dislocations around triple junctions in polycrystalline aluminum. Ghosh et al. (1997) developed a Voronoi cell finite element model for micromechanical analysis of ceramic-metal composites. Wu and Guo (2000) advanced a three-dimensional (3-D) Voronoi model to study the influence of elastic anisotropy of cubic and hexagonal metallic crystals on the stress intensity factors of intergranular cracks.

1.5.3 Material Modeling of Ceramics

Modeling of crystal plasticity for ductile materials has been well documented (e.g., Asaro, 1983; Nemat-Nasser and Okinaka, 1996; Anand and Kothari, 1996). Asaro (1983) considered strain-hardening of rate-dependent polycrystals in the development of large strain-continuum constitutive laws. Nemat-Nasser and Okinaka (1996) proposed an algorithm for analyzing the deformation of fcc single crystal, also assuming rate-dependent slip. Anand and Kothari (1996), on the other hand, presented a computational procedure for determining the increments of shear on a unique set of active slip systems in a rate-independent theory. Moreover, Gupta (1977) examined the crystal anisotropy effect on intracrystalline plasticity in shocked lithium fluoride (LiF) single crystals. Microplastic strains in brittle polycrystalline solids prior to microfracture were studied by Sarfarazi (1989), based on the continuous activation of Frank-Read sources in the grains. Little work, however, has been done on the modeling of microplasticity in inherently strong solids.

The Johnson-Cook plasticity model is known to be suitable for high strain rate deformation of most metals (e.g., Daridon et al., 2004; Buchar et al., 2004). It is actually a particular type of Mises plasticity model with analytical forms of the hardening law and

rate dependence, and is typically used in adiabatic transient dynamic simulations (ABAQUS manual, 2004). The Drucker-Prager model is more suitable for granular-like brittle materials, such as soils and ceramics. This type of material becomes stronger when pressure increases, and the compressive strength is greater than the tensile strength. The model can capture the frictional sliding behavior and allow inelastic shearing (ABAQUS manual, 2004). For instance, Kolari et al. (2002) described the yield stress state and material softening of solid ice after yielding with the Drucker-Prager model. Though the Drucker-Prager model in conjunction with shear failure model may predict well the inelastic behavior of ceramics during shock compression, the failure during unloading or recovery may be beyond its capability. Johnson and Holmquist (1994) advanced the modeling of glassy brittle materials by describing the strength in two smoothly varying functions for intact and fractured materials respectively. The fractured materials sustain much lower strength than intact materials.

There is ample evidence that ceramics do slip under high confinement and/or high temperature. Bretheau et al. (1979) documented the plastic deformation of α-Al_2O_3 single crystals (which are typically treated as hexagonal-structured material) by slip in the basal, prismatic and pyramidal systems at high temperatures $T > 1025$°C. Heuer et al. (1971) observed non-basal slip in polycrystalline Al_2O_3 deformed at 1000°C and 1400°C under confinement. Castaing et al. (1981) deduced from optical observations prismatic slip in Al_2O_3 single crystals subjected to hydrostatic pressures of 0.5-1.5 GPa between 20°C and 950°C. Generally speaking, the basal systems $\{0001\}<11\bar{2}0>$ are the predominant slip systems for most hexagonal crystals. Non-basal glide requires a higher critical resolved

shear stress (CRSS). To our best knowledge, however, most of the observations were made when thermally activated dislocation motion plays a significant role, and it is not clear whether the reviewed results could be extended to the conditions for shock compression, where shock-induced temperature is typically below 1025°C. Also, determining critical resolved shear stress for a certain slip system is difficult.

1.5.4 Description of Some Polycrystalline Ceramics

Polycrystalline ceramics of two polycrystalline α-phase aluminum oxides (α-Al_2O_3), Lucalox (99.9% pure and dense) and AD995 (99.5% pure and 97% dense), polycrystalline aluminum oxynitride (AlON), and ploycrystalline silicon carbide (SiC). are considered in this research. The unique combination of strong and transparent has made these materials excellent candidates for armors. Both physical properties and crystal structures of these materials are simply described. The most commonly used α-Al_2O_3 is the polycrystalline α–phase Alumina (Lucalox) with a high purity of 99.9%. α-Al_2O_3 is typically treated as hexagonal-structured material. The ambient density of α-Al_2O_3 is 3.986 g/cm^3, and its HEL measured by Munson and Lawrence (1979) is ~ 9 GPa. Polycrystalline α-Al_2O_3 has many uses in high-pressure science. It is used in diamond anvil cells as manometer; as a window material in shock physics; and in armor applications. Polycrystalline AD995 is another type of polycrystalline α–phase Alumina alumina and is formed by Al_2O_3 powder (99.5%) with a small amount of aluminosilicate glass (0.5%) as a stabilizing agent. The crystal structure of the AD995 is identical to that of α-Al_2O_3. The ambient density is 3.89 g/cm^3 due to a small amount of porosity in the

ceramics and the addition of lower density glass. The HEL is 7.0 – 7.9 GPa, significantly less than α-Al_2O_3. Polycrystalline AD995 has uses in armor application. AlON is a polycrystalline ceramic material formed from a solid solution of Al_2O_3 and AlN (McMcauley, 2002). In this form, the crystal structure is a nitrogen-stabilized cubic spinel with an ambient density of 3.67 g/cm^3. The HEL is reported to be 10 – 12 GPa. Because of its high strength and manufacturability of this material into many custom shapes, it is used in armor application as a window material.

CHAPTER 2

MODELING METHODOLOGY

2.1 Introduction

Voronoi tessellation was first introduced by Dirichlet and Voronoi (Okabe et al., 1992), who presented the tessellation in 2-D and 3-D space. Polycrystal model based on the Voronoi tessellation has been suggested as a topologically accurate model to the microstructure of polycrystalline ceramics and metals (Kumar and Kurtz, 1994; Kumar et al., 1996). The Voronoi polycrystal has the characteristics of all nuclei of grains appear simultaneously at random positions and each grain grows at the same rate in all directions. In the previous studies of our group (Xue, 2003; Zhang, 2005), using the method of Voronoi tessellation, a computational modeling methodology for micromechanical analysis of polycrystalline ceramics has been developed. It consists of a microstructural model based on the 2-D or 3-D Voronoi tessellation, and material models for compression-dependent nonlinear elasticity and crystal plasticity as well as for intergranular shear damage under compression. In this chapter, the modeling methodology is reviewed, and at the same time, the development of 2-D 200-grain square polycrystal model with grain boundary layers and 3-D 600-grain cubic polycrystal model

are described, and then the new model tests of multiscale modeling technique are presented in detail.

Voronoi polycrystal model constructions and numerical mesh generation for polycrystal analysis are described in Section 2.2. For 2-D modeling, the grain-wise geometry of a 2-D Voronoi polycrystal can be imported into the commercial FE software ABAQUS/CAE (ABAQUS manual, 2007), which can generate triangular elements sharing nodal consistency at the grain boundaries. For 3-D modeling, the grain-wise meshing technique by Xue (2003) is adopted. In this meshing technique, the Voronoi-Delaunay duality principle is used to construct a triangular-element grain surface mesh. The grain surface mesh is then imported into the commercial mesh code HyperMesh (HyperMesh manual, 2007) to generate a tetrahedron-element volume mesh that shares the nodes on grain surfaces with the grain surface mesh.

The material modeling for computational investigation of the micromechanisms governing the inelastic deformation of polycrystalline ceramics under high confining stresses and/or high strain rates is presented in Section 2.3. Under highly confined uniaxial-strain compression, the elastic response of a ceramic may be noticeably nonlinear even at its elastic limit. It suggests that the elastic nonlinearity of polycrystalline ceramics depends predominantly on volume compression or pressure (Bassett et al., 1993; Feng et al., 1998; Yuan et al., 2001). A simple nonlinear elasticity model is used to describe the volume-compression dependent stiffening. The nonlinear elasticity model is described in section 2.3.1.

A crystal plasticity model for the hexagonal symmetry is considered for analyzing microplasticity in ceramics during shock compression. There are three types of possible slip systems for hexagonal crystals: basal, prismatic and pyramidal (Bretheau et al., 1979; Heuer et al., 1971). The basal slip is predominant because it has the lowest activation threshold. The crystallographic orientations of the three types of slip are depicted in Figure 2.1 (Zhang, 2005). The crystal plasticity modeling is presented in Section 2.3.2.

It is assumed that microdamage only occurs at grain boundaries in the forms of intergranular shear damage under compression. Grain boundaries are treated as glassy second phase. The ground boundary material may be modeled as an isotropic solid. The flow stress is assumed to be governed by a pressure-dependent "plasticity" law using the Johnson-Holmquist (JH-2) model (Johnson and Holmquist, 1994). The JH-2 model is described in Section 2.3.3.

2-D and 3-D Voronoi polycrystal models are verified by the simulations of a plate impact experiment using multiscale modeling technique, in which a Voronoi polycrystal is embedded in a homogeneous matrix. The details of the model structures, material parameters and boundaries conditions used in the simulations are presented in Section 2.4 along with the numerical results.

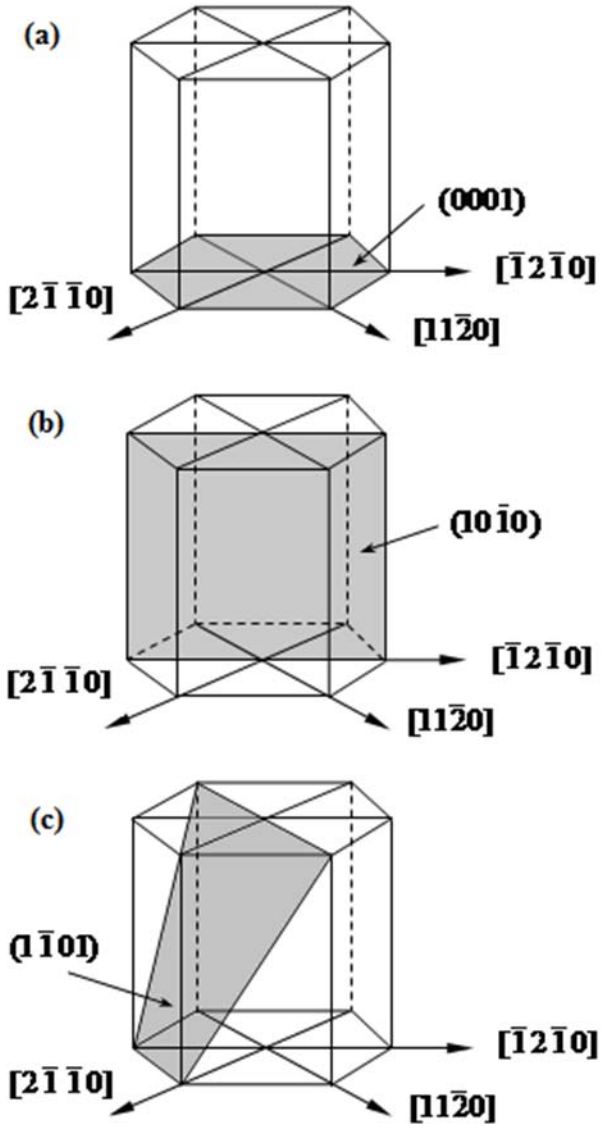

Figure 2.1: Slip systems for (a) basal, (b) prismatic and (c) pyramidal Slips

2.2 Polycrystal Modeling

Closed-space Voronoi tessellation (e.g., Kumar et al., 1992; Xue, 2003) is one of algorithms for structural constructions of the 2-D and 3-D Voronoi polycrystals. Because it is convenient for micromechanical analysis, the principles of closed-space Voronoi tessellation is adopted. In particular, the algorithms developed by Xue (2003) for constructing square (2-D) and cubic (3-D) Voronoi polycrystal models are employed.

Details of the algorithm for constructing a 3-D Voronoi polycrystal in a unit cube are reviewed in Appendix A-1. The algorithm for constructing square (2-D) Voronoi polycrystal model is similar to that for the 3-D model. The difference is that all planes degenerate to lines and that each vertex is obtained from line intersection. When the FE method is used for numerical solution, the model is termed as the Voronoi polycrystal-finite element (VP-FE) model. For creating grain boundaries in a 2-D Voronoi polycrystal, each Voronoi cell is contracted by moving each of its edges the same small distance towards its centroid.

According the algorithms for constructing 3-D Voronoi polycrystal and 2-D Voronoi polycrystal, a 2-D 200-grain square polycrystal model and a 3-D 600-grain cubic polycrystal model are developed, shown in Figure 2.2 and Figure 2.3, respectively. For a 2-D polycrystal model, grain boundaries with uniform thickness are constructed by contracting crystal cells, shown in Figure 2.2 (zoom in view). The Thickness is considered as 1% of the side length of the square.

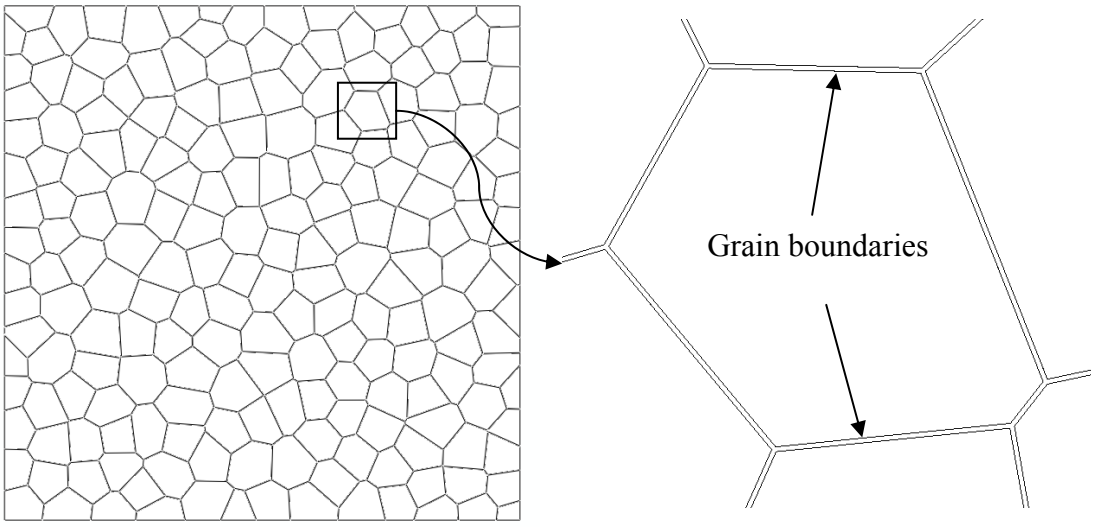

Figure 2.2: 200-grain square polycrystal model with grain boundaries.

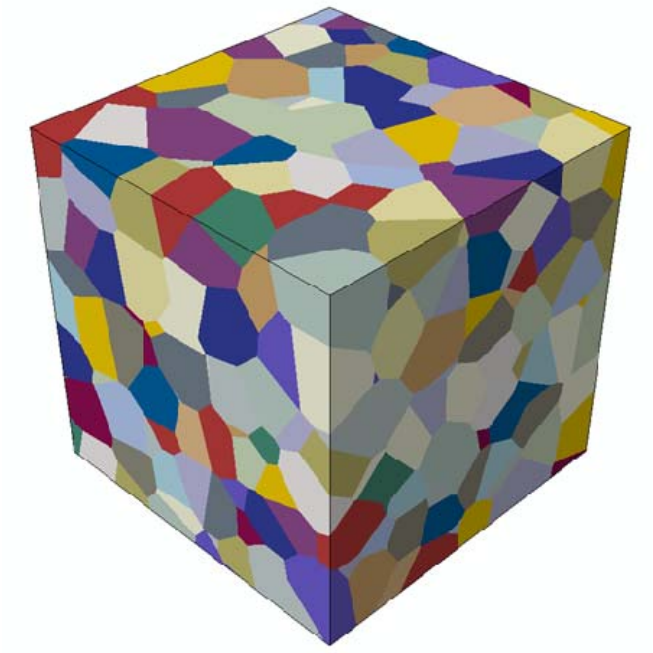

Figure 2.3: 3-D 600-grain cubic polycrystal model.

For a 2-D polycrystal model, microstructure-preserving triangular numerical mesh can be generated by the commercial FE software ABAQUS/CAE as described earlier (Section 2.1). The 2-D polycrystal model is implemented into ABAQUS/CAE and gets meshes. Figure 2.4 shows an example of mesh for a 2-D 200-grain square model. In the

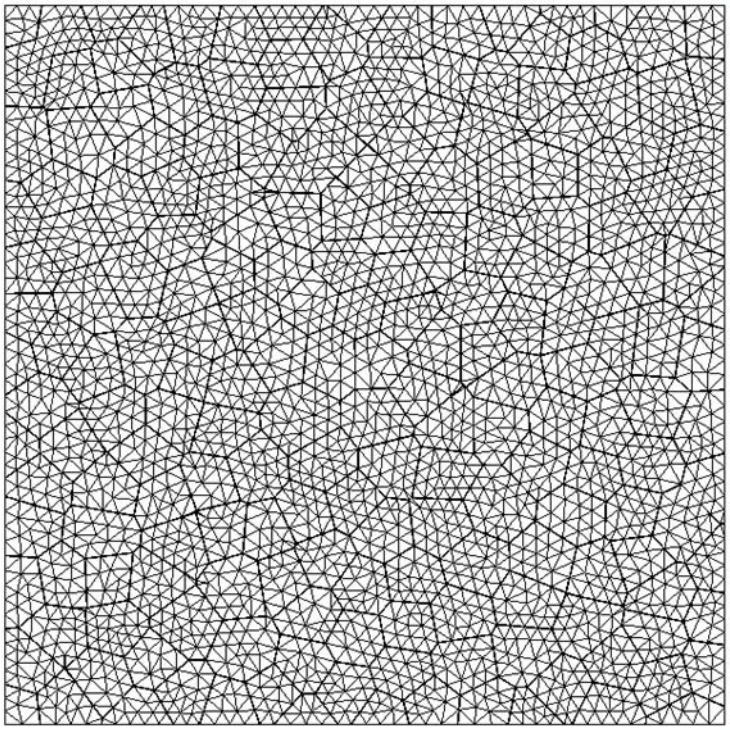

Figure 2.4: A 200-grain square Voronoi polycrystal model with a microstructure-preserving triangular numerical mesh.

same way, microstructure-preserving numerical mesh for grain boundary layers can also be generated by ABAQUS/CAE. Figure 2.5 shows the zoom-in views of square VP-FE models with two different methods of meshing, one layer (a) and three layers (b) of grain boundary elements, respectively. It is found that the two method of meshing for layers of

grain boundary elements are not important to affect the analysis (Zhang, 2005). So only one layer elements of grain boundary is considered in this study.

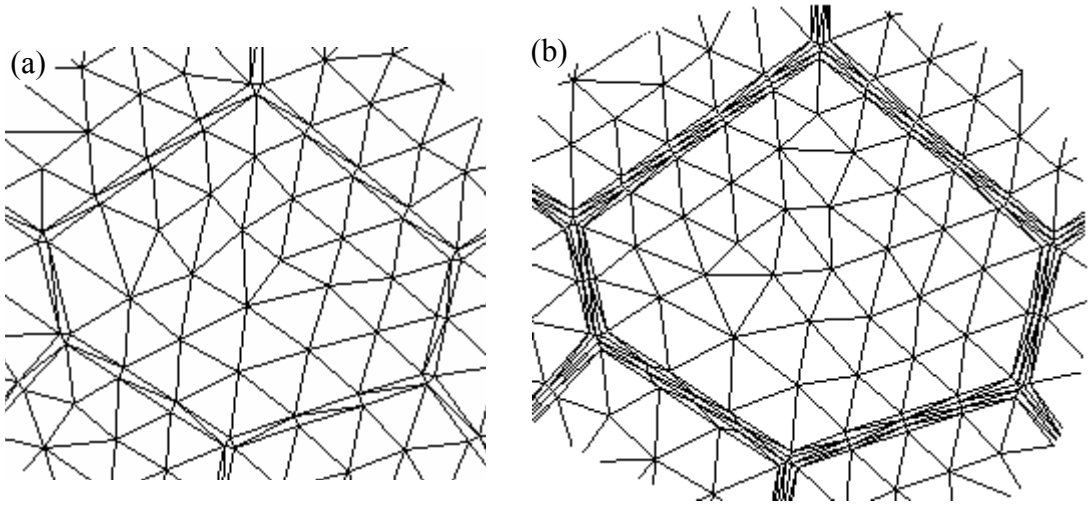

Figure 2.5: Zoom-in views of square VP-FE models with grain boundary layers: (a) one layer, and (b) three layers of grain boundary elements.

For a 3-D polycrystal model, currently, there is no commercial code capable of generating microstructure-preserving numerical mesh. The grain-wise meshing technique has been developed by Xue (2003). The procedure is as follows:

1. Input the geometric data of the 3-D Voronoi polycrystal model to be meshed in terms of grain-wise sequenced faces, vertices and edges.
2. Select a characteristic length *s* as the nominal element edge length.
3. Deposit nodes on all of the grain vertices and then on all of the grain edges with a spacing as close to *s* as possible. The deposition is executed globally so that there

is only one node arrangement on each grain edge (which is shared by *three* neighboring grains).

4. For each grain face, add an imaginary polygon, which is a concentric contraction from the polygon occupied by the edges of grain face. The amount of contraction is determined by making the largest distance between the edges of inner and outer polygons equal to *s*. If the inner polygon is large enough to contain a further contracted imaginary polygon, it will be added following the same principle and so forth until there is no room for a new round of contraction.

5. Deposit nodes on all inner polygon vertices and on all inner polygon edges with a spacing as close to *s* as possible. The deposition is also executed globally so that there is only one node arrangement on each grain face (which is shared by *two* neighboring grains).

6. For each grain face, apply the Delaunay triangulation to obtain a unique triangle-element face mesh including the nodes on the grain edges.

7. Assemble the entire surface mesh for each grain. In this process, each grain face mesh is used twice as there are two grains sharing the grain face. The connectivity table for the grain surface mesh is determined to enforce that the sequence of three nodes of each triangular element is counterclockwise with respect to the outward normal of the grain face, on which the element is located.

8. For each triangle-element grain surface mesh, use the HyperMesh code (HyperMesh manual, 2006) to construct a tetrahedron-element volume mesh

whose nodes on the grain faces are forced to coincide with the nodes of the grain surface mesh. The available uniform element size option is selected and grain-to-grain automatic batch processing is used in this process.

9. Assemble the grain-wise volume elements, remove the redundancies on the grain faces, edges and vertices, and construct the global connectivity table that enforces the counterclockwise sequence to the four nodes of every tetrahedral element. The result is a tetrahedron-element numerical mesh that preserves the microstructure of 3-D Voronoi polycrystal model.

A structural model constructed in such a way will be referred to as a 3-D VP-FE model for the rest of the dissertation. Figure 2.6 shows an example of mesh for a 600-grain cubic VP-FE model.

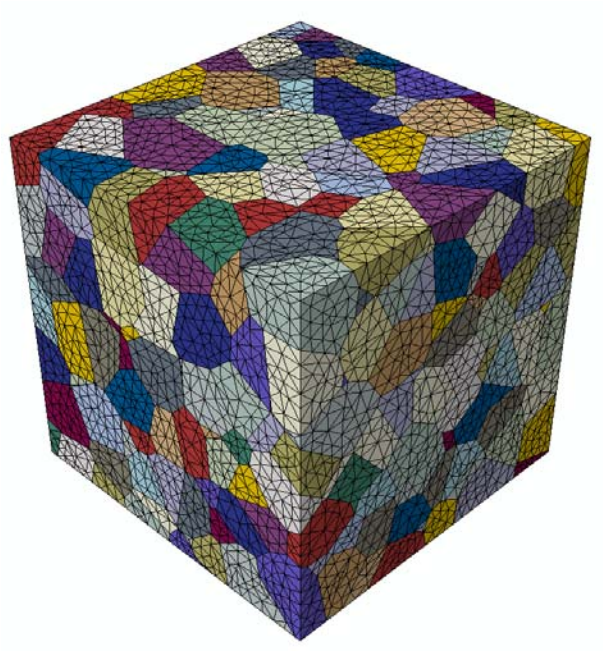

Figure 2.6: A 3-D 600-grain cubic polycrystal model with mesh.

2.3 Material Modeling

2.3.1 Nonlinear Crystal Elasticity Model

Assuming the additive formulation of elastic and plastic strain rates, the rate constitutive equation with respect to the current local crystallographic axes may be described as

$$\dot{\boldsymbol{\sigma}} = \mathbf{C} : (\dot{\boldsymbol{\varepsilon}} - \dot{\boldsymbol{\varepsilon}}^{p}) + \mathbf{W} : \dot{\boldsymbol{\omega}}, \quad i, j, k, l = 1, 2, 3 \tag{2.3}$$

where the superimposed dot denotes the material time derivative, $\boldsymbol{\sigma}$ is the symmetric Cauchy stress tensor, $\mathbf{C}$ is the fourth order tangent elasticity tensor of the deformed material with respect to the current crystallographic base, $\mathbf{W}$ is the fourth order tensor that specifies the stress rate transformation under time-dependent rigid rotations, $\dot{\boldsymbol{\varepsilon}}$ and $\dot{\boldsymbol{\omega}}$ are respectively the symmetric and asymmetric parts of the velocity gradient, and $\dot{\boldsymbol{\varepsilon}}^{p}$ is the plastic strain rate.

The elastic response of a ceramic compressed uniaxially to its Hugoniot elastic limit (HEL) may be noticeably nonlinear. Typically, the information available for the nonlinear elastic response of ceramics is the pressure vs. volume compression of their polycrystalline powders or bulk materials (e.g., Bassett et al., 1993; Feng et al., 1998). It has been observed that the effect of volume compression is relatively strong on the elastic dilatation while weak on the elastic distortion. Accordingly, we may consider volume-compression dependent corrections only for the dilatational components of the *tangent* elastic constants, i.e.,

$$C_{iijj} = C^0_{iijj}\left[1 + A(V_0 - V)/V_0\right], \tag{2.4a}$$

$$C_{ijij} = C^0_{ijij},\ i \neq j \tag{2.4b}$$

and

$$C_{iiij} = 0,\ i \neq j \tag{2.4c}$$

where i, j = 1, 2, 3 (no sum on i or j), the superscript "0" denotes the properties in the undeformed initial state, A is the correction parameter, and V_0 and V are respectively the initial and current specific volumes. Note that Eq. (2.4c) states no coupling between the dilatation and distortion modes, which is the case for crystals with the hexagonal structure. Unless otherwise specified, this simple nonlinear elasticity model is used to describe the volume-compression dependent stiffening.

2.3.2 Crystal Plasticity Model

The constitutive model for crystal plasticity uses a rate formulation and takes into consideration dislocation motions on multiple slip systems. The rate of plastic strain with respect to crystal axis is calculated by

$$\dot{\boldsymbol{\varepsilon}}^p = \sum_{\alpha=1}^{n} \mathbf{P}^{(\alpha)} \dot{\gamma}^{(\alpha)}, \tag{2.5}$$

With

$$\mathbf{P}^{(\alpha)} = \frac{1}{2}(\mathbf{m}^{(\alpha)} \otimes \mathbf{n}^{(\alpha)} + \mathbf{n}^{(\alpha)} \otimes \mathbf{m}^{(\alpha)}), \tag{2.6}$$

where $\mathbf{P}^{(\alpha)}$ is the Schmid direction tensor, $\mathbf{m}^{(\alpha)}$ and $\mathbf{n}^{(\alpha)}$ are respectively the unit vector of slipping direction and that normal to the slip plane of the α-slip system, and $\dot{\gamma}^{(\alpha)}$ is the

rate of plastic shear strain of the system, which is determined by the following simple power law (Zhang et al., 2005):

$$\dot{\gamma}^{(\alpha)} = \dot{\gamma}_0 \operatorname{sgn}(\tau^{(\alpha)}) \left| \tau^{(\alpha)} / g^{(\alpha)} \right|^k \text{ for } \tau^{(\alpha)} > g^{(\alpha)}. \tag{2.7}$$

Here $\dot{\gamma}_0$ is the reference shear rate, k is the rate sensitivity parameter, $\tau^{(\alpha)}$ is the shear stress resolved on the α-slip system, i.e.,

$$\tau^{(\alpha)} = \mathbf{P}^{(\alpha)} : \boldsymbol{\sigma}, \tag{2.8}$$

and $g^{(\alpha)}$, which measures the system strain hardening, uses the initial critical resolved shear stress (CRSS) τ_c as the starting value and evolves as:

$$\dot{g}^{(\alpha)} = \sum_{\beta=1}^{n} h_{\alpha\beta} \left| \dot{\gamma}^{(\beta)} \right|, \tag{2.9}$$

where $h_{\alpha\beta}$ are the slip-plane hardening moduli. For hexagonal-structured crystals, basal, prismatic and pyramidal slips are the three types of plausible slip systems. Assume no coupling between different types of slip systems, the components of $h_{\alpha\beta}$ are (Hutchinson, 1976):

$$h_{\alpha\beta} = h_0 \sec^2\left(\frac{h_0 \gamma}{\tau_s - \tau_c} \right) \left[q + (1-q)\delta_{\alpha\beta} \right], \tag{2.10a}$$

if α and β are the same type of slip systems. Otherwise,

$$h_{\alpha\beta} = 0. \tag{2.10b}$$

In Eq. (2.10a), h_0 is the initial hardening rate, τ_s is the maximum value of critical resolved shear stress, q is a constant in the range of [1, 1.4], $\delta_{\alpha\beta}$ is the Kronecker delta, and γ is a measure of the cumulative plastic shear strain calculated by summing the contributions from all n slip systems, i.e.,

$$\gamma = \int \sum_{\beta=1}^{n} \left| d\gamma^{(\beta)} \right| . \tag{2.11}$$

It should be pointed out that the values for τ_s and τ_c are different for different types of slip systems.

A stress-based Newton-Raphson algorithm has been developed to solve the above nonlinear constitutive equations iteratively (Zhang, et al., 2005). The solution procedure and iteration scheme are described in Appendix A-2 by Equations 2.12 ~ 2.31. The iterative solution scheme is implemented in ABAQUS/Explicit through User-defined subroutine - VUMAT

2.3.3 Grain Boundary Material Model

Some polycrystalline ceramics have glassy grain boundaries, e.g., 10% of intergranular glassy phase was observed in the α-Al_2O_3 studied by Longy and Cagnoux (1989). It is therefore reasonable to treat these grain boundaries as secondary material phase. As a reasonable approximation, the grain boundary material may be modeled as an isotropic solid having the same elastic response as that of the corresponding polycrystalline ceramic. The constitutive relation of the material can be described by the following rate equation:

$$\dot{\boldsymbol{\sigma}} = \overline{\mathbf{C}} : (\dot{\boldsymbol{\varepsilon}} - \dot{\boldsymbol{\varepsilon}}^{p}) + \mathbf{W} : \dot{\boldsymbol{\omega}}\,, \tag{2.32}$$

where $\overline{\mathbf{C}}$ is the tangent elasticity tensor of the material. Its two independent components, the Lamé constant λ and shear modulus μ, may have volume-compression dependence similar to that considered in the nonlinear crystal elasticity model (Section 2.3.1), i.e.,

$$\lambda = \lambda^{0}[1 + B(V_0 - V)/V_0]\,, \tag{2.33a}$$

$$\mu = \mu^{0}\,, \tag{2.33b}$$

where B is the nonlinearity correction parameter. The values of λ^0 and μ^0 (where superscript "0" denotes the properties of initial undeformed material) are taken to be those of the corresponding polycrystalline material under the ambient conditions and B is determined by matching the bulk modulus-volume compression relation of the corresponding polycrystalline material (either experimental measurements, e.g., Yuan et al., 2001 or results of polycrystal simulations). This approach ensures the consistency with the nonlinear crystal elasticity described earlier (Section 2.3.1).

The rate of "plastic strain" in Eq. (2.32) is physically the rate of inelastic strain in the grain boundary material due to intergranular shear damage. The flow stress is assumed to be governed by a pressure-dependent "plasticity" law, which adopts a flow-surface treatment of the Johnson-Holmquist (JH-2) model (Johnson and Holmquist, 1994) as depicted in Figure 2.7. The curve (F_s and F_c) is the flow surface for the initially intact material under monotonic loading, which has a pressure-dependent strength portion that follows the Drucker-Prager plasticity theory (Loret and Prevost, 1986) (F_s) and a limiting strength portion that is pressure-independent (F_c). This treatment is motivated by the

experimental observation that the macroscopic material strength of shocked ceramics increases with compression and saturates when shock stress approaches 2×HEL (e.g., Feng et al., 1998).

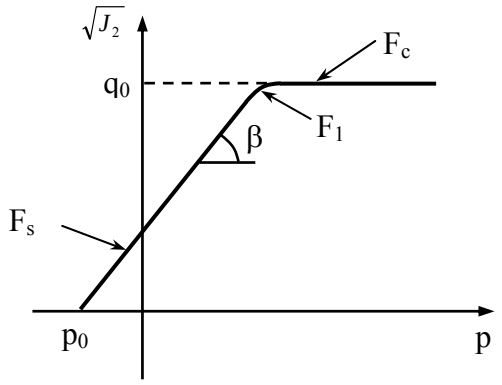

Figure 2.7: Schematic of flow-surface treatment for grain boundary material.

The flow surfaces in Figure 2.7 may be mathematically described by the following functions:

$$F_s = \sqrt{J_2} - (p - p_0)\tan\beta = 0\,, \tag{2.34a}$$

$$F_c = \sqrt{J_2} - q_0 = 0\,, \tag{2.34b}$$

where $p = -\sigma_{ii}/3$ is the equivalent pressure stress with summation on i, σ_{ij} are the components of the Cauchy stress, $J_2 = S_{ij}S_{ij}/2$ is the second invariant of the deviatoric stress tensor with summations on both i and j and $S_{ij} = \sigma_{ij} + p\delta_{ij}$, q_0 is the strength limit, β is the friction angle of F_s, and p_0 represents the cohesion of intact material. Note that

for the smoothness of flow surfaces, the transition between F_s and F_c follows the circular curve:

$$F_1 = \sqrt{\left(\sqrt{J_2} - (1-\alpha_1)q_0\right)^2 + \left(p - p_1\right)^2} - \alpha_1 q_0 = 0 \tag{2.35a}$$

with $$p_1 = q_0\left(\alpha_1 \tan(\beta/2) + \cot\beta\right) + p_0\,, \tag{2.35b}$$

where, $\alpha_1 q_0$ is the radii of two transition curves.

The constitutive equation of the Drucker-Prager model can be solved with arbitrary degree of non-associativity (Loret and Prevost, 1986). The outward normal of F_s can be computed from Eq. (2.34a) as

$$Q_{ij}^s = \frac{\partial F_s}{\partial \sigma_{ij}} = \frac{1}{3}\tan\beta\,\delta_{ij} + \frac{1}{\sqrt{2S_{kl}S_{kl}}}S_{ij}\,, \tag{2.36}$$

The components of the rate of plastic strain may be determined according to the following flow rule:

$$\dot{\varepsilon}_{ij}^p = \eta P_{ij}^s\,, \tag{2.37a}$$

with $$P_{ij}^s = \frac{1}{3}\tan\theta\delta_{ij} + \frac{1}{\sqrt{2S_{kl}S_{kl}}}S_{ij}\,, \tag{2.37b}$$

where η is a positive scalar; $\theta \geq 0$ is the dilatation angle. If $\theta \neq \beta$, the flow rule is non-associative. When $\theta = \beta$, $P_{ij}^s = Q_{ij}^s$ and the flow rule becomes associative.

It is reasonable to assume that β and p_0 in Eq. (2.34a) are constants, implying that no deformation-induced strengthening is expected. Therefore, time differentiation of Eq. (2.34a) yields the following consistency condition:

$$\dot{F}_s = Q_{ij}^s \dot{\sigma}_{ij} = 0 . \tag{2.38}$$

Combining Eqs. (2.32), (2.37a) and (2.38) gives η as

$$\eta = \frac{Q_{ij}^s \overline{C}_{ijkl} \dot{\varepsilon}_{kl}}{Q_{ij}^s \overline{C}_{ijkl} P_{kl}^s} . \tag{2.39}$$

The algorithms for solving the constitutive equations on the other portions of the flow surfaces follow the same procedure.

The extent of in-grain plastic strain and that of inelastic grain boundary strain are measured using the effective plastic strain at the integration point of each numerical element, which is defined as

$$\bar{\varepsilon}^p \equiv \int_0^t \sqrt{\frac{2}{3} \dot{\varepsilon}_{ij}^p \dot{\varepsilon}_{ij}^p} \, dt . \tag{2.40}$$

User-defined subroutine (VUMAT) which consists of three subroutines: one (VUMAT_MAT1) for crystal plasticity, one (VUMAT_MAT2) for bi-crystal boundaries, and the other (VUMAT_MAT3) for triple-crystal junctions, is implemented in ABAQUS/Explicit.

2.4 Modeling Tests

In the previous work by Zhang (2005), an analysis based on a 100 - grain square Voronoi polycrystal model at mesoscale with grain boundary of macroscopically homogeneous material was developed and applied to study the microplasticity in uniaxially compressed polycrystalline aluminum oxide and the resulting effective material strength (Zhang, 2005). However, the statistic analysis of longitudinal stress response is not good since there are stress concentrations of crystals around the square. The number of crystals in the inner of square is not enough for the analysis. Hence 200-grains of 2-D model and 600 grains of 3-D model are considered for the analysis. So the results of the model parameters obtained in the previous study need be verified if they are suitable to the new polycrystal model for the dynamic finite element analysis. Although polycrystal modeling, which accounts for crystal anisotropies and grain-to-grain topological variations and permits implementation of crystal plasticity models of interest, may be used to analyze mesoscopically heterogeneous inelastic deformation via transgranular slip or twinning in some grains under shock compression, the size affordable is too small to run wave propagation simulations needed to extract material properties from plate impact experiment. To address this issue, a multiscale modeling technique is developed, in which a Voronoi polycrystal is embedded in a homogeneous matrix of the size proper for simulating the experiment. Using the multiscale modeling, it not only can solve the problem that some crystals have so rigid when the loading of pressure or displacement is applied directly on the polycrystal model, but the most important is that the loading of multiscale model, simulated from the experiment, is

realistic. The multiscale modeling technique is applied to analyze the inelastic deformation and effective strength of polycrystalline Al_2O_3 under shock compression using the plate impact data from the work of Munson and Lawrence (Munson and Lawrence, 1979). The details are described as follows.

2.4.1 Multiscale Modeling and Analysis

Multiscale modeling. Figure 2.8 shows a schematic illustration of the multiscale modeling technique as used for the analysis. The technique is a two-step approach. In the first step, a wave propagation simulation approach, which is similar to those commonly used for dynamic finite element analysis of plate impact experiment, is used to verify or optimize the parameters of macroscopic homogeneous material model by matching the computed wave profile of velocity between buffer and window with the experimental measurement data. The configuration for plate impact experimental simulation is shown in Figure 2.8 (a). Thicknesses of aluminum impactor and target disks are 5.04 mm and 6.35 mm respectively. A fused-silica buffer is 3.25 mm thick and a fused-silica window is 25.4 mm thick.

In the second step, mesoscopic analysis of Vonoroi polycrystal approach is used to verify or optimize the parameters of polycrystal material model. The configuration of a heterogeneous sub-domain for mesoscopic analysis is shown in Figure 2.8 (c). The center is a 200 grain Vonoroi polycrystal and the rest is treated as a homogeneous material. The heterogeneous sub-domain has the same size and boundary nodal as a homogeneous sub-domain (containing only the homogeneous material), shown in Figure 2.8 (b), which is taken 9 unit elements from the center of the target. The sample is in the center of the

homogeneous sub-domain where the simulation results of stress-strain curves are plotted. To verify or optimize the parameters of polycrystal material model, the triaxial stress-strain curves volume-averaged over the center portion of the Vonoroi polycrystal approach is close to those computed at the sample of plate impact simulation.

The details of analysis for multiscale modeling are described as follows. First, the finite element model of plate impact simulation is implemented into ABQUS/Explicit. Figure 2.8 (b) shows an example of the representative mesh. The target, buffer and window are assembled by ABAQUS/Tie. The impactor and the target are contacted by using ABAQUS/ Surface- to-Surface contact (Explicit). The impactor has an initial velocity V_0 = 760 m/s.

The material model for non-linear elastic fused-silica is described by the following constitutive equations (Feng and Gupta,1996).

The mean stress response

$$P_H = 367.7\mu - 3907\mu^2 + 3751\mu^3 - 130100\mu^4 (kbar), \tag{2.41}$$

where μ $(= V_0/V - 1)$ is the volume compression. V_0 and V are the current and initial specific volumes, respectively.

The shear modulus, expressed using two linear functions of μ

$$G = 306.2 - 1199\mu (kbar) \qquad for \qquad \mu \le 0.076, \tag{2.42 a}$$

and $$G = 215.076 + 668.4(\mu - 0.076)(kbar) \qquad for \qquad 0.076 < \mu \le 0.12. \tag{2.42 b}$$

The macroscopic material model for alumina uses the mean stress response predicted by elastic polycrystal simulation and material strength model that combined the Drucker-Prager plasticity with a prescribed limited strength, described in section 2.3.3,

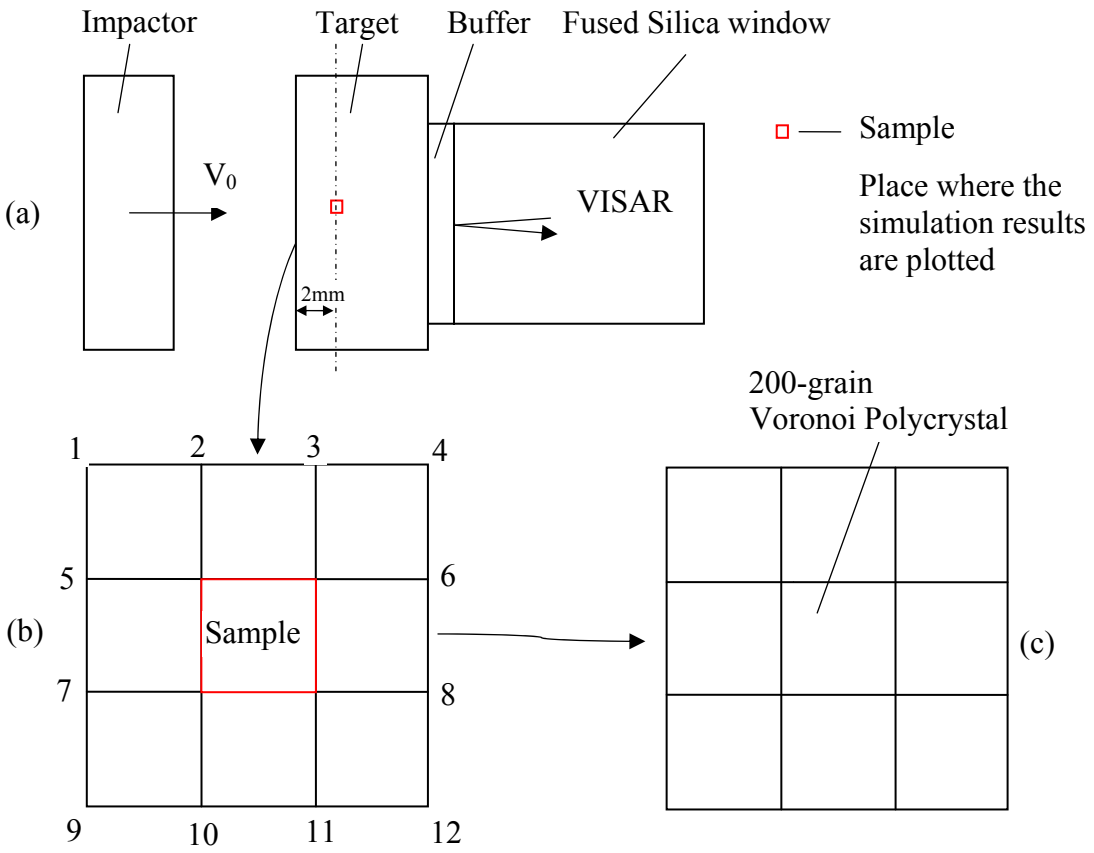

Figure 2.8: Schematic illustration of multiscale modeling: (a) Configuration for plate impact simulation; (b) Homogeneous Sub-domain (9 elements for plate impact simulation) and sample at macroscopic scale; (c) Voronoi Polycrystal (sample at mesoscale) for sub-domain central region.

(Zhang, 2005). The parameters of λ^0 = 140.70 GPa, μ^0 = 160.03 GPa, B = 5.06, p_0 = -0.8 GPa, β = 32.64°, q_0 = 4.34 GPa and α = 1.5 are used for the calculation. A computed wave profile of the velocity between buffer and window is plotted to compare well with the experimental measurement data by adjusting these parameters. The displacement histories of the homogeneous sub-domain boundary nodes (The nodes of 1 to 12 in Figure 2.8 (b)) are recorded and used as the dynamic boundary conditions in the mesoscopic analysis of heterogeneous sub-domain. The stress-strain curve of sample is plotted. The details of results are described in Section 2.4.2.

Second, the 2-D and 3-D mesoscopic analyses of heterogeneous sub-domain are carried out by using ABAQUS/Explicit (2-D) and Standard (3-D). For 2-D analysis, a plate of heterogeneous sub-domain is constructed with a very small thickness and meshed. Figure 2.9 (a) shows the mesh and boundary conditions. A coarser mesh is generated in all around homogeneous parts and the mesh size decreases towards the center region of heterogeneous sub-domain which is polycrystal crystal overlaid with a very fine, grain-wise constructed, microstructure-preserving mesh. The displacement histories of the boundary nodes obtained from plate impact simulation are used as dynamic boundary conditions in x and y direction. The displacements of surface nodes in z-direction are prevented. Figure 2.9 (b) shows the zoom of polycrystal mesh and coupling between polycrystal and the rest homogeneous parts which share the same nodes in four lateral surfaces. For 3-D analysis, a cube of heterogeneous sub-domain with the center of a 600 grain 3-D polycrystal crystal model and all around homogeneous parts are constructed and meshed. Figure 2.10 shows the FE model with mesh. A much coarser mesh is created

in all around homogeneous parts and the mesh size decreases towards the center region of heterogeneous sub-domain which is a 3-D polycrystal crystal overlaid with a very fine, grain-wise constructed, microstructure-preserving mesh. The boundaries of nodes of four lateral surfaces are applied in x and y positions as the same displacement levels which are obtained by the result histories through 2-D analysis with different levels of impact velocities. Also in z-direction the displacements of the surface nodes are prevented. 3-D polycrystal model is coupled with the all-round homogeneous parts by sharing the nodes of six outside surfaces.

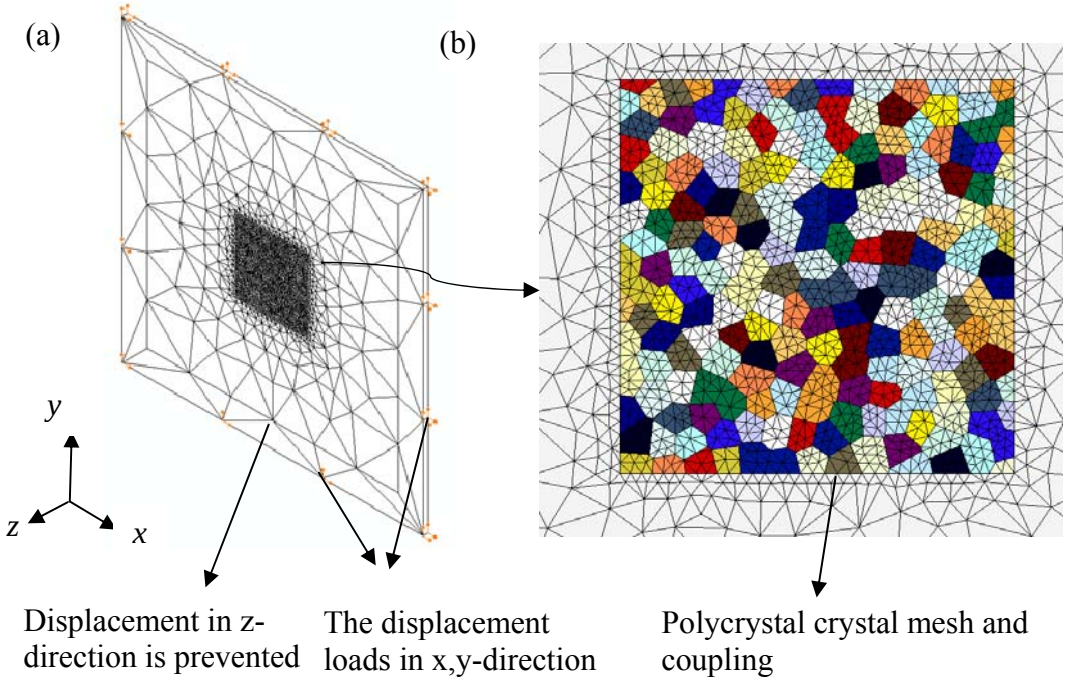

Figure 2.9: The 2-D FE model of heterogeneous sub-domain: (a) mesh and boundaries, and (b) zoom of polycrystal crystal mesh and coupling.

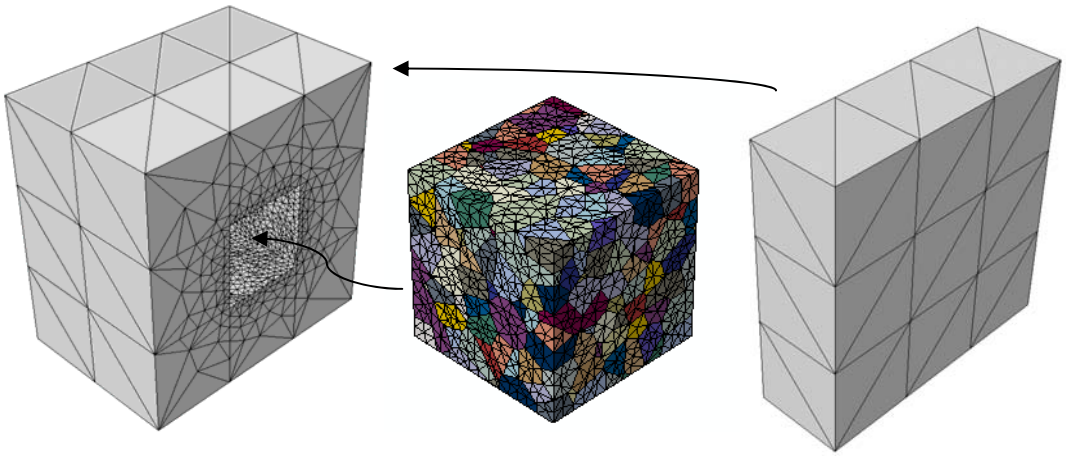

Figure 2.10: The 3-D FE model of heterogeneous sub-domain: (a) mesh of the two left sides and coupling, (b) 3-D polycrystal crystal mesh, and (c) mesh of the right side.

Material modeling. The mesosopic polycrystal analysis takes into account the material models of nonlinear crystal elasticity, crystal microplasticity by basal and prismatic slips, and the strength model of macroscopic material (see section 2.3).

Nonlinear elasticity. A ceramic can display noticeable stiffening in elastic bulk response when the material is deformed under uniaxal-strain compression. An accurate description requires at least a second-order formulation. Anisotropic elastic response of a single crystal can be represented by a finite-strain formulation (Horn and Gupta, 1989), in which the Cauchy stress σ_{ij} is defined as a function of Green strain ε_{ij}^{G} and second- and third-order isentropic elastic constants, C_{ijkl} and C_{ijklmn}, i.e.,

$$\sigma_{ij} = \frac{1}{J} F_{ik} F_{jl} \left(C_{klmn} \varepsilon_{mn}^{G} + \frac{1}{2} C_{klmnpq} \varepsilon_{mn}^{G} \varepsilon_{pq}^{G} \right), \; i, j, k, l, m, n, p, q = 1, 2, 3, \qquad (2.43)$$

where $F_{ij} = \partial x_i / \partial X_j$ is the deformation gradient with x_i and X_i denoting the current and initial configurations respectively. $J = \det \mathbf{F}$ is the Jacobian for the transformation between the two coordinate systems. The Green strain is defined by

$$\varepsilon_{ij}^{G} = \frac{1}{2} \left(\frac{\partial x_k}{\partial X_i} \frac{\partial x_k}{\partial X_j} - \delta_{ij} \right), \qquad (2.44)$$

where δ_{ij} is the Kronecker delta.

Al_2O_3 single crystal with trigonal symmetry has 6 independent second-order elastic constants and 14 independent third-order ones. The experimental measurement for these constants is given by Hankey and Schuele (1970), as shown in Table 2.1.

Crystal plasticity. The model parameters for crystal plasticity are based on the assumption of rate-independent and non-hardening microplasticity (Zhang et al., 2005). A value of 1×10^{-3} s^{-1} is used for $\dot{\gamma}_0$, the selection of which is free for a very large *k*. To model a non-hardening plasticity, the saturated shearing stress τ_s in Eq. (2.10a) is assumed 0.2% greater than the critical resolved shearing stress (CRSS) τ_c, and the initial hardening parameter h_0 is given a value of 1.0 GPa. Hence, hardening moduli $h_{\alpha\beta}$ approach zero rapidly with increasing γ. Consequently, the latent hardening parameter *q* becomes insignificant and is given a value of 1.

Table 2.1: Independent second- and third-order elastic constants for Al_2O_3 with trigonal symmetry.

Second-order elastic constants (GPa)		Third-order elastic constants (GPa)			
C_{1111}	496.8	C_{111111}	-3870.0	C_{113323}	-131.0
C_{1122}	163.6	C_{111122}	-1090.0	C_{112323}	-302.0
C_{1133}	110.9	C_{111133}	-963.0	C_{111313}	-1160.0
C_{1123}	-23.5	C_{111123}	55.0	C_{222222}	-4520.0
C_{3333}	498.1	C_{112233}	-289.0	C_{333333}	-3340.0
C_{2323}	147.4	C_{112223}	-39.0	C_{332323}	-1090.0
		C_{113333}	-922.0	C_{232323}	-19.0

The inelastic deformation and effective strength model of polycrystalline Al_2O_3 under shock compression are analyzed, and the 2-D and 3-D polycrystal models as well as the material models are verified. The results are presented in Section 2.4.2.

2.4.2 Results of Multiscale Modeling Analysis

Plate impact simulation. In comparison with the experimental measurement data (Munson and Lawrence, 1979), the computed particle velocity profile between buffer and window is plotted in Figure 2.11. The computed data compare well with the

experimental measurement data. The parameters of homogeneous material model are verified so that they can be used in the dynamic analysis.

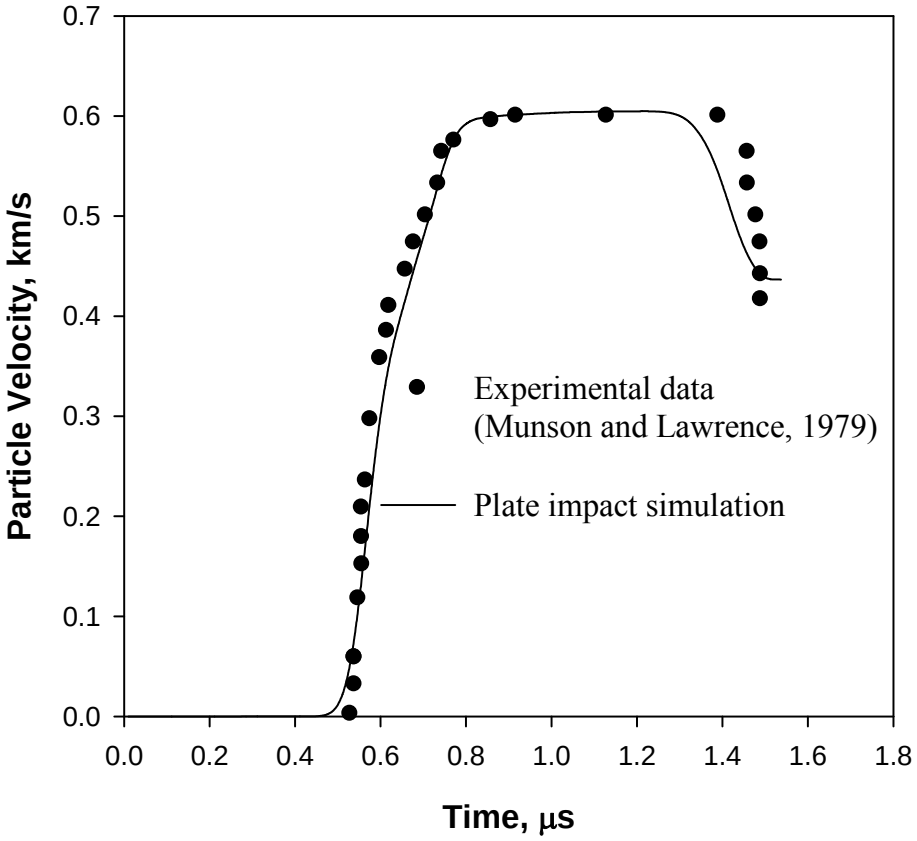

Figure 2.11: Compared the computed wave profile of velocity for plate impact simulation with experimental measurement data.

Mesoscopic analysis The results of 2-D and 3-D mesoscopic polycrystal analysis of the mean stress response, the macroscopic longitudinal stress and lateral stress compared with those of sample for plate impact simulation are predicted and shown in Figure 2.12. The results are based on basal slip and prismatic slip with $\tau_{cb} = 2.7$ GPa and $\tau_{cp} = 3.3$ GPa. The following three significant points can be made. First, the longitudinal

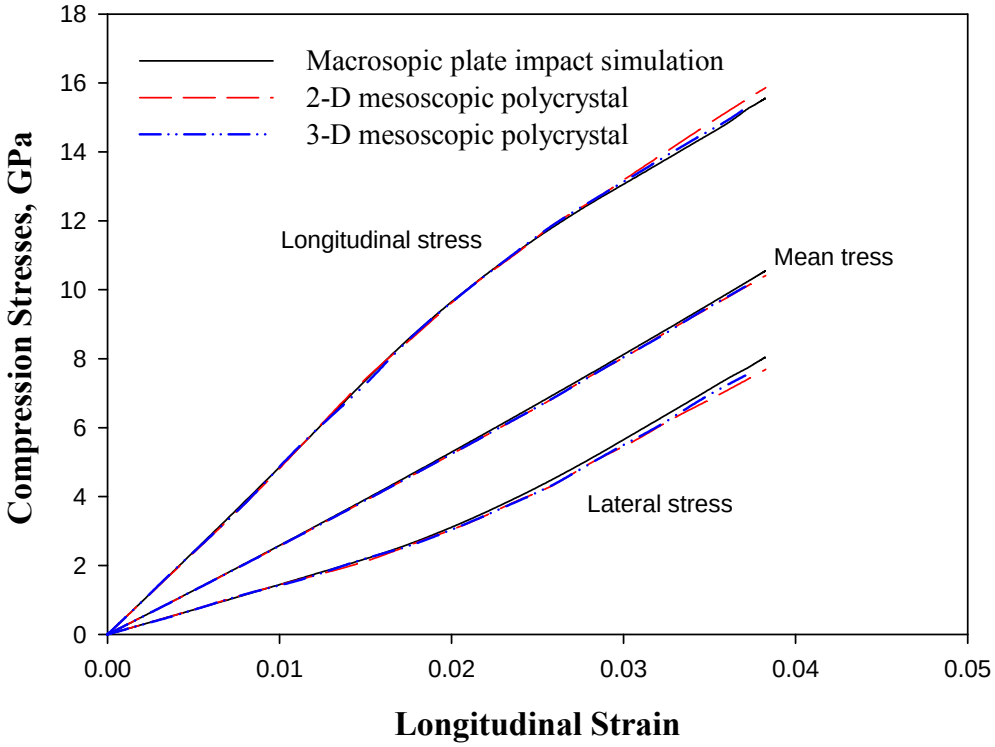

Figure 2.12: Compared the longitudinal stress, mean stress and lateral stress response of 2-D and 3-D mesoscopic polycrystal analysis with those of sample for plate impact simulation.

stresses based on mesoscopic analysis compare very well with that of plate impact simulation above Hugoniot elastic limit (HEL), which is 9.1 GPa. Second, mean stress, the longitudinal and lateral stress based on mesoscopic analysis compare closely with those computed in plate impact simulation. The longitudinal displays a little stiffer and the lateral stress displays a little softer beyond the HEL. Third, the results of 2-D and 3-D mesoscopic analysis have the same prediction of longitudinal and mean stress. It can observe that the stresses response can be well characterized by the parameters of crystal elastic and plastic model as well as macroscopic homogeneous material model.

The contour plots of the effective plastic strain (see Eq. 2.40) fields of 2-D mesoscopic polycrystal crystal analysis at four stress states: (a) $\sigma_x = 8.39GPa$, (b) $\sigma_x = 9.43GPa$, (c) $\sigma_x = 12.65GPa$, and (d) $\sigma_x = 16.08GPa$ are shown in Figure 2.13. The same intensity scale is used for different stress states. The calculated HEL is about 9.1 GPa. From the plot for 8.39 GPa (a) shock stress, which is the predicted HEL, the material is seen to have very small plastic strains (0.1 to 0.2%) in a few isolated crystals (due to pre-HEL microplasticity). In the plot at little above HEL 9.43 GPa (b), there exists a small amount of slipped crystals, but the intensity of plastic strain is still small. The evolution of microplasticity from (b) to (c) is rapid. At stress state 12.65 GPa (c), more crystals are deformed with increased intensity of plastic strain with basal slip. The plastic deformation is clearly heterogeneous displaying a nonuniform distribution of plastically deformed grains and large variations in $\bar{\varepsilon}^p$. The plot for 16.08 GPa shock stress (d) shows a $\bar{\varepsilon}^p$ field that is much greater in intensity due to the activation of prismatic slip but the similar in the morphology of plastic region as that shown in (c). In

other words, intragranular microplasticity is greatly intensified but with little initiation of new slip sites and a fraction of the crystals remains elastic, giving rise to a significantly stronger heterogeneity. Also the contour plots of the effective plastic strain fields in x-

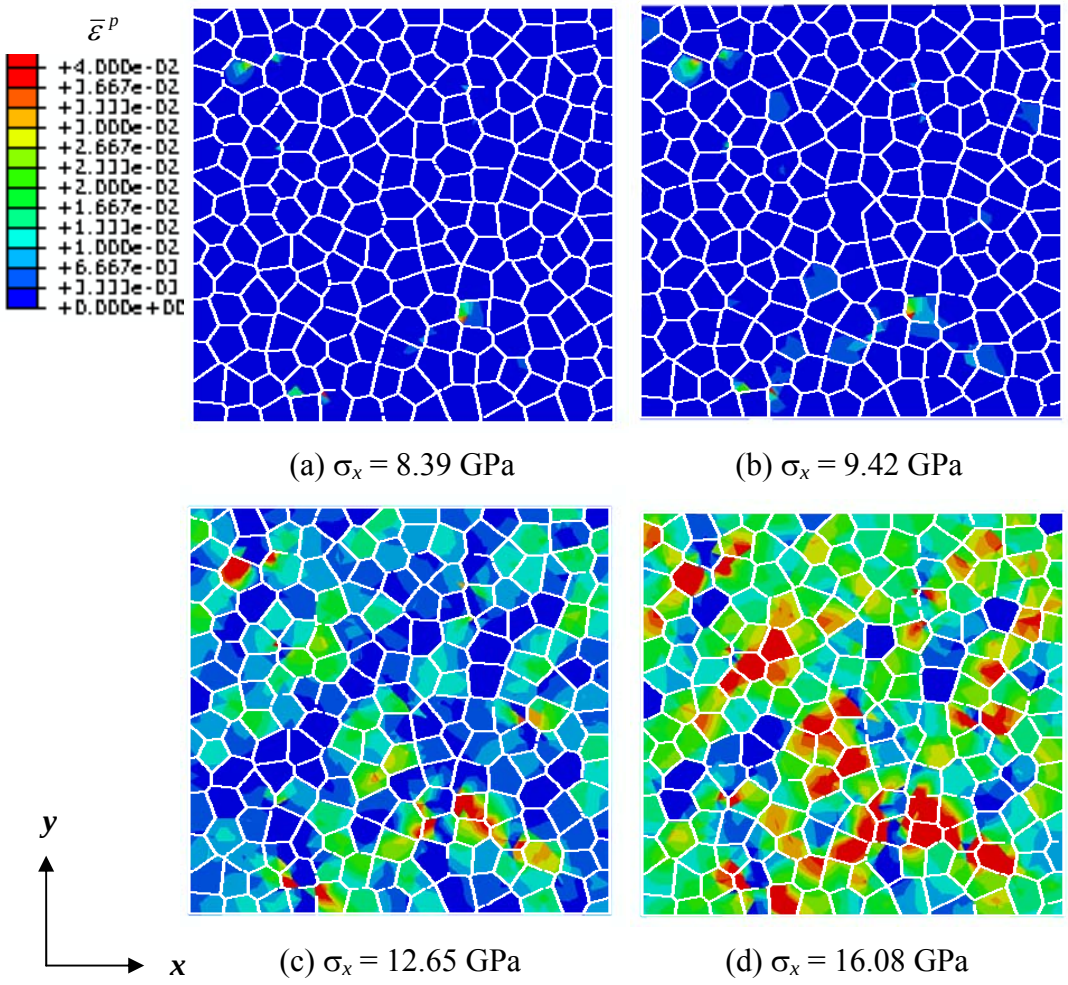

(a) σ_x = 8.39 GPa (b) σ_x = 9.42 GPa

(c) σ_x = 12.65 GPa (d) σ_x = 16.08 GPa

Figure 2.13: Contour plots of effective plastic strain field in polycrystalline alumina of 2-D mesoscopic polycrystal analysis at four different stress states: (a) σ_x = 8.39 GPa, (b) σ_x = 9.42 GPa, (c) σ_x = 12.65 GPa, and (d) σ_x = 16.08 GPa.

cut plane of 3-D mesoscopic polycrystal analysis at three stress states: (a) $\sigma_x = 8.49GPa$, (b) $\sigma_x = 12.80GPa$, and (c) $\sigma_x = 16.18GPa$ are shown in Figure 2.14.

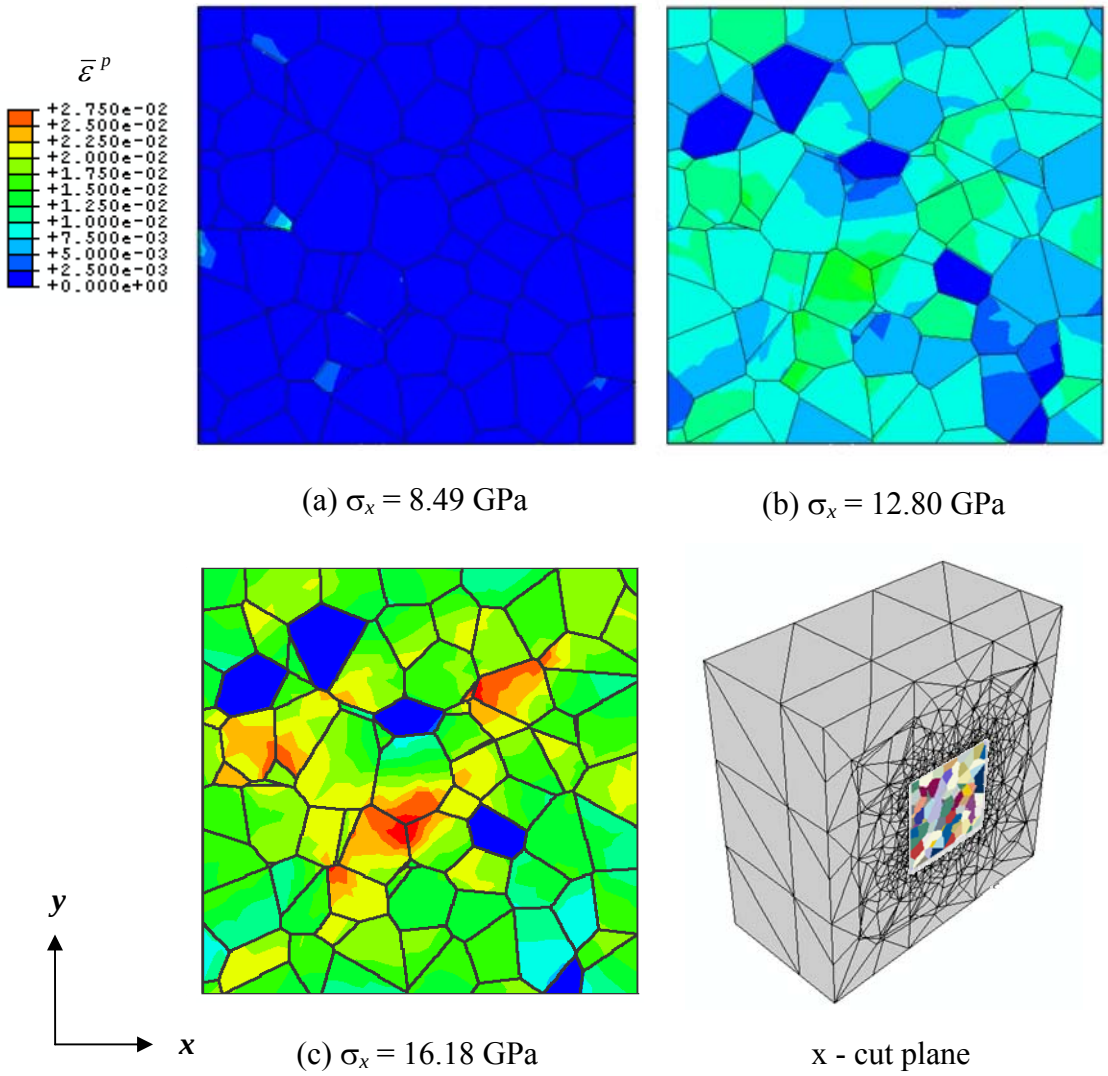

Figure 2.14: Contour plots of effective plastic strain field in polycrystalline alumina in x-cut plane of 3-D mesoscopic polycrystal analysis at three different stress states: (a) σ_x = 8.49 GPa, (b) σ_x = 12.80 GPa, and (c) σ_x = 16.18 GPa.

Figure 2.15 shows the statistical distributions of normalized longitudinal stress calculated by mesoscopic polycrystal finite element method using 2-D plate model (a, b) and 3-D model (c, d). Compressions under two macroscopic longitudinal stresses are

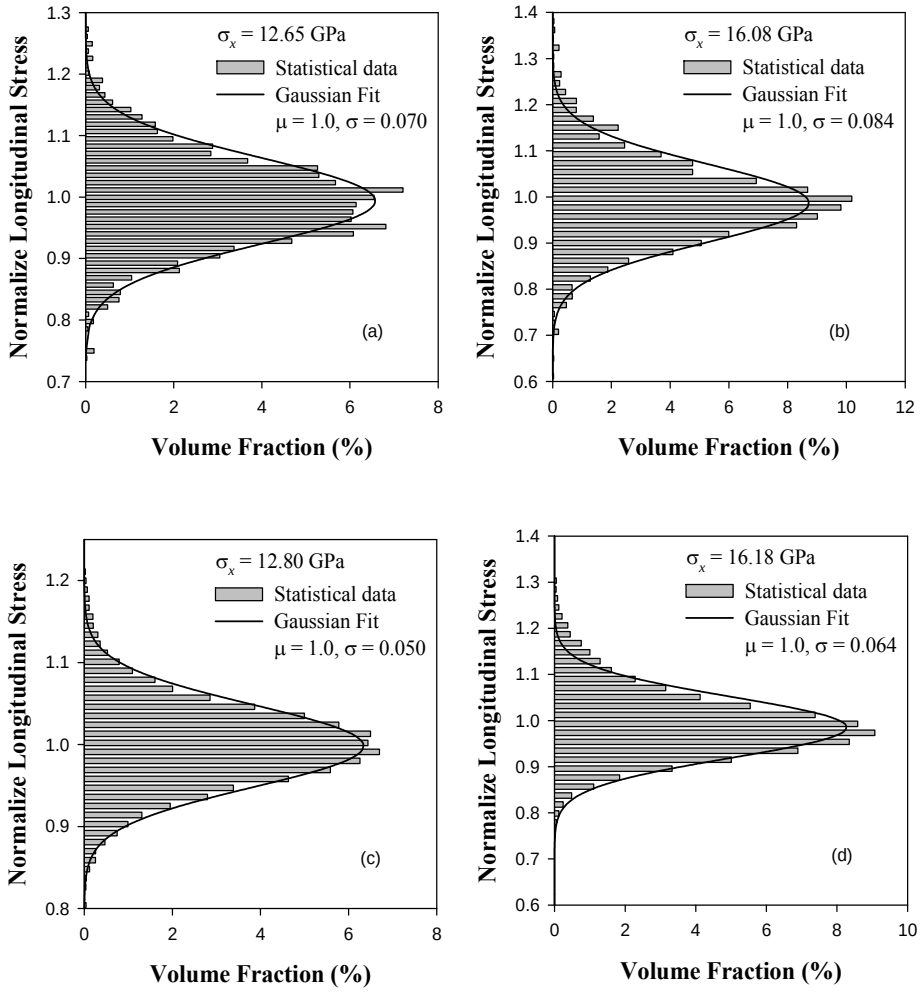

Figure 2.15: Statistical distribution of normalized longitudinal stress calculated by mesoscopic polycrystal analysis using finite element method using 2-D plate model (a, b) and 3-D cube model (c, d).

considered: 12 GPa (12.65 GPa for Figure (a) and 12.80 GPa for Figure (c)), which is right above the HEL; and 16 GPa (16.08 GPa for Figure (b) and 16.18 GPa for Figure (d)). Mean value μ and standard deviation σ of Gaussian curves are also shown in the figures to present the stress variations. The Gaussian fits superimposed on the histograms show that all the distributions are essentially Gaussian, and the distributions for 3-D model (c, d) fit Gaussian best. Both distributions are apparently Gaussian-like with good matches between the statistical data and their best Gaussian fit (the lines). The results suggest that a good statistical representation can be achieved with the 200-grain square-plate or 600-grain cubic VP-FE models. Therefore, a 200-grain square (2-D) Voronoi polycrystal model is used in all the 2-D micromechanical analyses presented in the rest of the dissertation, and each 3-D micromechanical analysis presented in the rest of this dissertation employs a 600-grain cubic model.

Numerical simulations using the microstructure and material models have been carried out to investigate the inelastic deformations and compression strengths of polycrystalline ceramics under shock compression. The continue study of polycrystalline α-Al_2O_3 (Lucalox) with microstructural model with different slip systems is presented and the results are discussed in Chapter 3. The results of the strength analysis of polycrystalline AD995 are presented and discussed in Chapter 4. The results of strength analysis of polycrystalline AlON are presented and discussed in Chapter 5.

CHAPTER 3

SHOCK STRENGTH OF DENSE POLYCRYSTALLINE α–PHASE ALUMINUM OXIDES (LUCALOX)

3.1 Introduction

Among the tested aluminas, the most commonly used is Lucalox, a commercially available polycrystalline α-phase aluminum oxides (α-Al_2O_3) with a high purity of 99.9% and full density. For decades, its longitudinal response under shock wave compression was measured by several researchers (e.g., Longy and Cagnoux, 1989; Munson and Lawrence, 1979; Murray, et al., 1996), and its HEL measured by Munson and Lawrence (1979) is ~9 GPa. However, longitudinal measurements alone cannot determine the material strength, nor further identify the underlying micromechanisms. The material strength and the inelastic deformation mechanism of polycrystalline α-Al_2O_3 have been studied in the previous work in our group by Zhang (2005) by using a 100-grain square polycrystal model. In the previous work, polycrystal modeling methodology and technique with finite element analysis have been developed for polycrystalline α-Al_2O_3, and the result shows that the simulated macroscopic compressive strength response

compare well with the experimental measurement by considering material model of nonlinear elastic and crystal plasticity with slip systems of basal and pyramidal slips (prismatic slip is not considered). However there is an issue of interest: what is the effect of prismatic slip because some researchers have showed that prismatic slip is more important and easily activated than pyramidal slip (Cadoz et al., 1984; Heuer et al., 1998)? Considering basal and prismatic slips for polycrystalline a-Al_2O_3 under shock stresses is significantly higher than its HEL. Hence, a further analysis of compressive strength of polycrystalline α-Al_2O_3 by considering basal and prismatic slip is needed to solve the issue.

To investigate the effect of prismatic slip, the analysis of compressive strength of polycrystalline α-Al_2O_3 is continued. 200-grain crystal square FE model are employed in this analysis. The material model considers nonlinear elasticity, crystal plasticity and effective strength model that are used in the previous work (Zhang, 2005). Model parameters are also obtained. Both basal slip and prismatic slip are considered. The FE model and the material model are implemented into ABAQUS/Explicit code with User-material Subroutine for FE analysis. A 3-D microstructure modeling by finite element method is presented in section 3.2. The material model and parameters are presented in section 3.3. Microplasticity analysis and results are presented in section 3.4. Section 3.5 summarizes the key findings of the study presented in this chapter.

3.2 3-D Modeling by Finite Element Method

The modeling methodology consists of three components: (1) a realistic 3-D model of polycrystalline microstructure, (2) a material model including compression-dependent elastic stiffening and crystal plasticity, and (3) a solution algorithm to implement the microstructure and material model into the commercial FE code the ABAQUS/Standard for numerical analysis.

Microstructural modeling. The polycrystalline microstructure is modeled using a cubic (3-D) VP-FE model with 600 grains, as shown in Figure 3.1. Since the loading condition is uniaxial-strain compression, uniform pressure is applied on the front surface

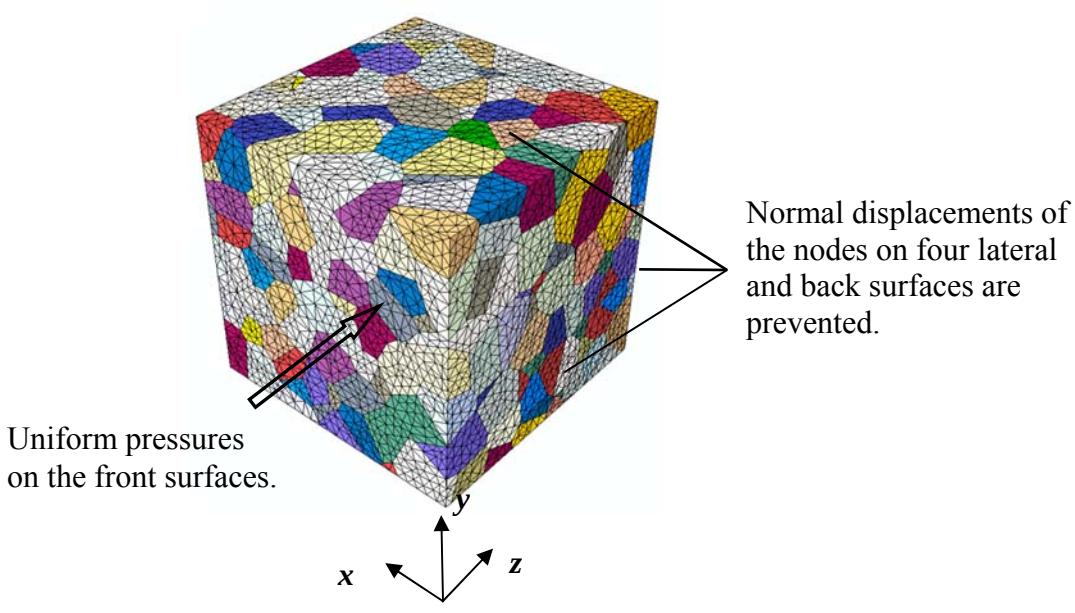

Figure 3.1: 3-D polycrystal, microstructure-preserving FE mesh, and boundaries conditions.

of the polycrystal, while the back surface is fixed normally and the transverse displacements are prevented at the four lateral surfaces. Each Voronoi cell is assigned a random crystallographic orientation to represent crystal properties of the modeled material

Nonlinear elasticity. A ceramic can display noticeable stiffening in elastic bulk response when the material is deformed under uniaxal-strain compression. An accurate description requires at least a second-order formulation. Anisotropic elastic response of a single crystal can be represented by a finite-strain formulation (Horn and Gupta, 1989), as described by Eqs. (2.43-2.44) in Section 2.4.1. α-Al_2O_3 single crystal with trigonal symmetry has 6 independent second-order elastic constants and 14 independent third-order ones. The experimental measurement for these constants is given by Hankey and Schuele (1970), as shown in Table 2.1.

Crystal plasticity model (see section 2.3.2). The selection of constitutive parameters for crystal plasticity is based on the assumptions of rate-independent non-hardening plasticity. Zhang et al. (2005) have carried out a series of FE simulations and a parametric study and found that model simulations with the following parameters provides the best overall match to the experimental data. That results in a very large *k* in Eq. (2.7), which forces a negligibly small variation of $\tau$with $\dot{\gamma}$. A value of 1×10^{-3} s^{-1} is used for $\dot{\gamma}_0$, the selection of which is free for a very large *k*. To model a non-hardening plasticity, the saturated shearing stress τ_s in Eq. (2.10a) is assumed 0.2% greater than the critical resolved shearing stress (CRSS) τ_c, and the initial hardening parameter h_0 is

given a value of 1.0 GPa. Hence, hardening moduli $h_{\alpha\beta}$ approach zero rapidly with increasing γ. Consequently, the latent hardening parameter q becomes insignificant and is given a value of 1. Two slip conditions are considered in the numerical simulations: (1) prismatic slip $\{10\bar{1}0\}\langle 11\bar{2}0\rangle$ only with the CRSS τ_{cp} = 2.7 GPa and (2) both primary prismatic slip $\{10\bar{1}0\}\langle 11\bar{2}0\rangle$ and second basal slip $\{0001\}\langle 11\bar{2}0\rangle$ with CRSS's of $\tau_{cp} = 2.7$ GPa and $\tau_{cb} = 3.3$ GPa. Figures 2.1 represent the slip planes and slip directions for the basal, prismatic and pyramidal systems, respectively.

3.3 Microplasticity Analysis and Results

Numerical simulations for mean stress response, the macroscopic longitudinal stress and lateral stress of polycrystalline α-Al_2O_3 deformed under uniaxial-strain compression are carried out based on a 200-grain 2-D Voronoi polycrystal model. The microstructural model and material model are implemented into ABAQUS/Explicit code for FE analysis. Mean stress response, the macroscopic longitudinal stress and lateral stress based on prismatic slip only and both basal slip and prismatic slip conditions are predicted and the results are shown in Figure 3.2. Mean stress response (solid line) and experimental longitudinal stress data (Munson and Lawrence, 1979, as scattered dots) are shown in the figure for comparison. The results of considering both basal slip and pyramidal slip conditions are also shown for comparisons (Zhang, 2005). The following fifth significant points can be made. First, the calculations predict the same mean stress response as the experimental data. Second, the calculations by prismatic slip alone with $\tau_{cp} = 2.7$ GPa are the same those by basal slip with $\tau_{cb} = 2.7$ GPa, which can capture the

transition to the softer response at HEL, and the calculated value for HEL is 9 GPa, which agrees well with the experimental measurement of 9.1 GPa (Munson and Lawrence, 1979) Third, the longitudinal stress calculations based on prismatic slip alone

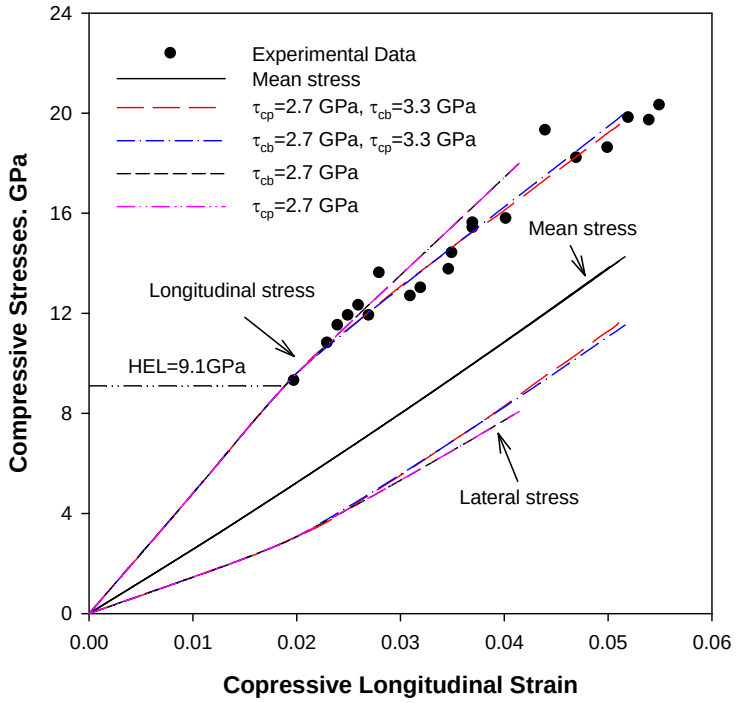

Figure 3.2: Macroscopic longitudinal, mean and lateral stress response of polycrystalline α-Al_2O_3.

compare well with the experimental data up to a compressive longitudinal strain of 0.029, the corresponding longitudinal stress at which is ~ 13 GPa, about 1.4 × HEL. In addition, the longitudinal stress response displays a stiffening behavior and the lateral stress

response displays a softening behavior beyond the HEL. Fourth, the activations of second basal slip make the longitudinal stress response softer and lateral stress response stiffer. Model predictions compare better with experimental data than those predicted by basal slip or prismatic slip alone. This suggests that only one slip alone may not be sufficient for explaining the inelastic behavior of alumina, especially beyond 1.4 times the HEL. Fifth, beyond 2 × HEL, model predictions based on both primary prismatic and second basal slip are the same as those of both primary basal and second prismatic slip. It can be said that the influence of prismatic slip on shocked alumina has the same as basal slip, In fact, the macroscopic response of shocked alumina is well captured by model simulations using both primary prismatic $\tau_{cp} = 2.7$ GPa and second basal slip and $\tau_{cb} = 3.3$ GPa up to a longitudinal of 20 GPa or about 2.2 times the HEL.

Figure 3.3 (a) - (c) plot the statistical distribution of longitudinal stress for the same stress states at 13.98 GPa by considering different slip systems: (1) Prismatic slip only and τ_{cp} = 2.7 GPa; and (2) Primary prismatic slip $\tau_{cp} = 2.7$ GPa and second basal slip with $\tau_{cb} = 3.3$ GPa; The volume- averaged stress response can be viewed as an accurate representation for the macroscopic response of the material. It can be observed that the longitudinal stress distributions are Gaussian-like, and combined prismatic slip and basal slip cause less heterogeneity than prismatic slip only.

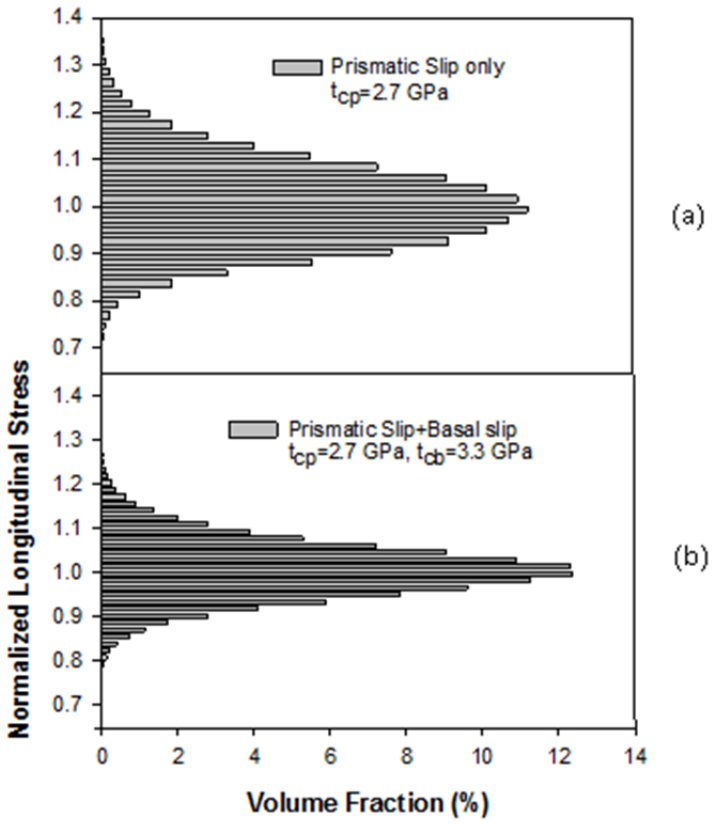

Figure 3.3: Statistical distributions of longitudinal stress in polycrystalline α–Al_2O_3 at σ_x =13.98 GPa by considering different slip systems: (a) Prismatic slip only, and (b) prismatic+ basal slips.

3.4 Summary

In this chapter, the compression strength of polycrystalline α-Al_2O_3 under dynamic loading has been studied computationally using the 3-D 600-grain plate VP-FE model, and the effect of different slip systems are investigated. The material model considers nonlinear anisotropic and crystal elasticity. The material model parameters are used from the previous work. The slip systems consider basal only, both basal and prismatic slip, and both basal and pyramidal slip. The microstructure and material models have been implemented into ABAQUS/Explicit for finite element analysis.

Numerical results for the analysis of polycrystalline α-Al_2O_3 show that: (1) The calculations by prismatic slip alone are the same those by basal slip alone. Microplasticity by prismatic slip only alone is adequate only near the HEL but underestimates post-HEL softening; (2) The model predictions by prismatic (primary) and basal (second) slips and those predicted by basal (primary) and pyramidal (second) slip compare better with experimental data than those predicted by prismatic or basal slip alone; They compare well with experimental data up to a longitudinal of 20 GPa or about 2.2 times the HEL.

CHAPTER 4

SHOCK STRENGTH OF 3% POROUS POLYCRYSTALLINE α–PHASE ALUMINUM OXIDES (AD995)

4.1 Introduction

Polycrystalline AD995, another α–phase aluminum oxide ceramic, is one of the most widely used and studied advanced ceramic materials used for impact protection. It is composed of 99.5% polycrystalline alumina with a small amount of aluminosilicate glass (0.5%) and has 97% density due to 3% porosity in the ceramic. As an alternative to pure and dense polycrystalline α-Al_2O_3, polycrystalline AD995 has a relative abundance and low-cost material resource that is advantageous for commercial applications. The HEL of AD995 has been measured by some researchers (eg., Dandeka and Bartowski, 1993; Reinhart and Chhabildas, 2003), and the measured value varies from 6.7 to 7.9 GPa. However, compared with pure and dense α-Al_2O_3, which has extremely high effective shock strength, AD995 has 15-30% reduction in the Hugoniot elastic limit (HEL) and more signification reduction in the post-HEL strength (Dandekar & Bartowski, 1993; Reinhart & Chhabildas, 2003). It is not yet clear whether this is caused by glassy grain boundaries, voids or something else. To examine compressive strength of polycrystal

AD995 alumina under dynamic loading and understand its inelastic deformation behavior, numerical studies using Voronoi polycrystal modeling in conjunction with finite element analysis are carried out. Modeling and analysis of strength of polycrystalline AD995 Alumina under dynamic loading are presented in this chapter.

The material model considers nonlinear anisotropic crystal elasticity, crystal plasticity and deformation twinning, which is presented in Section 4.2. Crystal plasticity model that is extending to allow modeling and simulation of crystal slip and crystal deformation twinning is described in this section. The constructions of 2-D porous VP-FE models and the study of their performances are presented in Section 4.3. Three types of 2-D porous VP-FE models with triangular, square and random-shape voids are examined in this section. The studies to examine the roles of glassy grain boundaries and voids are presented in Section 4.4.1 and 4.4.2. The grain boundary are treated as a glassy second phase to examine the effects of weaker grain boundary and AD995 is approximated as pure alumina with 1~3% porosities to investigate the role of voids. Microplasticity analysis and results of strength of polycrystalline AD995 under shock compression are presented in section 4.4.3. To compare well with the experimental measurement, numerical simulations for strength response of shocked AD995 by using combined deformation twinning and crystal slip with lower threshold are carried out. Section 4.5 summarizes the key finding of the computational studies presented in this chapter.

4.2 Material Modeling and Parameters

Like pure and dense α-Al_2O_3, the material modeling of AD995 also consists of nonlinear anisotropic crystal elasticity, crystal plasticity and grain boundary model, which are presented in chapter 2. The parameters of material modeling are approximated as those of pure and dense α-Al_2O_3. The selections of material modeling parameters are presented as the followings.

Nonlinear crystal elasticity. AD995 has the same parameters as pure and dense α-Al_2O_3. The model parameters for the nonlinear crystal elasticity include 6 independent second-order elastic constants and 14 independent third-order ones, as shown in Table 2.1.

Crystal plasticity. The selection of constitutive parameters for crystal plasticity model is based on the assumptions of rate-independent non-hardening plasticity, and same values are selected as those used for pure and dense Al_2O_3 [see Section 3.3]. We use the selected parameters and consider two slip systems and a deformation twinning in the numerical simulations. The microplasticity model of basal twinning and slip systems are: (1) prismatic (primary) $\{0001\}\langle 11\bar{2}0\rangle$ and basal slip (second) $\{0001\}\langle 11\bar{2}0\rangle$ with the CRSS's of $\tau_{cp} = 2.7$ GPa and $\tau_{cb} = 3.3$ GPa; (2) basal twinning $\{0001\}\langle 10\bar{1}0\rangle$ and prismatic slip with CRSS's of $\tau_{cbtw} = 2.7$ GPa and $\tau_{cp} = 3.3$ GPa. Figures 2.1(a) and (b) represent the slip planes and slip directions for the basal and prismatic systems, respectively. In order to describe more accurate finite shear strains, a deformation twinning system is considered with the two slip systems since deformation twinning is an important deformation mode of AD995 (A. He et al., 2002). The deformation twinning is

assumed as basal twinning $\{0001\}\langle 10\bar{1}0\rangle$. The relevant system for basal twinning is shown in Figure 4.1.

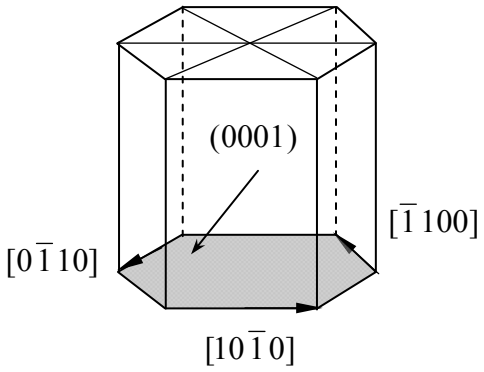

Figure 4.1: Basal twinning

Crystal plasticity model is extended to allow modeling and simulation of crystal slip and crystal deformation twinning. The associated equations for slip and twinning systems are described in below. The rate of plastic strain with respect to crystal axis is calculated by: (1) For active slip system with inactive twinning,

$$\dot{\boldsymbol{\varepsilon}}_{sl}^{p} = \sum_{\alpha=1}^{n^{sl}} \mathbf{P}^{(\alpha)} \dot{\gamma}^{(\alpha)} \ . \tag{4.1}$$

where $\dot{\boldsymbol{\varepsilon}}_{sl}^{p}$ is the rate of plastic strain for slip system, n^{sl} is the total number of slip system, $\mathbf{P}^{(a)}$ is the Schmid direction tensor of $\alpha-$slip system, and $\dot{\gamma}^{(a)}$ is the rate of plastic shear strain of the $\alpha-$slip system. The calculations of $\mathbf{P}^{(a)}$ and $\dot{\gamma}^{(a)}$ as well as relative variables have been described in Chapter 2 [see Eq.(2.2)~Eq.(2.5)].

(2) For active slip system with active twinning,

$$\dot{\boldsymbol{\varepsilon}}_{tw}^{p} = (1-\sum_{\beta=1}^{n^{tw}} f^{(\beta)})\sum_{\alpha=1}^{n^{tw}} \mathbf{P}^{(\alpha)}\dot{\gamma}^{(\alpha)} + \sum_{\beta=1}^{n^{tw}} \dot{f}^{(\beta)} P^{(\beta)}\gamma_{tw} \,. \tag{4.2}$$

where $\dot{\boldsymbol{\varepsilon}}_{tw}^{p}$ is the rate of plastic strain for twin system, n^{tw} is the total number of twin system, $\mathbf{P}^{(\beta)}$ is the Schmid direction tensor of $\beta-$twin system, which is calculated by

$$\mathbf{P}^{(\beta)} = \frac{1}{2}(\mathbf{m}^{(\beta)} \otimes \mathbf{n}^{(\beta)} + \mathbf{n}^{(\beta)} \otimes \mathbf{m}^{(\beta)}) \,, \tag{4.3}$$

here $\mathbf{m}^{(\beta)}$ and $\mathbf{n}^{(\beta)}$ are respectively the unit vector of twinning direction and that normal to the twin plane of the $\beta-$twin system, $\dot{f}^{(\beta)}$ denotes the evolution of the deformation twinning volume fraction and is calculated by

$$\dot{f}^{(\beta)} = \frac{\dot{\gamma}_0}{\gamma_{tw}} \mathrm{sgn}(\tau^{(\beta)}) \left| \tau^{(\beta)} / g^{(\beta)} \right|^{k} . \tag{4.4}$$

where $\dot{\gamma}_0$ is the reference shear rate and set as $0.001\mathrm{s}^{-1}$, k is the rate sensitivity parameter and assumed to be the same as slip deformation, γ_{tw} is the constant shear strain associated with twinning and equal to 0.635 (Pirouz and Lawort et al., 1994), $\tau^{(\beta)}$ is the shear stress resolved on the $\beta-$twinning system, i.e.,

$$\tau^{(\beta)} = \mathbf{P}^{(\beta)} : \boldsymbol{\sigma} \,, \tag{4.5}$$

and $g^{(\beta)}$, which measures the system strain hardening, uses the initial critical resolved shear stress (CRSS) τ_{ctw} as the starting value and evolves as:

$$\dot{g}^{(\beta)} = \sum_{\beta=1}^{n^{tw}} h_{tw}\gamma_{tw}\dot{f}^{(\beta)} \,, \tag{4.6}$$

where $\gamma_{tw}\dot{f}^{(\beta)}$ denotes the equivalent shear rate of the $\beta-$twinning system, and h_{tw} is the twinning-plane hardening moduli. Assume no coupling between different types of twin systems, and no coupling between twin systems and slip systems. The value of h_{tw} is (Hutchinson, 1976):

$$h_{tw} = h_0 \sec^2\left(\frac{h_0\gamma_{tw}^{\beta}}{\tau_{stw}-\tau_{ctw}}\right), \tag{4.7}$$

here h_0 is the initial hardening rate and the same as value of slip system, τ_{stw} is the maximum value of critical resolved shear stress and assumed 0.2% greater than the critical resolved shearing stress (CRSS) τ_{ctw}, which is considered roughly to be equal to that of basal slip (Tymiak & Gerberich, 2007), and γ_{tw}^{β} is a measure of the cumulative plastic shear strain calculated by summing the contributions from all n^{tw} twin systems, i.e., we define γ_{tw}^{β} at the time *t* by

$$\gamma_{tw}^{\beta}(t) = \int_0^t \sum_{\beta=1}^{n^{tw}} \gamma_{tw}\Delta f^{(\beta)}(t)dt\,, \tag{4.8}$$

and $f^{(\beta)}$ is the volume fraction of the $\beta-$twin system. The twin fraction $f^{(\beta)}$ at time *t* is calculated by

$$f^{(\beta)}(t) = \frac{\gamma_{tw}^{\beta}(t)}{\gamma_{tw}}\quad . \tag{4.9}$$

And the total rate of plastic strain $\dot{\boldsymbol{\varepsilon}}^{p}$ is the sum by Eq. (4.1) and Eq.(4.2)

$$\dot{\boldsymbol{\varepsilon}}^{p} = \dot{\boldsymbol{\varepsilon}}_{sl}^{p} + \dot{\boldsymbol{\varepsilon}}_{tw}^{p}. \tag{4.10}$$

Grain boundary model. The pressure-dependent strength model to describe the inelastic deformation in grain boundaries of AD995 (see Figure 2.7) are used. The parameters are the same as those of pure and dense α-Al_2O_3: λ^0 = 140.70 GPa, μ^0 = 160.03 GPa, B = 5.06, p_0 = -0.8 GPa, β = 32.64°, q_0 = 4.34 GPa and α = 1.5.

In addition, in order to examine the effects of weaker grain boundaries on the effective strength of AD995 under shock compression, the grain boundaries are treated as a glassy second phase with 50% weaker elastic response and 90% weaker in strength. All the material models are implemented into ABAQUS/Explicit code by User Subroutines with VUMAT.

4.3 Porous Polycrystal Model of AD995

In light of the fact that the dynamic compression data available for ceramics are mainly from plane wave experiments, we consider a representative material cell subjected to macroscopically uniaxial-strain, dynamic compression. The resulting stress states are triaxial with transverse symmetry only at the macroscopic level. To simplify the problem, however, we adopt a 2-D approximation, which neglects microstructural variation in one lateral direction. The microstructure model for this study of AD995 is 2-D Voronoi polycrystal model with 3% voids. The model construction includes two parts: polycrystal part and void part. A 2-D 200-grain square-plate microstructure polycrystal model is used as the polycrystal part for AD995. The polycrystal part with finite elements in the study and boundary conditions are shown in Figure 4.2(a). The computational domain is a

square plate with uniform thickness. Uniform and symmetric displacement histories giving rise to the desired dynamic compression loading sequence are applied on the two boundaries normal to the *y*-axis. The four lateral boundaries are prohibited for normal displacements, resulting in zero total strain through the thickness and in the *x* direction macroscopically. The polycrystalline microstructure is constructed by applying the 2-D Voronoi tessellation to the computational domain and assigning to each Voronoi cell a randomly selected crystallographic orientation. To implement the grain boundary modeling, we apply a small in-plane contraction to each Voronoi crystal (see Section 2.2). The resulting intergranular space is filled with the grain boundary material as shown in Figure 4.2(b). The in-plane grain contraction ratio to create the grain boundaries is 1% and the grain boundaries are meshed in one layer. Results of a series of calculations using the models with various thicker grain boundaries up to 10% area ratio and mesh of one or three layers (Figure 2.5) indicate that such variations in grain-boundary structural modeling cause little difference in the computed macroscopic response and microscopic behavior. Also shown in Figure 4.2, the computational domain is overlaid with a specially designed mesh of triangular prism elements, in which the crystals are meshed grain-wise and the neighboring grain core meshes are bridged consistently with the elements in the grain boundary. Such a mesh preserves the polycrystalline microstructure and enables numerical analysis by the FE method.

The applied dynamic compression (compressive pressure) has a rise time of approximately 5μs and obtains the maximum pressure, 20 GPa. The loading history is shown in Figure 4.3.

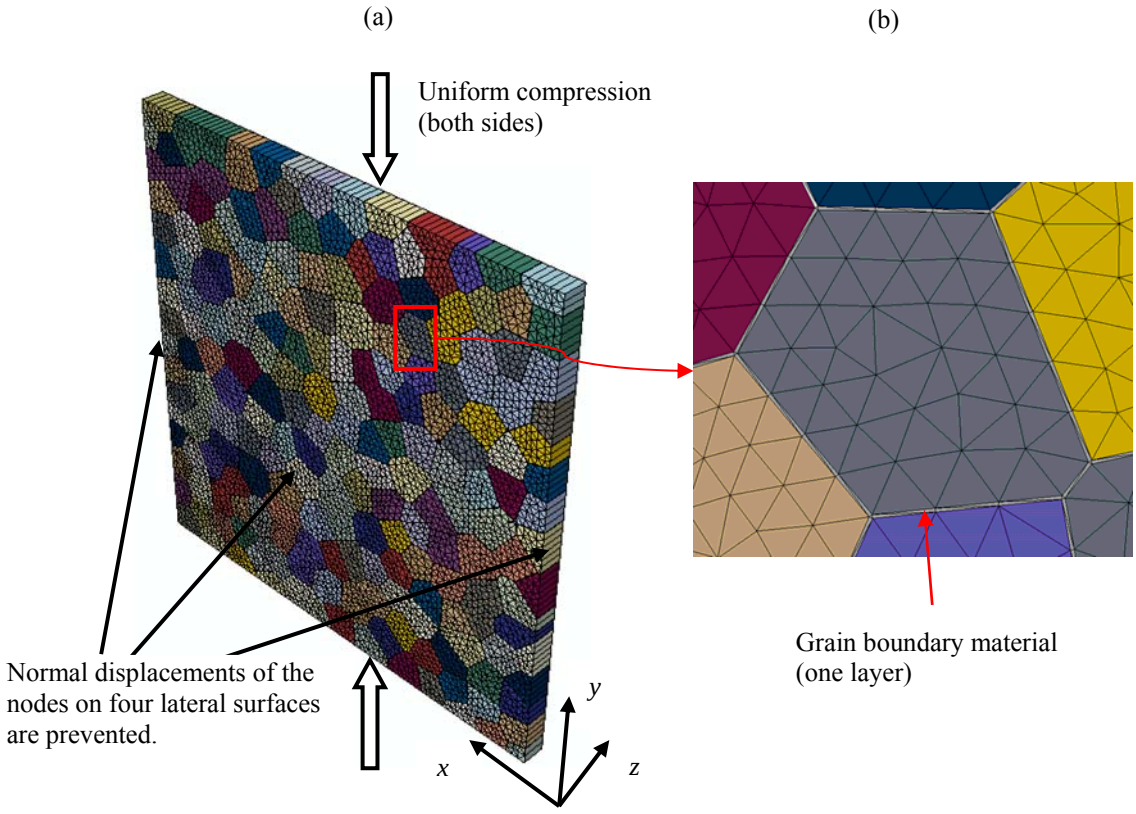

Figure 4.2: Polycrystal model configurations and boundary conditions: (a) polycrystal model with grain boundary layer, microstructure-preserving FE mesh, applied boundary conditions, and (b) grain boundary material.

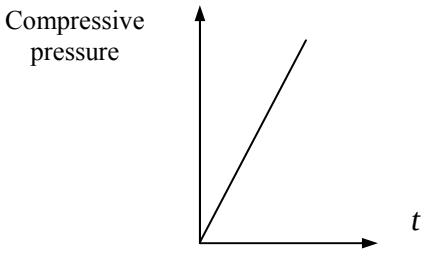

Figure 4.3: The loading history

The next step is to generate the void part on the basis of the polycrystal part. The key objective is to develop an effective void model for the polycrystal simulation of AD995. In order to obtain this objective, three porous polycrystal models with voids of different shapes such as triangular, square and random-shaped voids are developed and void model studies to examine for their performances and mesh dependencies for modeling and analysis of microplasticity-driven void collapsing in AD995 under shock compression are carried out to find the best porous polycrystal model for the simulations. The technical details of constructing voids and the results of void modeling studies are shown as the follows.

4.3.1 The Constructions of Voids

The 200-grain square polycrystal models with triangular, square and random-shaped voids in x-y plane are shown in Figure 4.4. The processes for constructing triangular, square and random-shaped voids are described.

First, a porous polycrystal model with triangular voids is developed because triangular voids are easy and convenient to be generated. Triangular voids are generated by deleting some elements from the polycrystal part. A triangular void is a single element which is randomly selected as a void according the condition (72% in grain, 25% in grain boundaries, and 3% at triple junctions), and the total volume of these selected elements is up to 3% of the total volume of whole polycrystal part. Figure 4.4 (a) shows a sample of the porous polycrystal model with triangular voids and a zoom view. The void modeling study of porous polycrystal model with triangular voids shows that this model is not an

effective model for the simulations (see Section 4.3.2), so other void models need be developed.

Second a porous polycrystal model with square voids is generated by constructing square holes in random locations and orientations of polycrystal part. The square voids are generated first and then the porous model is meshed. Each square void can be viewed as two triangular elements. The volume of each square void is random between 2 times of minimum volume and 2 times of maximum volume of elements. The total volume of all square voids is 3% of the total volume of whole polycrystal model. Figure 4.4 (b) shows a sample of the porous polycrystal model with square voids and a zoom view. The purposes of constructing this model are: First this model can be used to investigate the effect of special voids with a fix shape; Second, it can be also used to study the mesh convergence for constructing random-shaped voids. The details of mesh convergence will be described in Section 4.3.3.

At last a porous polycrystal model with random-shaped voids is generated. The method of constructing random-shaped voids is the same as that of constructing triangular voids, but the difference is that a random-shaped void in grain is deleting two or three triangular elements which connect together from the polycrystal part. The voids are called random-shaped voids because each void has different shape. The total volume of all random- shaped voids is 3% of the total volume of whole polycrystal model Figure 4.4 (c) shows a sample of the porous polycrystal model with random-shaped voids and a zoom view.

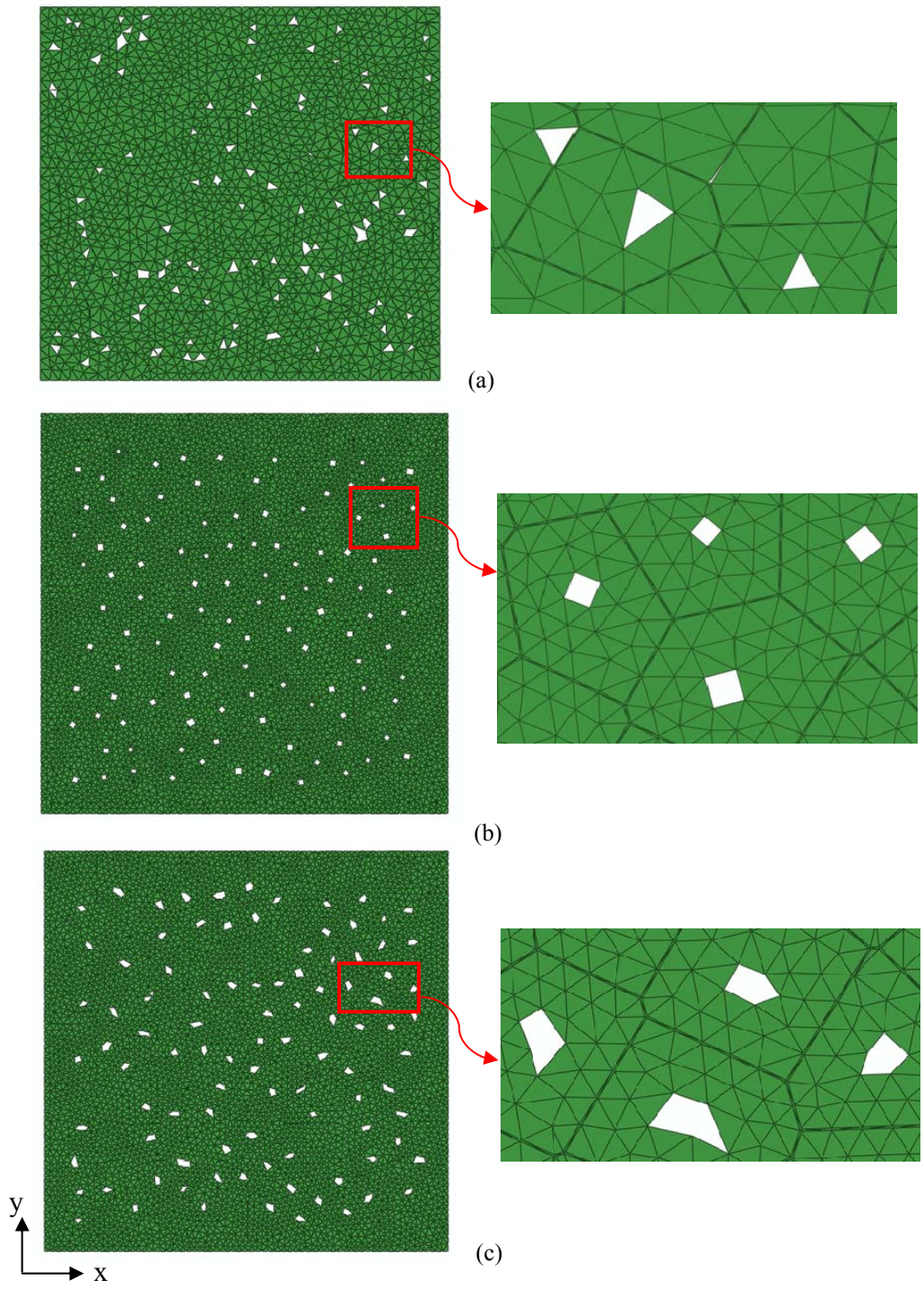

Figure 4.4: 200-grain porous polycrystal models of AD995 with 3% voids of different shapes: (a) Triangular voids; (b) Square voids; and (c) Random-shaped voids.

4.3.2 Void Modeling Studies and Results

Void modeling studies to examine for their performances and mesh dependencies for modeling and analysis of microplasticity-driven void collapsing in AD995 under shock compression are carried out. The results are for three porous polycrystal models of AD995 with 3% voids of different shapes: triangular, square and random-shaped. The material models are described in Section 4.2. Only both prismatic slip and basal slip ($\tau_{cp} = 2.7$ GPa and $\tau_{cb} = 3.3$ GPa) is considered. Boundary conditions and load history are the same as the study of pure and dense Al_2O_3, which are shown in Figure 3.1 and 3.2 respectively.

Macroscopic response. Figure 4.5 compares the three model predictions of the macroscopic longitudinal and mean stress (area–weighted average values) as functions of the applied compressive uniaxial strain with the experimental data of Dandekar & Bartowski (1993) and Reinhart & Chhabildas (2003) and the results of pure and dense Al_2O_3. The following three significant points can be made. First, for three porous polycrystal models with 3% voids, the longitudinal and mean stress response display different behaviors, that means different void models have different influences on the longitudinal and mean stress and an effective void model is important for simulation. Second, compared with the data of pure and dense model, the longitudinal and mean stress response of porous polycrystal models display a different softening behavior with different void shapes, the random-shaped void model is the most soften, the triangular void model is a little soften and the square void model is between random-shaped void model and triangular model. Third, the longitudinal stress calculations based on porous

polycrystal models don't match well with the experimental data and the response displays a stiffening behavior at the HEL and beyond the HEL.

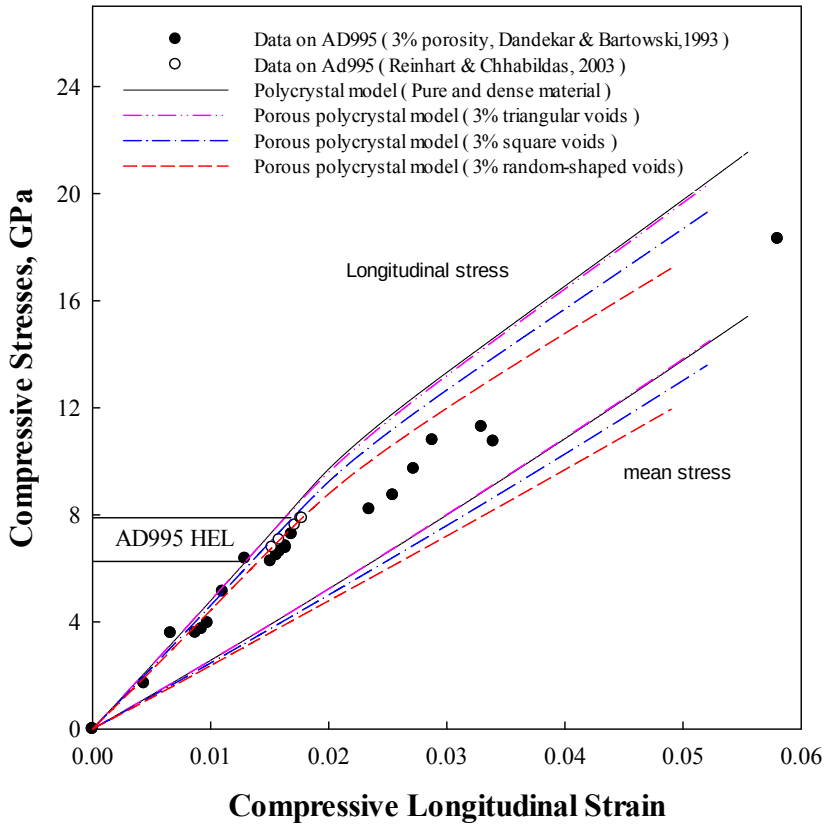

Figure 4.5: Comparison of computed response of three porous polycrystal models of AD995 with 3% voids of different shapes (triangular, square and random-shaped), computed response of pure and dense of Al_2O_3, and measured response of AD995. The numerical results shown are for both prismatic slip and basal slip of $\tau_{cp} = 2.7$ GPa and $\tau_{cb} = 3.3$ GPa.

Effective plastic strain. The effective plastic strain is defined by:

$$\bar{\varepsilon}^{p} = \sqrt{\frac{2}{3}\varepsilon_{ij}^{p}\varepsilon_{ij}^{p}}\ , \tag{3.11}$$

where ε_{ij}^{p} are the plastic strain components, which are uniform in each element. To examine the microscopic behaviors of void models, the comparison of contour plots of effective plastic strain $\bar{\varepsilon}^{p}$ field at σ_y = 16.0 GPa stress state of different models is shown in Figures 4.6. Figures 4.6 (a)-(d) show respectively the effective plastic strain fields of polycrystal models with (a) Pure and density, (b) Triangular voids, (c) Square voids and (d) Random-shaped voids, assuming possible slip in both prismatic and basal systems with $\tau_{cp} = 2.7$ GPa and $\tau_{cb} = 3.3$ GPa. The intensity of effective plastic strains is presented in the same scale. The higher effective plastic strains more than 5% are shown by using red color. It can be observed that the distribution of plastic strain is not continuous in all the figures. From Figure 4.6 (a) to (d), pure and dense model to random-shaped void model, they involve the increase of red areas of higher effective plastic strain, the more increase of effective plastic strain means the much more softening behavior in macroscopic response. For porous polycrystal models, the red areas of higher effective plastic strains are near the voids which are collapsing. Random-shaped void model has more red areas because the random-shaped voids are easily collapsed, and triangular void model has small red areas because most of triangular voids are rigid and hardly collapsed, even the collapsed voids are like random-shaped voids (two or more triangular void connected together). This is why the longitudinal and mean stresses display the same behavior as pure and dense material for the triangular void model.

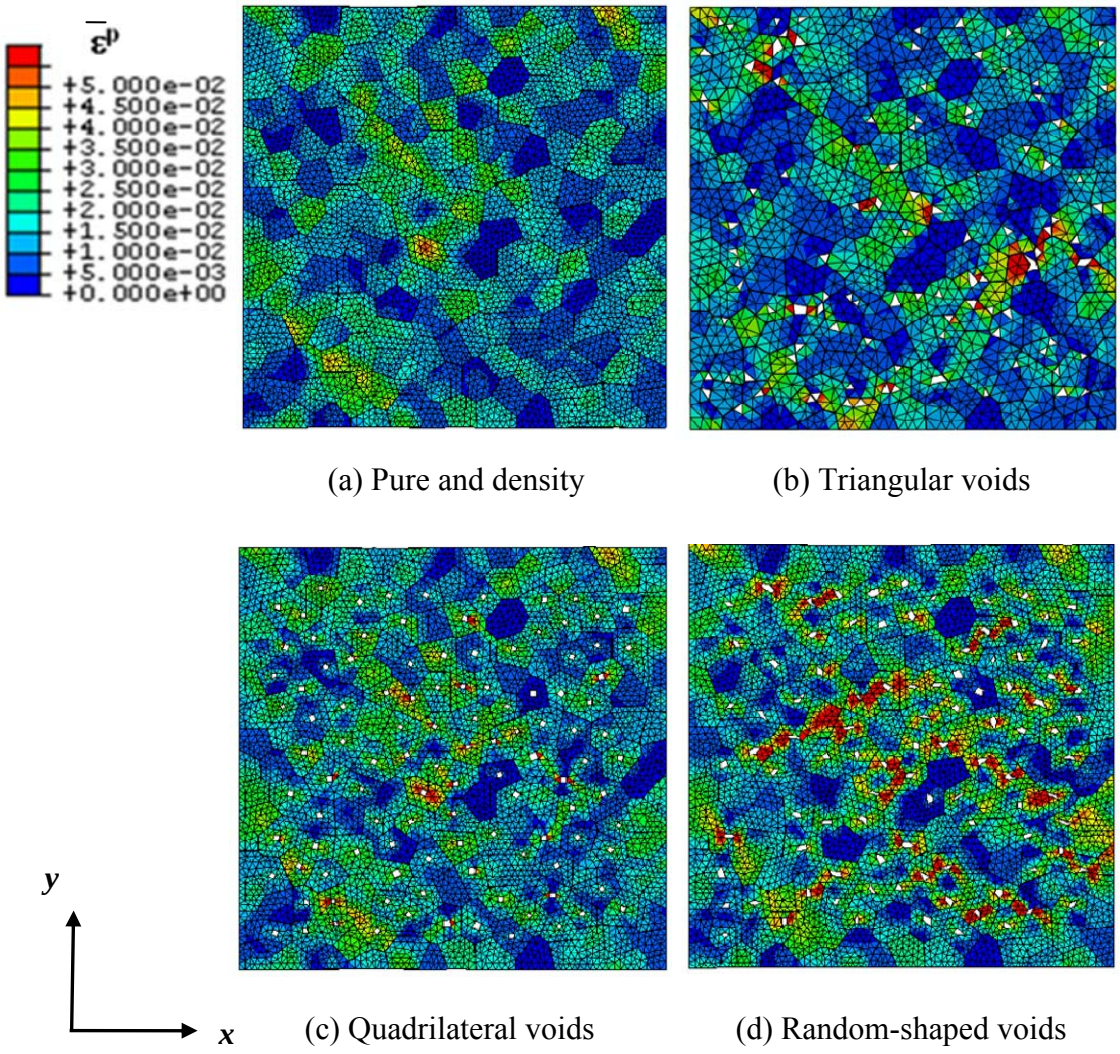

(a) Pure and density (b) Triangular voids

(c) Quadrilateral voids (d) Random-shaped voids

Figure 4.6: Comparison of contour plots of effective plastic strain field at σ_y = 16.0 GPa stress state for void modeling study of different models: (a) Pure and density; (b) Triangular voids; (c) Quadrilateral voids; (d) Random-shaped voids.

4.3.3 Mesh Density and Void Randomness

From void modeling study, it is demonstrated that the random-shaped void model is the best porous polycrystal model for the simulations. Random-shaped voids are used to construct porous VP-FE model for AD995. The other issues are mesh density and void randomness. What is the best mesh density for porous VP-FE model because mesh density can affect the performance of voids? Can a porous VP-FE model generated with a type of random voids represent other types of porous VP-FE models? The studies of mesh density and void randomness are needed to solve the issues.

The study of mesh density and void randomness is described here. Since the random-shaped voids are constructed by deleting two or three elements which connect together from polycrystal part and are generated randomly, the locations of random-shaped voids change with different mesh density. It is hardly to compare the models with different density meshes since the voids are different. For this reason, porous models with the special square shape voids are developed to study the mesh convergence. The details of constructing square voids are presented in Section 4.3.1. Because the square voids are not extracted from the elements, they don't change with different density meshes after they are generated. It is convenient to compare them to study the mesh convergence. The processes are: First, the tests of square void models with different density meshes are carried out and the best reasonable mesh density is obtained by comparing the longitudinal stress response with experimental data. Second, the best reasonable mesh density is suggested for porous VP-FE model with random-shape voids, so the polycrystal part is meshed by using this mesh density and then some different samples of

porous VP-FE models with random-shaped voids generated by different random numbers can be obtained for the study of the void randomness. The detail of constructions of random-shaped voids is presented in Section 4.3.1. And third, we can also construct different samples of porous VP-FE models with different mesh densities for some kind of random-shaped voids to double check the mesh convergence. At last a kind of porous VP-FE model with random-shaped voids, which is the best representation of porous VP-FE models, is obtained for the analysis of strength of Polycrystalline AD995. The results of the studies are present below.

From the tests of different porous VP-FE models with square voids, the result of the best reasonable mesh density is 13209 elements in total. Using this mesh density, several porous polycrystal models with 3% different types of random-shaped voids are obtained for the study voids randomness. Two examples of porous VP-FE models with 3% random-shaped voids with this mesh density, sample1 and sample 2, are used to describe the results of the study voids randomness. The two models with mesh and voids are shown in Figure 4.7 (a) and (b), respectively. The voids of sample 1 and sample 2 are generated in the different locations, so the two samples have different type of voids. The results of strengths response of the two samples are compared to determine void randomness. In addition, the result of strengths response of another sample with more mesh of total 26517 elements is compared with them to check mesh convergence. Figure 4.7 (c) shows the porous VP-FE model with more mesh.

Figure 4.8 shows the results of comparison of model predictions of the macroscopic longitudinal and mean stress as functions of the applied compressive

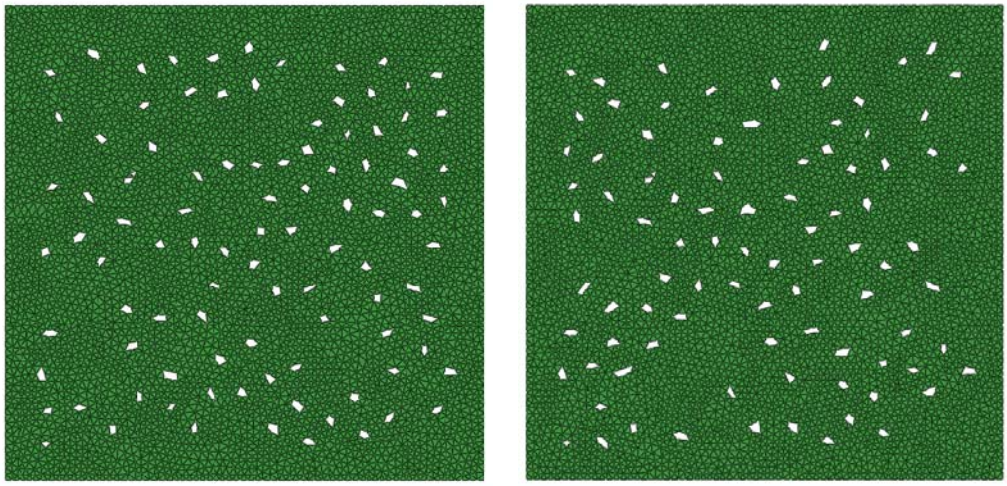

(a) Sample-1 (3% porosity)

(b) Sample-2 (3% porosity)

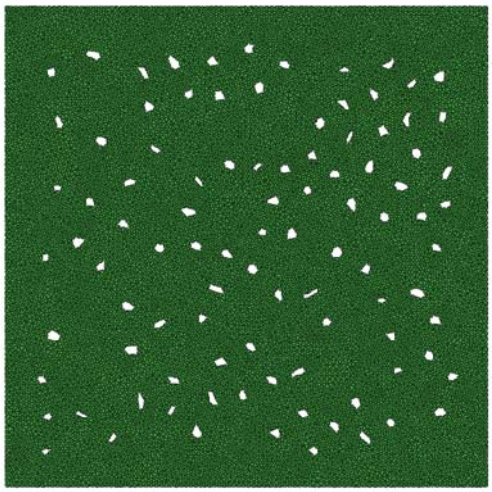

(c) Sample-1 (more mesh)

Figure 4.7: Porous polycrystal models with two different distributions of 3% random-shaped voids, (a) Sample-1, (b) Sample-2, and (c) Sample-1(more mesh).

uniaxial strain. The following two significant points can be made. First, longitudinal stress response for sample 1 (more mesh) displays a little stiffen behavior than that of sample 1 beyond HEL and up to 12GPa. That means even sample 1 has more mesh, but the result is not good. Mesh convergence is also proven. Second, the calculations of longitudinal and mean stresses response for sample 1 and sample 2 are the same. That

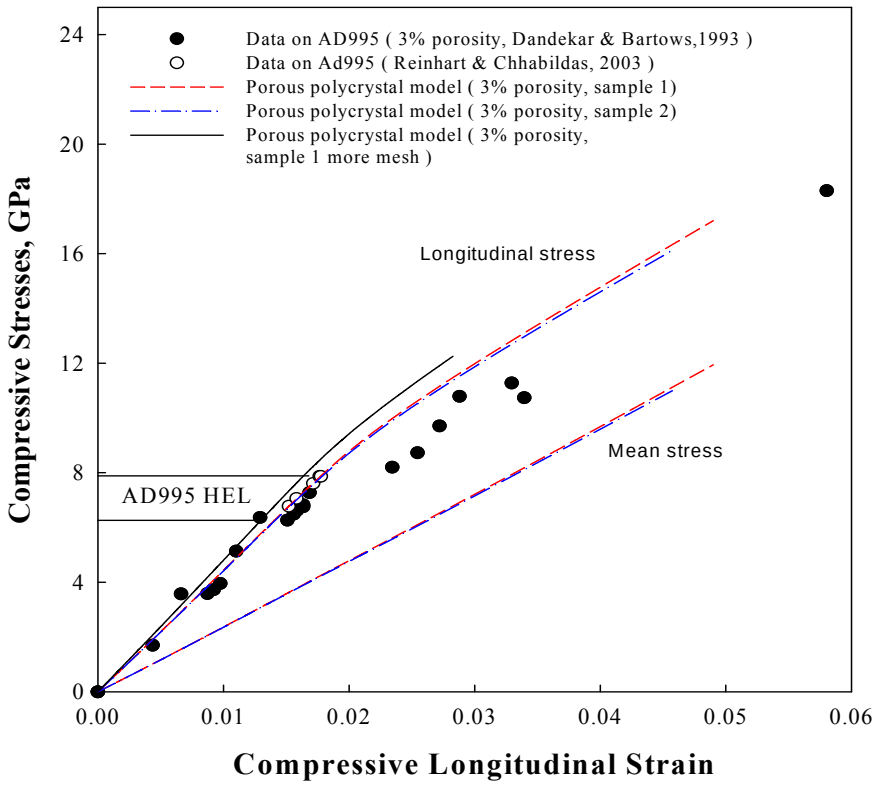

Figure 4.8: Comparison of longitudinal and mean stress response of sample 1, sample 2 and sample 1 (more mesh) for the studies of void randomness and mesh density.

means the two types of voids have the same effects on the strength of AD995. The results of sample 1 can represent those of sample 2. Void randomness is verified. The same results can also be obtained through the examination of the effective plastic strain fields.

Figures 4.9 (a) and (b) show the effective plastic strain fields of sample 1 and sample 2, respectively. The intensity of effect plastic strains is presented in the same scale. The higher effective plastic strains more than 5% are shown by using red color. It can be observed that the plastic strains have the similar distribution in the two figures and also both have the similar reds areas of higher effective plastic strains which are near the collapsing voids. Consequently, the two model samples have the same macroscopic response.

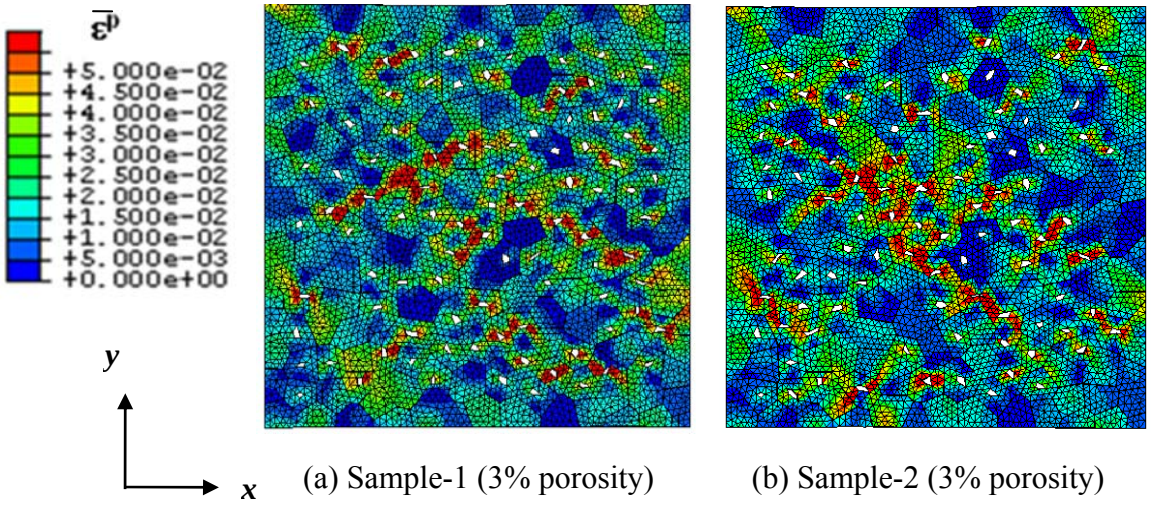

(a) Sample-1 (3% porosity) (b) Sample-2 (3% porosity)

Figure 4.9: Comparison of contour plots of effective plastic strain field at σ_y = 16.0 GPa stress state for porous polycrystal models with two different distributions of 3% random-shaped voids, (a) Sample-1 and (b) Sample-2.

Although the results of mesh density and void randomness are only presented by two samples of porous polycrystal models for consistency, verification calculations with different samples of porous polycrystal models have been carried out to ensure that the results presented are statistically representatives.

4.4 Strength Analysis and Results of Polycrystalline AD995

In order to explain 15-30% reduction in the HEL and more signification reduction in the post-HEL strength of shocked-AD995, the roles of glassy grain boundaries, voids and microplasticity in the inelastic deformations and strengths of polycrystalline AD995 under uniaxial–strain compression are examined. The numerical simulations and results for the strength response of shocked-AD995 are presented in this section.

The roles of glassy grain boundaries are studies based on a 200-grain 2-D porous VP-FE model by treating the grain boundaries as a glassy second phase (weaker boundaries). 3% triangular voids are considered in the model. The reason of using this kind of voids is that we can focus on studying the roles of weaker boundaries because the influence of triangular voids is very small according the previous void modeling studies (see section 4.3.2). The results of the roles of glassy grain boundaries are presented in Section 4.4.1. In order to examine the roles of voids, 2-D 200-grain porous polycrystal models with 1%, 2% and 3% random-shaped voids are developed and the simulations are carried out based on these models. The results of the roles of voids are presented in Section 4.4.2. Microplasticity analysis and results of strength of polycrystalline AD995

are presented in Section 4.4.3. The boundary conditions and load history are described in Figure 4.2 and 4.3 respectively. The porous VP-FE model and the material model are implemented into ABAQUS/Explicit code with User-material Subroutine for FE analysis. The results are presented as the follows.

4.4.1 The Roles of Glassy Grain Boundaries

The purpose of this study is to examine if the weaker boundaries can explain the reduction in the HEL and more signification reduction in the post-HEL strength of shocked AD995. The FE model considers a 2-D 200-grain porous VP-FE model with 3% triangular voids. The technical method is the grain boundaries are treated as a glassy second phase with 50% weaker elastic response and 90% weaker in strength (weaker boundaries). The parameters are λ^0 = 70.35 GPa, μ^0 = 80.015 GPa, B = 4.56, p_0 = -0.8 GPa, β = 32.64°, q_0 = 3.906 GPa and α = 1.5. Crystal material model considers nonlinear elasticity and crystal plasticity with both basal slip and prismatic slip of $\tau_{cb} = 2.7$ GPa and $\tau_{cp} = 3.3$ GPa. The porous VP-FE model and the material model are implemented into ABAQUS/Explicit code with User-material Subroutine for FE analysis.

Model predictions of macroscopic longitudinal and mean stresses (volume-averaged values) as functions of the applied compressive uniaxial strain are plotted in Figure 4.10. The experimental longitudinal data of Dandekar & Bartowski (1993) and Reinhart & Chhabildas (2003) and the computed longitudinal and mean stress response of porous VP-FE model with 3% triangular voids (non-wearker boundaries) are shown in the figure for comparison. The following two significant points can be made. First, the

longitudinal stress calculations cannot match the experimental data of AD995 and the longitudinal stress displays a stiffening behavior at the HEL and high stiffening behavior beyond the HEL. Second, the longitudinal stress response of porous model with 3% triangular voids and weaker boundaries only displays a little softening than that of 3%

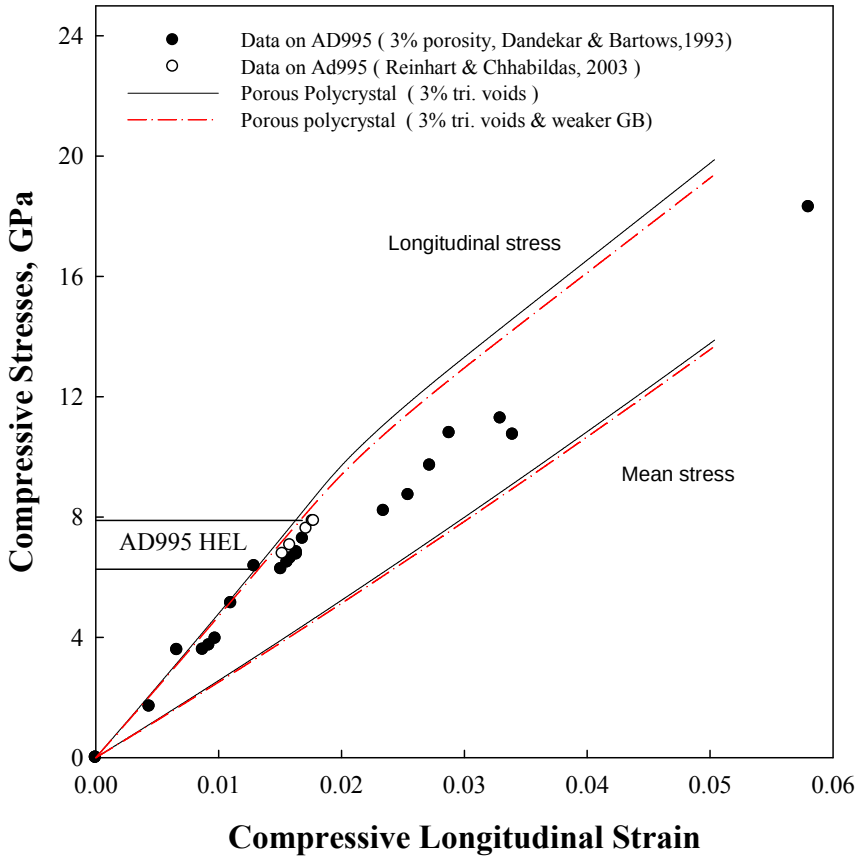

Figure 4.10: Macroscopic longitudinal and mean response of polycrystalline AD995 with 3% triangular voids and weaker grain boundaries.

triangular voids (non-weaker boundaries). It can be observed that the effect of the weaker grain boundaries is small and cannot explain the observed HEL and post-HEL response of shocked-AD995. In other word, it is not the glassy grain boundaries in AD995 alumina responsible for its lower shock strength than the dense one.

4.4.2 The Roles of Voids

To examine the roles of voids, 2-D 200-grain porous VP-FE models with 1%, 2% and 3% random-shaped voids are developed, shown in Figure 4.11 (a), (b) and (c), respectively. The material model considers nonlinear elasticity, crystal plasticity and effective strength model (see Section 4.2). Only both prismatic (primary) slip and basal slip of $\tau_{cp} = 2.7$ GPa and $\tau_{cb} = 3.3$ GPa are considered. The porous VP-FE model and the material model are implemented into ABAQUS/Explicit code with User-material Subroutine for FE analysis. Numerical simulations for longitudinal and mean stresses response of polycrystalline AD995 are carried out for these three porous polycrystal models.

Model predictions of macroscopic longitudinal and mean stresses response are plotted in Figure 4.12. The experimental longitudinal data of Dandekar & Bartowski (1993) and Reinhart & Chhabildas (2003) and the computed longitudinal and mean stress response of pure and dense α-alumina are shown in the figure for comparison. From Figure 4.10, the following three significant points can be made. First, the longitudinal and mean stresses response of three porous models display a softening behavior than those of pure and dense α-alumina. Second, with the increase in the percentage of voids, the much

more softening behaviors are displayed for the longitudinal and mean stresses response. The effect of voids on strength of AD995 is remarkable. Third, the longitudinal stress

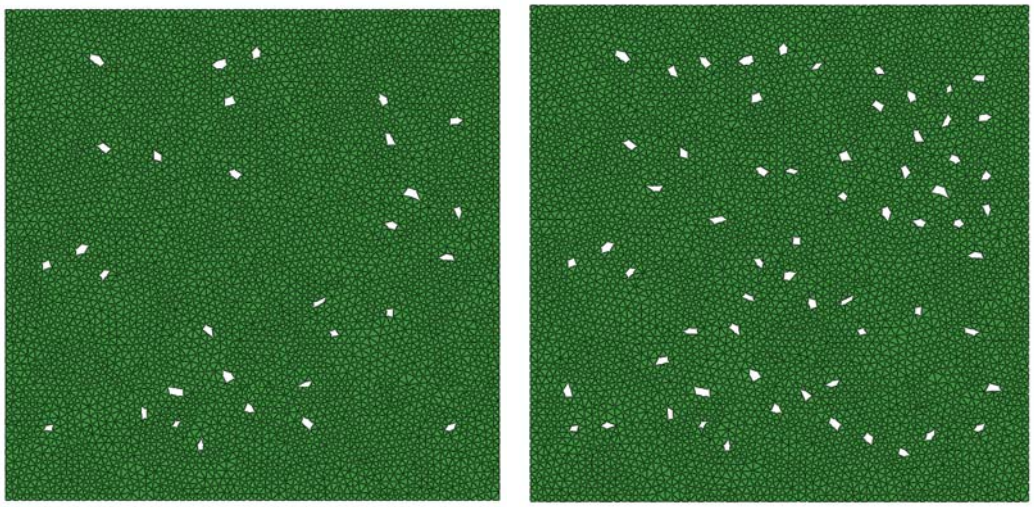

(a) 1% porosity

(b) 2% porosity

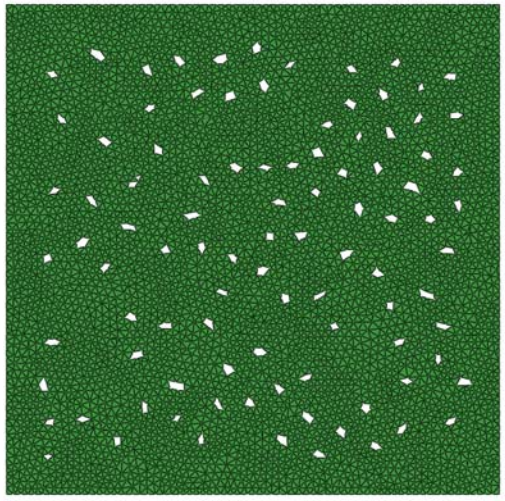

(c) 3% porosity

Figure 4.11: Porous polycrystal models with three different percent porosities of random-shaped voids, (a) 1% porosity, (b) 2% porosity, and (c) 3% porosity.

calculations based on porous polycrystal with 3% porosity compare well with the experimental data up to HEL, but it displays a stiffening behavior on the post-HEL.

To examine the microscopic behavior of shocked AD995 with 1-3% porosities, the contour plots of the effective plastic strain fields for porous ploycrystal model with

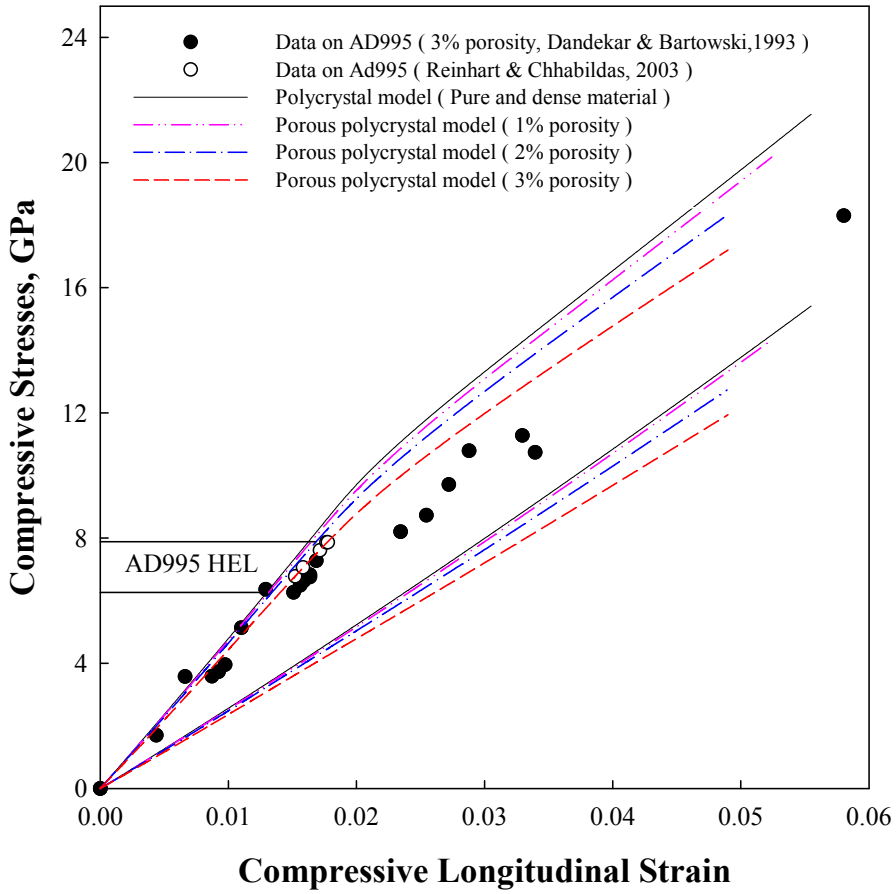

Figure 4.12: Comparison of computed response for polycrystalline AD995 by using porous polycrystal models with random-shaped voids of 1-3% porosities.

1%, 2% and 3% porosity at stress states of σ_y = 16 GPa are shown in Figure 4.13 (a), (b) and (c) respectively. The intensity of effective plastic strains is presented in the same scale. The higher effective plastic strains more than 5% are shown by using red color. From Figure (a) to (c), with the increase in the percentage of voids, the models involve more intensity in effective plastic strain and more red areas of higher effective plastic strains. It means that macroscopic stresses response become much more softening with the increase of effective plastic strain from 1% porosity to 3% porosity. For the entire figures, the distribution of plastic strain is not continuous and the red areas of higher effective plastic strains are near the voids. It can be observed that microplasticity becomes easier to initiate near the voids, evolve in a way of deformation band, and leads to voids collapsing. The more collapsing voids have, the much more softening the macroscopic response displays. It can be concluded that it is the voids, not the glassy grain boundaries in AD995 alumina responsible for its lower shock strength than the dense one. The model predictions can match the experimental data up to HEL but the experimental data right above HEL shows a much more abrupt post-HEL softening than the model prediction. It needs further analysis to explain the significant reduction in the post-HEL strength of shock AD995.

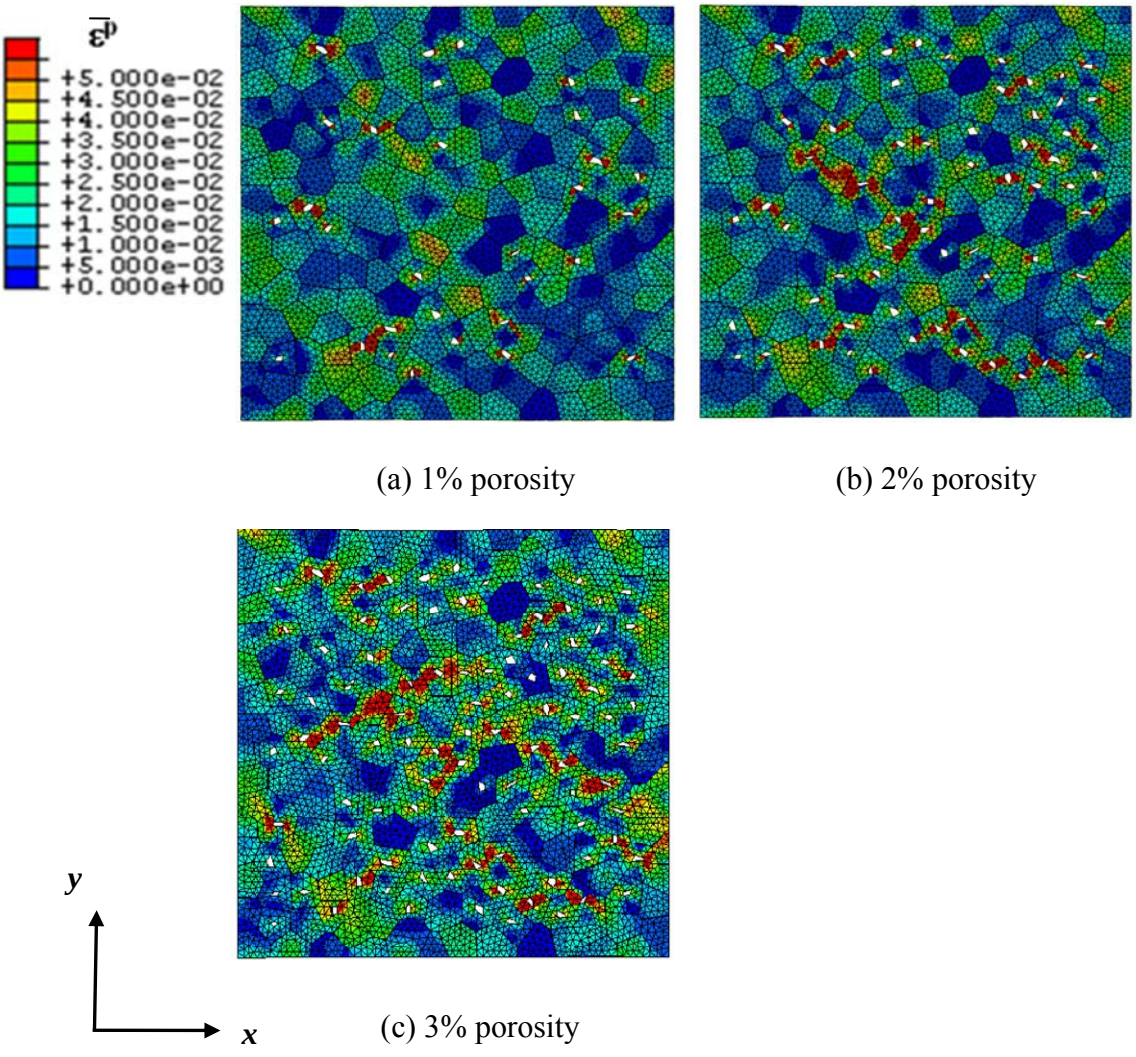

Figure 4.13: Comparison of contour plots of effective plastic strain field at σ_y = 16.0 GPa stress state for porous polycrystal model with of random-shaped voids of different percent porosities: (a) 1% porosity, (b) 2% porosity, and (c) 3% porosity.

4.4.3 Analysis of the Strength of Polycrystalline AD995

The model prediction of longitudinal stress response for porous VP-FE model with 3% random-shaped voids can match the experimental data up to HEL but it displays a much more stiffening behavior than the experimental measurement of post-HEL strength. The purpose of this analysis is to examine the post-HEL strength of shocked AD995 and make the model prediction match well with the experimental data. Since the post-HEL behavior of longitudinal stress response is relative to the deformation systems and all the previous calculations are based on both prismatic (primary) slip ($\tau_{cpb} = 2.7$ GPa) and basal slip ($\tau_{cb} = 3.3$ GPa) conditions, the two studies with different deformation systems and material model parameters are considered for the analysis of the strength of pollycrystalline AD995.

The first study is to activate a deformation twinning system because deformation twinning is another important deformation mode (He et al., 2002) and activating this deformation twinning maybe soften the longitudinal stress response. Hence, a deformation twinning system with the two slip systems are considered for the first study. The deformation twinning is assumed as basal twinning $\{0001\}\langle 10\bar{1}0\rangle$. The relevant system for basal twinning is shown in Figure 4.1. The constitutive equations for modeling and simulation of crystal slip and crystal deformation twinning are described in section 4.2. The CRSS (τ_c) of basal twinning is considered as a lower value and roughly equal to basal slip (τ_{ctw} = 2.7 GPa). The value of τ_{ctw} is used as the CRSS of both basal slip and twinning. The numerical simulation base on the deformation systems combined basal

twinning and prismatic slip with the CRSS of $\tau_{ctw} =$ 2.7 GPa and $\tau_{cp} = 3.3$ GPa is carried out. The porous polycrystal model used is 3% random-shaped voids model. The microstructure model and material model including twinning are implemented into ABAQUS/ Explicit code for FE analysis. Boundaries condition and load history are the same as those of α-Al_2O_3 (see Figure 3.1 and 3.2).

Model predictions of longitudinal stress and mean stress response for the first study are shown in Figure 4.14. It can be observed that the longitudinal stress response based on basal twinning and prismatic slip with the CRSS of $\tau_{ctw} =$ 2.7 GPa and $\tau_{cp} = 3.3$ GPa (the long dash line) displays a much softening behavior than that of both basal and prismatic slip (no twinning) with the CRSS of $\tau_{cb} =$ 2.7 GPa and $\tau_{cp} = 3.3$ GPa (the solid line), but compared with the experimental data (black circle dot), it still displays a stiffening behavior. The result shows that although by activating the deformation twinning, model prediction of longitudinal stress response displays much softening, it still cannot match well with the experimental data. The second study is considered.

In the second study, the different material model parameters for deformation systems of crystal plasticity are considered. Since model prediction cannot compare well with the experimental data even basal twinning system is activated, we have a reason to think that the material parameters for crystal plasticity of AD995 maybe have not the same values as those of pure and dense alumina. The lower CRSS of deformation systems maybe the reasons of abrupt post-HEL softening of strength of shocked AD995.

So the material parameters of lower CRSS values than those of pure and dense alumina are considered in this study.

The deformation systems combined basal twinning and prismatic slip with two conditions of lower CRSS are considered: (1) $\tau_{ctw} =$ 1.8 GPa and $\tau_{cp} = 2.0$ GPa; (2) $\tau_{ctw} =$ 2.0 GPa and $\tau_{cp} = 2.4$ GPa. The numerical simulations based on the two conditions are carried out through ABAQUS/Explicit. The results of calculations are also shown in Figure 4.14 (the dot dash line and the double dot dash line). The following three significant points can be made. First, the calculations predict the same mean stress response, which is consistent with the assumptions of material model. Second, the longitudinal stress calculations based on $\tau_{ctw} =$ 1.8 GPa and $\tau_{cp} = 2.0$ GPa can match well the experimental data in the post-HEL and up to 12.4 GPa, but the calculated value for HEL is lower than that observed. Third, the longitudinal stress calculations base on $\tau_{ctw} =$ 2.0 GPa and $\tau_{cp} = 2.4$ GPa can match well with the experimental at HEL and even in the post- HEL up to 14 GPa.

It can be observed that model predictions by basal twinning and prismatic slip with the low CRSS of $\tau_{ctw} =$ 2.0 GPa and $\tau_{cp} =$ 2.4 GPa compare better with experimental data than those predicted by other parameters of CRSS. It shows that using the same slip system and model parameters as pure and dense alumina may not be sufficient for explaining the inelastic behavior of AD995, especially in the post-HEL, and the influence of basal twinning and prismatic slip with the lower CRSS on shocked AD995 may be significant. In fact, the macroscopic response of shock AD995 is well

captured by model simulation using $\tau_{ctw} =$ 2.0 GPa and $\tau_{cp} =$2.4 GPa up to longitudinal of 14 GPa or about 2 times the HEL.

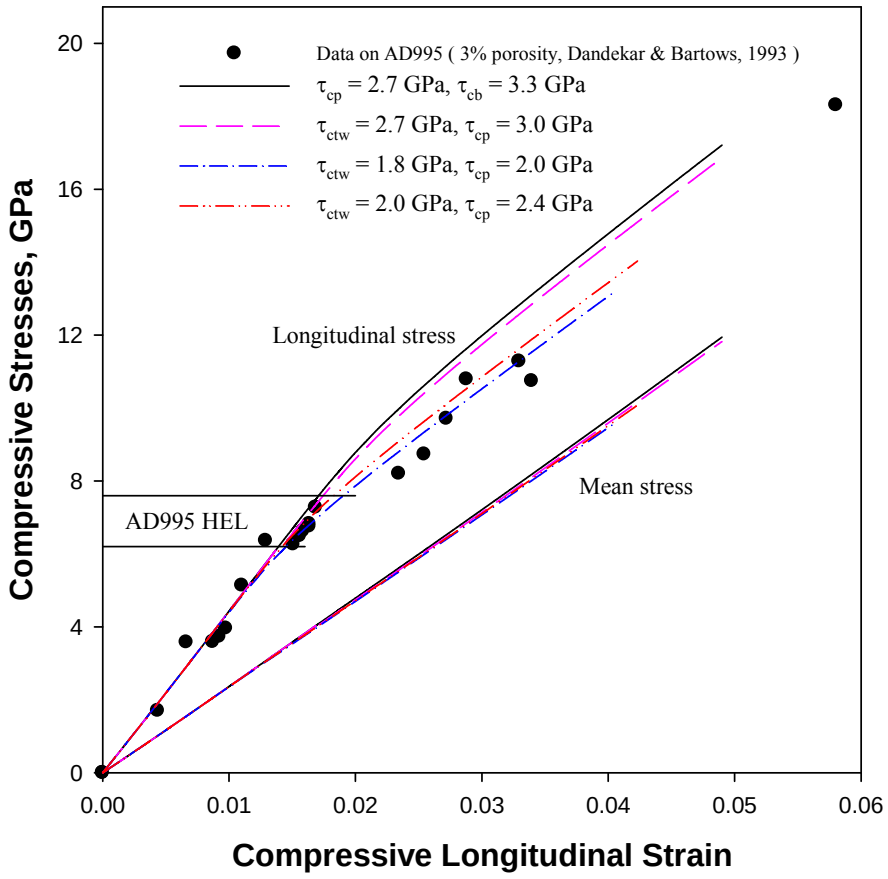

Figure 4.14: Macroscopic longitudinal and mean stresses response of polycrystalline AD995.

To examine the microscopic behavior of shocked AD995, the contour plots of effective plastic strain $\bar{\varepsilon}^p$ fields at three stress states: (a) $\sigma_y = 7.62GPa$, (b) $\sigma_y = 12.06GPa$, and (c) $\sigma_y = 14.03GPa$ are shown in Figure 4.15. The deformation systems are allowed to occur in basal twinning and prismatic slip systems with the CRSS of $\tau_{ctw} =$ 2.0 GPa and $\tau_{cp} = 2.4$ GPa. The same intensity scale is used for different stress states. The fields of effect plastic strains higher than 5% are described in red areas. The calculated HEL is about 7.1GPa. At little above HEL $\sigma_y = 7.62GPa$ (a), there exists a small amount of slipped crystals, but the intensity of plastic strain is still small. Voids collapsing are initiated. At $\sigma_y = 12.06GPa$ (b), more crystals are deformed with increased intensity of plastic strain. The evolution of microplasticity from (a) to (b) is rapid since the activated deformation systems. There involves some more red areas of high plastic strain near the voids and void collapsing evolves in the way of deformation twinning band. The more increase of effective plastic strain can explain the much softening behavior in longitudinal response. A significant increase in the intensity of effective plastic strain can be observed in (c) at $\sigma_y = 14.03GPa$. Many more red areas of high plastic strain are involves near the voids and lead to void collapsing. Some voids are totally collapsed and the calculation is failed to continue. The longitudinal stress of the simulation is up to 14.03 GPa, about 2 times of HEL.

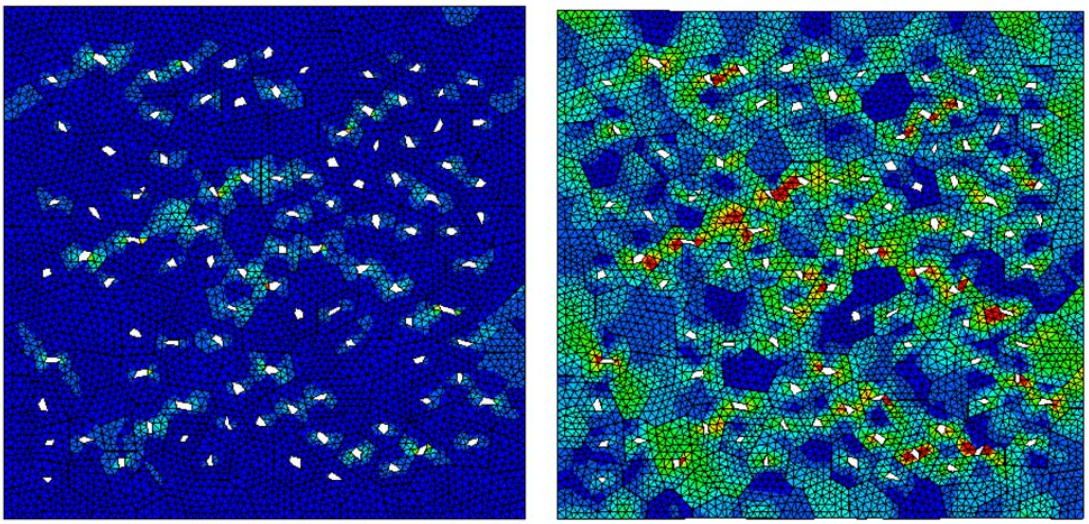

(a) σ_y = 7.62 GPa

(b) σ_y = 12.06 GPa

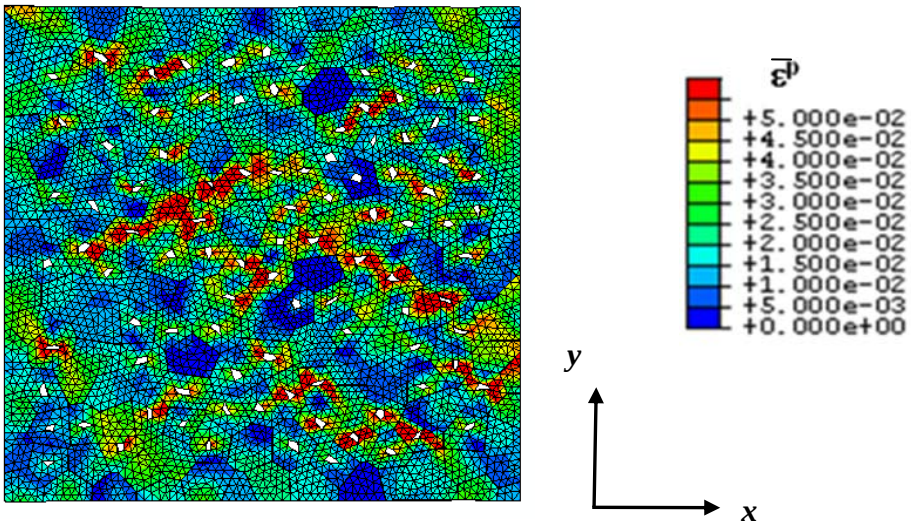

(c) σ_y = 14.03 GPa

Figure 4.15: Contour plots of effective plastic strain field in polycrystalline AD995 at three different stress states: (a) σ_y = 7.62 GPa, (b) σ_y = 12.06 GPa, and (c) σ_y = 14.03 GPa, assuming possible deformations in both basal twinning and prismatic slip systems with $\tau_{ctw} = 2.0$ GPa and $\tau_{cp} = 2.4$ GPa.

4.5 Summary

In this chapter, micromechanical analysis has been used to investigate the strength of polycrystalline AD995 alumina under dynamic loading and understand the difference between the inelastic deformation of shocked AD995 and that of shocked pure and dense α-phase alumina. Three types of 2-D porous VP-FE models have been constructed and examined for their performance and mesh dependencies for modeling and analysis of microplasticity-driven void collapsing in polycrystalline AD995 under shock compression. The material model of AD995 considers nonlinear anisotropic crystal elasticity and rate-dependent crystal plasticity. Microplasticity is assumed to originate from combined basal and prismatic slip, and even deformation basal twinning. The microstructure and material models have been implemented into ABAQUS/Explicit for finite element analysis. First, the grain boundaries are treated as a glassy second phase to examine the effects of weaker grain boundaries. Next, AD995 is approximated as pure alumina with 1%, 2% and 3% porosities to investigate the roles of voids in the inelastic deformation of AD995 under uniaxial-strain. Neither of the two studies can explain the observed HEL and post-HEL response of shocked AD995. At last, microplasticity analyses consider deformation twinning and crystal slip with lower CRSS of deformation systems are carried out to explain the observed the observed HEL and post-HEL response of shocked AD995.

Numerical results of void modeling studies for polycrystalline AD995 based on both basal and prismatic slip indicate the followings. First, triangular voids are so rigid to be collapsed and may be inadequate for intense plastic deformation near voids. The

longitudinal stress response of porous polycrystal model with 3% triangular voids displays almost the same behavior as that of pure and dense alumina. Second random-shaped voids are found to be the most advantageous, providing relative ease in construction, more realistic void shape modeling, and good ability for capturing void collapsing process. The longitudinal stress response of porous polycrystal model with 3% random-shaped voids displays the much more softening behavior than that of pure and dense alumina. Third, using porous polycrystal model with 3% square voids is convenient to have a test of mesh density. At last, void randomness is tested by using different porous polycrystal models of random-shaped voids to ensure that the results are statistically representative. Porous VP-FE model with random-shaped voids is used for the analysis of strength of AD995.

Numerical results for the analysis of strength of polycrystalline AD995 under dynamic loading indicate the followings: (1) Weaker grain boundary cannot explain the observed HEL and post HEL response of shocked AD995. (2) It is the voids in AD995 that responsible for its lower shock strength than the dense one. Microplasticity becomes easier to initiate near the voids, evolves with the deformation band, and leads to void collapsing. Model prediction based on both basal slip and prismatic slip with τ_{cp} = 2.7 GPa and $\tau_{cb} = 3.3$ GPa cannot match the experimental data. (3) Model prediction based both deformation twinning and prismatic slip with high threshod τ_{ctw} = 2.7 GPa and $\tau_{cp} = 3.3$ GPa can match the experimental data up to HEL, but cannot match the experimental data in the post-HEL. (4) In fact, model prediction can match well with the experimental data if a lower threshold of CRSS for deformation systems in crystal

plasticity than that of pure and dense alumina is used. The macroscopic response of shock AD995 is well captured by model prediction based on both deformation twinning and prismatic slip with low threshold τ_{ctw} = 2.0 GPa and τ_{cp} = 2.4 GPa up to longitudinal stress of 14 GPa or about 2 times of HEL. (5) The evolution of effective plasticity strain based on both deformation twinning and crystal slip with lower threshold is rapid for both intensity and plasticity field when the material is shocked to ~12 GPa, which can explain the abrupt post-HEL of strength of AD995. (6) When the shock stress is up to 14 GPa, most of the crystals have been plastically deformed and some voids are collapsed totally.

CHAPTER 5

RESPONSE OF POLYCRYSTALLINE ALUMINUM OXYNITRIDE UNDER SHOCK COMPRESSION

5.1 Introduction

Polycrystalline aluminum oxynitride (AlON) is a very important material for advanced structural engineering purposes. In particular, it can be sintered into a nearly fully dense isotropic and transparent polycrystalline solid which has the potential of serving as a low-cost, but high-strength, window material. In this regard, AlON has a distinct advantage in relation to polycrystalline Al_2O_3, which cannot be produced with true optical transparency (Graham and Munly, 1988). The crystals of AlON have cubic spinel structure and a typical size of 200 microns. The synthesis, fabrication, and microstructure of polycrystalline AlON have been described in detail by McCauley and Corbin (McCauley and Corbin, 1982). Although there are several studies to measure the Hugoniot Elastic Limit (HEL) of shocked AlON (Cazamias and Fiske, 2001; McCauley, 2002; Thornhill et al., 2005), the results regarding its shock strengths and mean stress

response are conflicting. The compressive strengths of shocked AlON under dynamic loading are not yet clear.

In view of the interest in AlON spinel as a transparent structural engineering material, it is necessary to have a good understanding of the strength of the material under shock compression and determine its strength properties. For the purposes, macroscopic effective shock strength modeling and simulations to interpret the available plate impact experiments on AlON and 3-D mesoscopic VP-FE modeling and analyses to predict the crystal elasticity and plasticity of shocked AlON are carried out.

Effective shock strength modeling and wave profile simulations of a series of plate impact experiments on AlON are presented in Section 5.2, including material model descriptions, FE models and simulations, and the analysis of results. The material modeling considers a pressure–dependent effective shock strength model that combines the Drucker-Prager plasticity with a limited strength cap and a nonlinear elasticity model assuming compression-dependent bulk modulus as detailed in Section 5.2.1. FE models and simulations are presented in Section 5.2.2, including the description of experiments that are simulated, the configurations of FE models and the simulations. The details of results are discussed in Section 5.2.3, including the comparisons of wave profiles between simulation results and experimental measurements, the optimized material model parameters, the determination of the effective shock strength of AlON, as well as the relationship between the longitudinal stress and particle velocity.

Mesoscopic analyses using a 600-grain cubic VP-FE model that allows explicit modeling of anisotropic crystal elasticity and plasticity and grain-to-grain interactions are

presented in Section 5.3. The method for modeling and simulations is described in Section 5.3.1, including the details for the 600-grain cubic VP-FE model, material descriptions, and numerical simulations. The analysis to determine the ambient elastic constants C_{ij} of AlON crystals in the polycrystalline form is presented in Section 5.3.2. Microplasticity analysis to determine the compressive crystal strength of shocked AlON is presented in Section 5.3.3. Section 5.4 summarizes the key findings of the studies presented in this chapter.

5.2 Simulations to Interpret Plate Impact Experiments on AlON

To determine the effective strength of shock-compressed AlON, a series of wave profile simulations of the plate impact experiments on AlON (Thornhill et al., 2005) are carried out by using a pressure–dependent strength model that combines the Drucker-Prager plasticity with a limited strength cap. Compared with the wave profiles between the simulations and the experiments, the effective compressive strength and mean stress response of shocked AlON are obtained. Details of the material modeling, FE model for wave profile simulations, and results are presented below.

5.2.1 Material Model

Effective shock strength model. It is found that the effective shock strength of several polycrystalline ceramics can be well summarized by a pressure-dependent "plasticity" law as depicted in Figure 5.1. Equivalence between pressure p and compressive mean stress $-\sigma_{ii}/3$ (where σ_{ij} are the components of the Cauchy stress) is

assumed. The flow stress is measured in terms of the second invariant of deviatoric stress J_2 $(= S_{ij}S_{ij}/2)$ with $S_{ij} = \sigma_{ij} + p\delta_{ij}$. The flow stress is assumed to vary with pressure similar to the flow-surface treatment of the Johnson-Holmquist (JH-2) model (Johnson and Holmquist, 1994). The flow surface has a pressure-dependent portion that follows the Drucker-Prager plasticity (F_s), a limit strength portion that is pressure-independent (F_c),

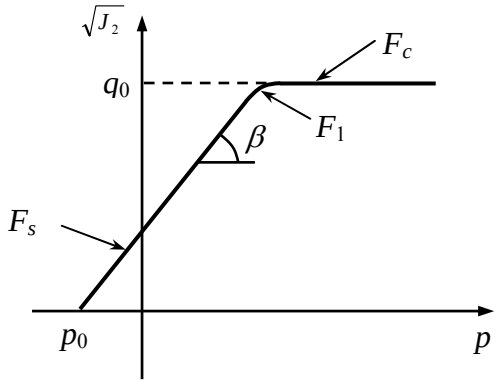

Figure 5.1: Schematic of shock strength model.

and a transition connecting these two portions smoothly (F_1), which are defined by Eqs. 2.34(a) ~ 2.35 (b) (see Section 2.3.3). The constitutive equation of the Drucker-Prager model can be solved with arbitrary degree of non-associativity (Loret and Prevost, 1986) using Eqs. 2.36 ~ 2.40 (see Section 2.3.3). The following parameters of the effective shock strength model need to be determined and optimized from the simulations: q_0 the limiting strength, p_0 the cohesion of intact material, β the friction angle of flow surface F_s, and αq_0 the radius of transition curve F_1.

Nonlinear elasticity model. Typically, the compression dependence bulk modulus can be described as

$$K = \lambda_0[1 + B(1 - V/V_0)] + 2\mu_0/3 \tag{5.1}$$

Where V_0 and V are respectively the initial and current specific volumes, $(1 - V/V_0)$ volume compression, λ_0 the initial Lamé constant, μ_0 the initial shear modulus, and B the nonlinearity correction parameter. The values of initial density ρ_0, λ_0 and μ_0 are chosen as: $\rho_0 = 3670 kg/m^3$, $\lambda_0 = 126.33 GPa$, $\mu_0 = 126.5 GPa$ (McCauley, 2002). The parameter B needs to be determined from the simulations.

5.2.2 Finite Element Model and Simulations

In recent years, plate impact experiments were performed by several investigators. For example, Thornhill and vogler have published a set of wave profiles of plate impact experiments on AlON with a VISAR window used Lithium fluoride (Thornhill, et al., 2005). These experiments provided numerical simulations original data and verification for the results of simulations. The simulations are based on these experiments conducted by T. F. Thornhill.

Description of experiments that simulated. The experimental configurations are schematically shown in Figure 5.2 (a). There were two kinds of configurations. One was a flier of copper (Cu) impacting the sample of AlON with a Lithium fluoride (LiF) window bonded to its back surface. AlON diameters were 23 or 29 mm while Cu flier was 27 mm in diameter. Another was a flier of coaxial flier aluminum (Al) surrounding

copper impacting the sample of AlON with a LiF window bonded to its back surface. AlON diameter was 50 mm while the inner Cu flier diameter was 17 mm and the Al outside diameter was 64 mm. LiF window was boned on the AlON for interface velocity measurements resulting from Al and Cu impactors. The interface velocity measurements (Exp. # 8, 7, 2, 1 and 6 in reference) are shown in Figure 5.2 (b).

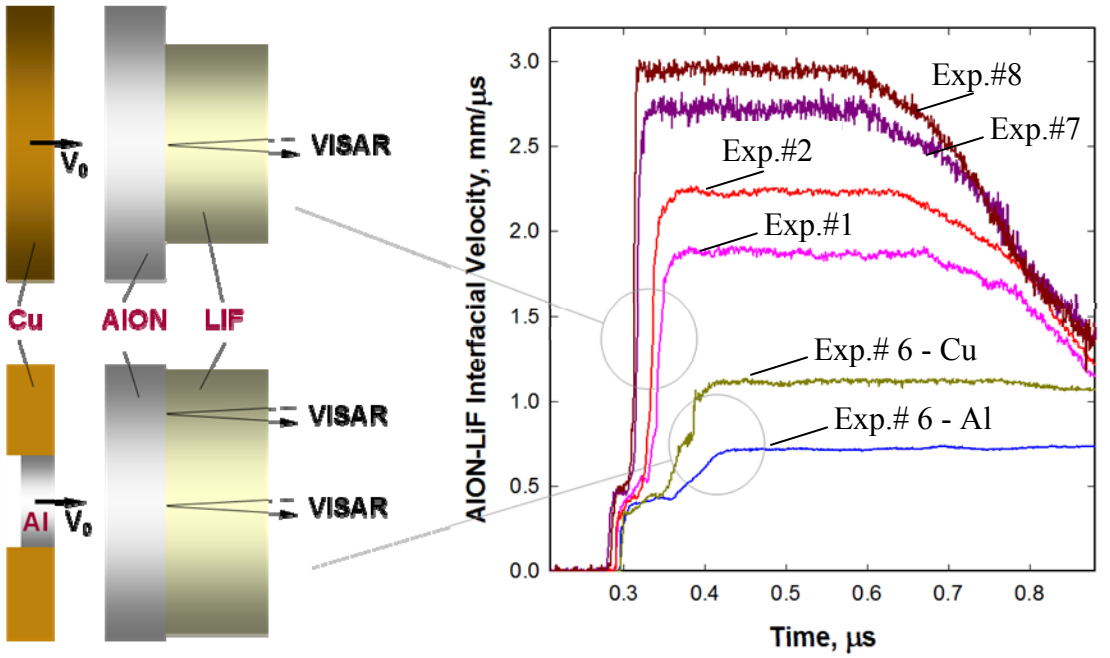

(a) The configurations of impact experiments

(b) Interface particle velocity measurements of impact experiments

Figure 5.2: The configurations and Interface particle velocity measurements of impact experiments.

Impact summary and some results including the shock stress σ, the particle velocity u_p and the shock velocity U_s for the experiments are listed in Table 5.1. They

were calculated by using jump condition analysis method in the reference (Thornhill et al.,, 2005). The strains ε are calculated by the measurement data of the initial density ρ_0 and the density of hugoniot state ρ by using the equation of $\varepsilon = \ln(\rho/\rho_0)$.

Table 5.1: Impact summary and some results for AlON experiments by Thornhill et al..

Exp. #	Impact velocity km/s	Flier thick mm	AlON Thick mm	AlON σ_{HEL} GPa	AlON Hugoniot			
					u_p km/s	U_s km/s	ε	σ GPa
1	2.612	Cu 1.477	3.005	9.83	1.550	8.970	0.189	51.0
2	3.124	Cu 1.474	3.010	8.72	1.880	9.110	0.232	62.9
3	1.561	Al 3.009	3.010	10.59	0.541	8.080	0.071	16.0
3	1.561	Cu 1.855	3.010	9.17	0.896	8.290	0.110	27.2
6	1.577	Al 3.259	3.012	10.50	0.549	7.950	0.073	16.1
6	1.577	Cu 3.057	3.012	10.50	0.897	8.420	0.112	27.8
7	3.846	Cu 1.509	2.982	10.73	2.350	9.390	0.289	80.9
8	4.124	Cu 1.526	2.990	10.29	2.530	9.610	0.305	88.9

The configurations of finite element models. To simulate these experiments, the configurations of experiments are modeled using planar axisymmetric FE models, as shown in Figure 5.3. Figure 5.3 (a) shows the type of model for simulating the experiments of No. 1, 2, 7 and 8. The model includes the Copper impactor, the AlON

sample and the LiF windows buffer. The thicknesses of Copper impactor and AlON sample are the same as the experiments (see Table 5.1). To prevent the wave coming back, the thickness of LiF needs be enough thick, modeled as 15mm. Figure 5.3 (b)

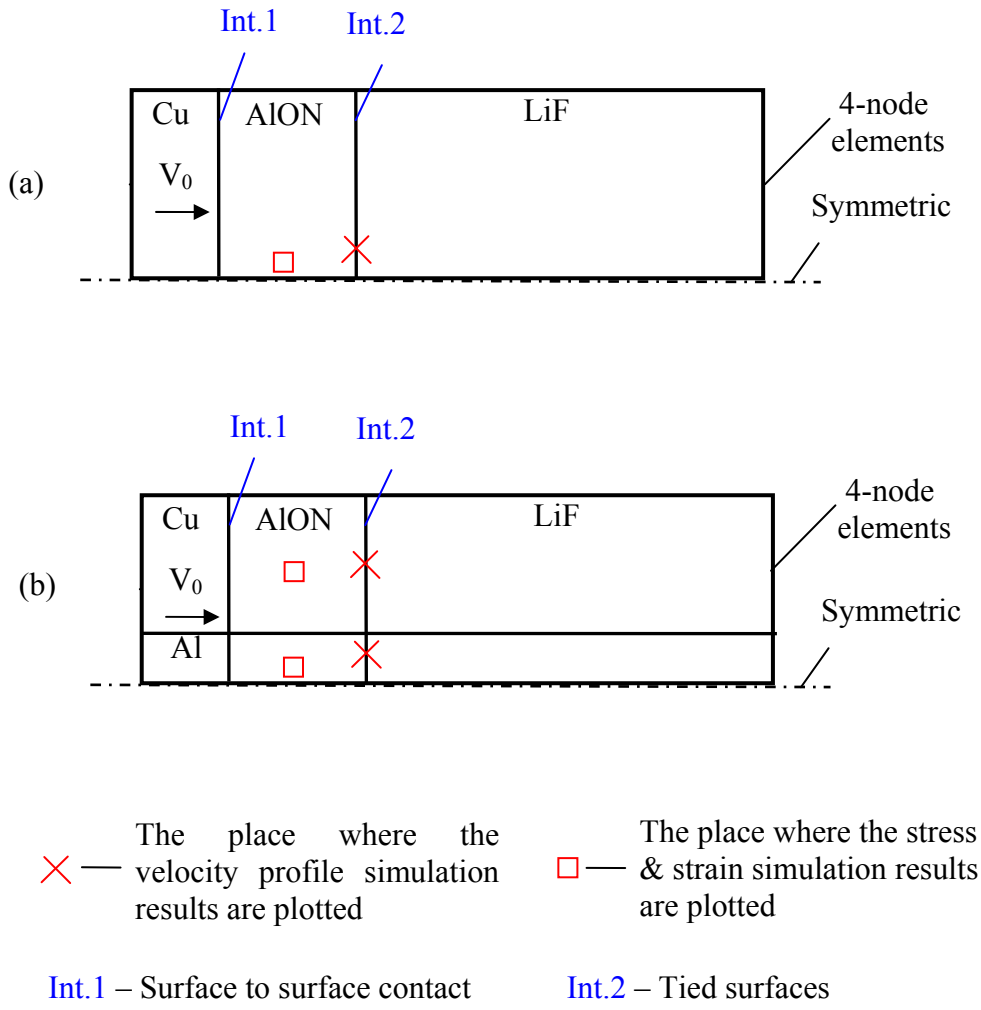

Figure 5.3: The configurations of finite element models: (a) for experiments # 1, 2, 7, and 8; (b) for experiments # 3 and 6. The models are meshed by 4-node axisymmetric elements.

shows the type of model for simulating the experiments of No. 3 and 6. The model includes the Cu and Al impactor, the AlON sample and the LiF windows buffer. To model the Cu and Al impactor, the whole impactor is divided into two parts. The inner is Al and the outer is Cu. The AlON sample and LiF windows are also divided into two parts according the impactor. The thicknesses of Cu impactor, Al impactor and AlON sample are the same as the experiments (see Table 5.1). The thickness of LiF is also modeled as 15mm.

The models are implemented into ABAQUS/Explicit and meshed by 4-node axisymmetric solid elements, which are not shown in Figure 5.3 because the element size (about 0.025mm) is so tiny. Figure 5.3 also shows the boundary conditions used for the 2-D plate impact simulations: (1) the center of the model is confined as symmetric; (2) the intersection between the impactor and the AlON sample is modeled as surface to surface contact (explicit); (3) the surfaces of the intersection between the AlON sample and the LiF window are tied together; (4) the initial velocity of the impactor is $V_{0,}$ which values are equal as the experiments (see Table 5.1).

Plate impact simulations. Material models of AlON, Copper, Al and LiF are implemented into ABAQUS/Explicit code with User-material Subroutine (VUMAT) for FE analysis. The material models of Copper, Al and LiF are employed as the hydrodynamic models (Feng and Gupta, 1994 & 1996), which are implemented into ABAQUS material model– equation of state by the following parameters, shown in Table 5.2.

The simulations are performed to match the wave profiles of AlON-LiF interfacial velocity vs. time with the experimental data by adjusting the parameters of material strength model of AlON, and at the same time the compressive longitudinal and mean stress response of shocked AlON are obtained. The places where the simulation results of velocity profiles, stresses and strains are plotted are also shown in Figure 5.3.

Table 5.2: The parameters of material model for Cu, Al and LiF

Material	ρ_0 (kg/m^3)	c_0 (m/s)	s	Γ_0	G (GPa)	Y_0 (MPa)
Cu	8930	3944.7	1.423	1.99	48.0	20.0
Al	2703	5188.3	1.382	2.0	27.63	324.0
LiF	2640	5148.0	1.353	1.63		

where ρ_0 is the initial density, c_0 and s define the linear relationship between the linear shock velocity U_s and the particle velocity u_p as $U_s = c_0 + su_p$, Γ_0 is the constant for the Grüneisen parameter , G is the shear modulus G and Y_0 is the yield strength.

5.2.3 Result and Discussions

The results presented in the section are for the plate impact experimental simulations on ALON, including the results of wave profiles, the material strength model, the compressive longitudinal and mean stress response and the relationship between longitudinal stress and particle velocity. The details of the results are described as the followings.

Results of wave profiles. The simulation results of AlON-LiF interfacial velocity profiles computed by using the pressure-dependent material strength model are shown in Figure 5.4. The processes of simulations are: firstly, based on the experiment #2, the

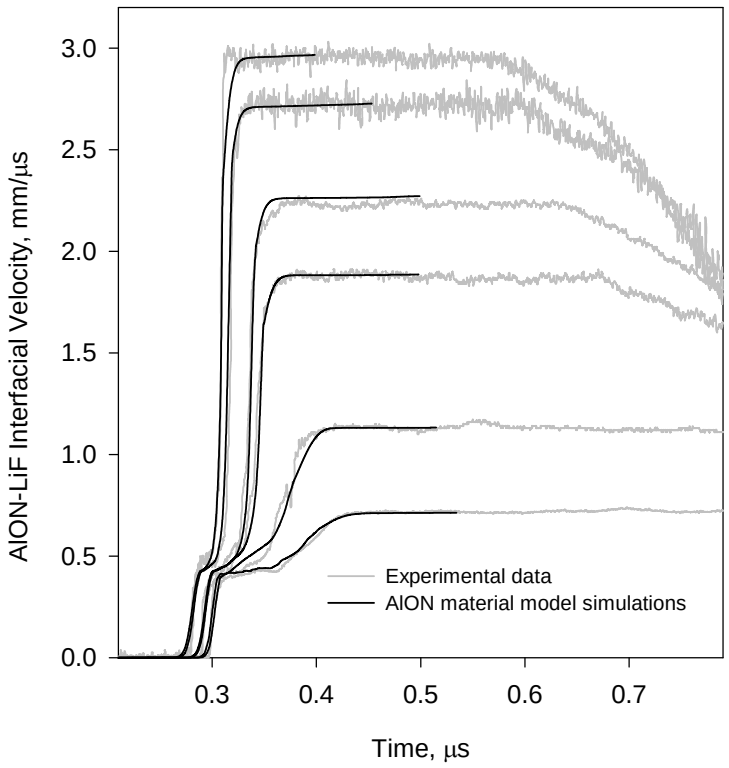

Figure 5.4: Comparison of the simulation results and experimental data of the AlON-LiF interfacial velocities.

simulation wave profile is computed to match well with the experimental measurement of experiment #2 by adjusting the parameters of material model, and a group of material parameters is obtained; secondly using this group of material parameters and the same conditions of the simulation of experiment #2, the simulations for other experiments (Exp.

1, 6, 7 and 8) are carried out to obtain the wave profiles and these wave profiles are compared with the experimental measurements; next, to get optimize the material parameters by repeating the first two steps until the match between the simulation results and experimental measurements is satisfied. In Figure 5.4, the simulation results compare very well with the experimental measurements by the optimized parameters for the strength model: $p_0 = -0.35GPa, \beta = 32.14^\circ, q_0 = 5.06GPa, \alpha = 1.8$, and $\lambda_0 = 126.33GPa$, $\mu_0 = 126.5GPa$, $B = 4.25$.

AlON strength model. This optimized strength model is plotted in Figure 5.5 in comparison with the experimental data of kolsky bar measurement (Paliwal et al., 2008)

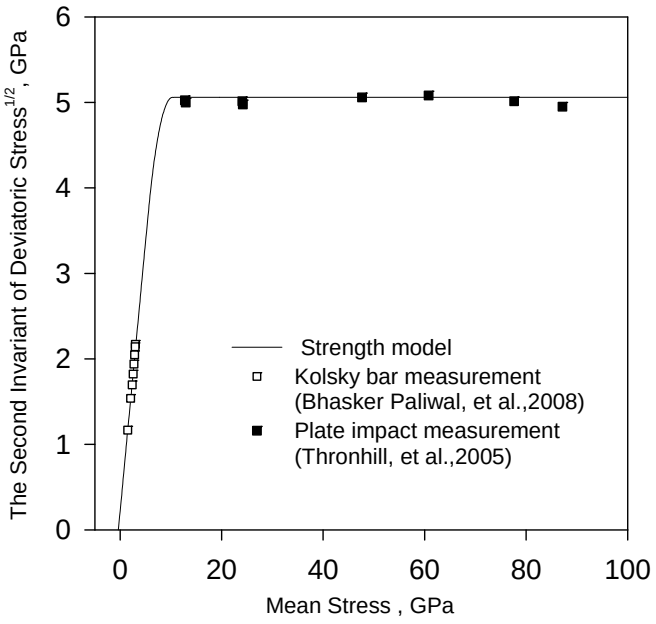

Figure5.5: The plot of the strength model of ALON, compared with the experimental data of kolsky bar measurement and plate impact measurement.

and plate impact measurement (Thornhill et al., 2005). From the figure, the curve compares well with the experimental data.

Some results for the simulations are listed in Table 5.3. The simulation results of the shock velocity U_s and the particle velocity u_p compare well with the experimental data in Table 5.1, but the longitudinal stresses are higher than the data calculated by jump conditions in Table 5.1. The details of stresses response are discussed in the following.

Table 5.3: Some results of plate impact simulations for ALON.

Simu. #	AlON Hugoniot			
	u_p (km/s)	U_s (km/s)	ε	σ (GPa)
1	1.554	8.8953	0.184	53.538
2	1.897	9.1899	0.225	66.670
3	0.525	8.0137	0.0566	18.556
3	0.881	8.3186	0.101	29.865
6	0.530	8.0184	0.0573	18.716
6	0.884	8.3219	0.102	29.931
7	2.306	9.5406	0.275	83.445
8	2.528	9.7304	0.302	92.931

Macroscopic response. Model predictions of macroscopic longitudinal and mean stresses are plotted in Figure 5.6. Shock longitudinal stress data by jumping condition analysis and mean stress response (Thornhill et al., 2005) are shown in the figure for comparison. In addition, mean stress response by simulating the relationship of the shock velocity U_s and the particle velocity u_p is also shown in Figure 5.6. The following four

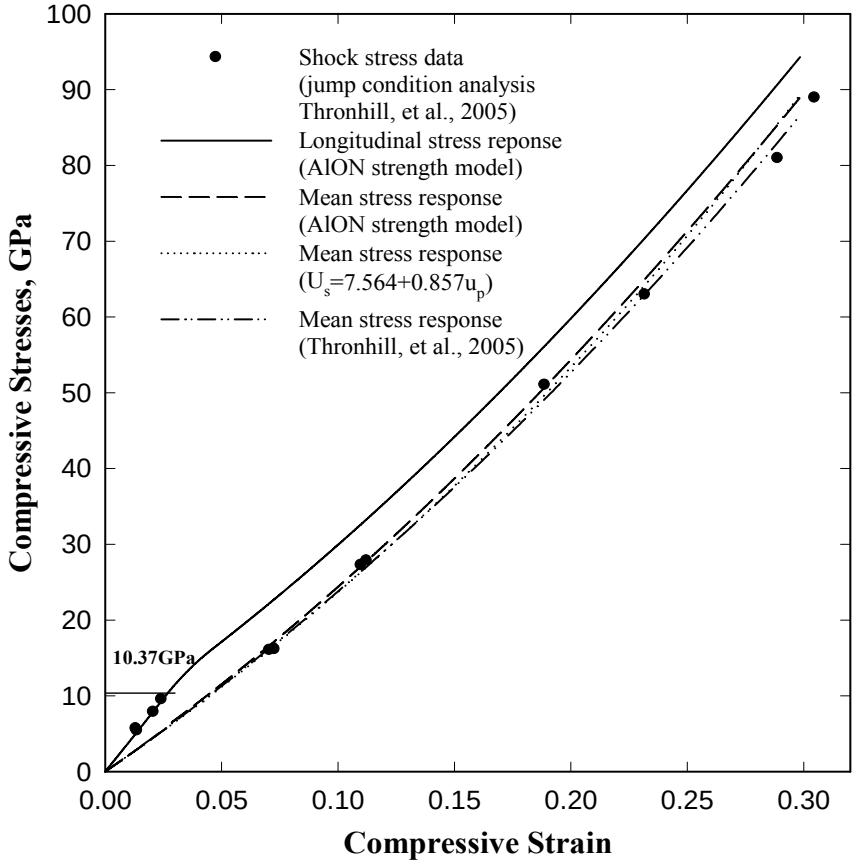

Figure 5.6: Macroscopic longitudinal and mean stress response of AlON.

significant points can be made. First, the mean stress calculations are up to 86 GPa, the longitudinal stress calculations are up to 92 GPa, and the calculated value for HEL is 10.37 GPa. Second, the mean stress calculations by using AlON strength model (dash line) can agree with the mean stress response (dash dot line) of Thornhill et al. (2005) because there only have small differences between them. Third, the longitudinal stress calculations based on AlON strength model (solid line) compare well with the shock stress data by jump condition analysis (black circle dots) of Thornhill et al. up to HEL but there have big difference between them beyond HEL. There must be some errors in the shock stress data by the jump condition analysis since the shock stress data have conflict with the mean stress response. So it can be said that the longitudinal stress response is a good prediction because it is consistent with the mean stress response. Fourth, the mean stress response by simulating the relationship of the shock velocity U_s and the particle velocity u_p compares well with that based on AlON strength model. The simulation result of the relationship is $U_s = 7.564 + 0.857u_p$.

Longitudinal stress versus particle velocity. The relationship of longitudinal stress and particle velocity is another important application for ceramics. The profile of longitudinal stress vs. particle velocity for the simulations based on AlON strength model is shown in Figure 5.7. In order to get the relationship of profile of longitudinal stress and particle velocity, the profile is fitted by a curve. The equation of the curve that fits the profile well is

$$\begin{cases} \sigma = 37.23u_p + 2.44u_p^2 & (\sigma \le 10.37GPa) \\ \sigma = -1.43 + 48.66u_p - 20.31u_p^2 & (10.37GPa < \sigma \le 15.02GPa) \\ \sigma = 3.15 + 27.94u_p + 2.99u_p^2 & (\sigma > 15.12GPa) \end{cases} \quad (5.2).$$

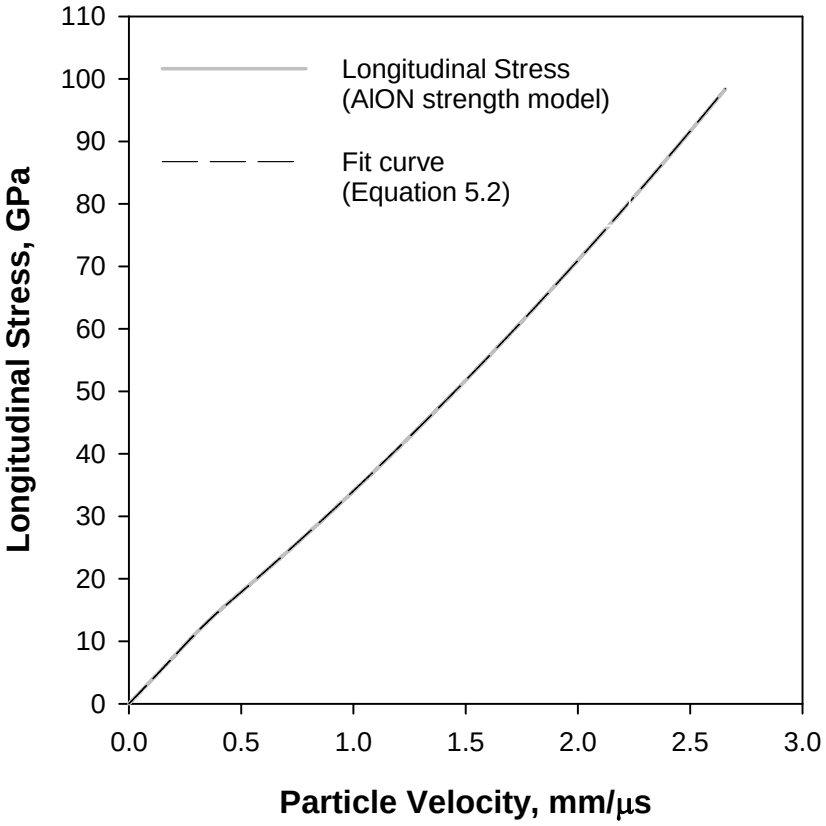

Figure 5.7: Longitudinal stress versus particle velocity of AlON.

5.3 3-D Analysis of Polycrystalline AlON

The analysis presented in this section focuses on polycrystalline model of AlON. 3-D analysis of elastic calculations and microplasticity analysis are performed because it is necessary to have a base of elastic constants C_{ij} in describing its macroscopic response to arbitrary loads and stress and the parameters of crystal microplasticity model for polycrystalline AlON. 3-D 600-grain cubic VP-FE model is developed for the simulation, presented in Section 5.3.1. The material model considers elasticity and crystal plasticity, also presented in Section 5.3.1. The elastic calculations to determine the ambient elastic constants C_{ij} of polycrystalline AlON is presented in Section 5.3.2. Microplasticity analysis to determine compressive strengths of shocked AlON are presented in Section 5.3.3.

5.3.1 Modeling and Simulations

The modeling methodology consists of three components: (1) a realistic 3-D model of polycrystalline microstructure, (2) a material model including elasticity and crystal plasticity, and (3) a solution algorithm to implement the microstructure and material model into the commercial FE code the ABAQUS/Standard for numerical analysis.

The polycrystalline microstructure is modeled using a cubic (3-D) VP-FE model with 600 grains randomly assigned crystallographic orientations. The configuration of 3-D polycrystalline model is shown in Figure 2.7. The details of methods for constructing

3-D polycrystalline model, finite element mesh and model test are described in the Chapter 2.

The simulations include elastic calculations and microplasticity analysis. The purpose of elastic calculations is to estimate a base of elastic constants C_{ij} (C_{11}, C_{12} and C_{44}) for polycrystalline AlON. In the microplasticity analysis, macroscopic longitudinal and mean stress response are obtained by using non-linear elasticity and crystal plasticity material model in which the parameters consider the same values as those used for polycrystalline Al_2O_3. The results of macroscopic response are compared with the results of plate impact experimental simulation and the parameters that selected are discussed.

For elastic calculations, the material model considers linear anisotropic elastic behavior. For a cubic material, the elasticity stiffness matrix is given by

$$\hat{\mathbf{C}} = \begin{bmatrix} C_{11} & C_{12} & C_{12} & 0 & 0 & 0 \\ & C_{11} & C_{12} & 0 & 0 & 0 \\ & & C_{11} & 0 & 0 & 0 \\ & & & C_{44} & 0 & 0 \\ & sym. & & & C_{44} & 0 \\ & & & & & C_{44} \end{bmatrix}. \tag{5.3}$$

Parameters C_{11}, C_{12} and C_{44} need to be determined through the calculations. There are two types of the loading conditions for elastic calculations. One is uniaxial-strain compression: uniform pressures are applied on the front and the back surfaces of the polycrystal, while the transverse displacements are prevented at the four lateral surfaces as shown in Figure 5.8(a). Another is hydrostatic compression: uniform pressures are applied on the all six surfaces as shown in Figure 5.8(b).

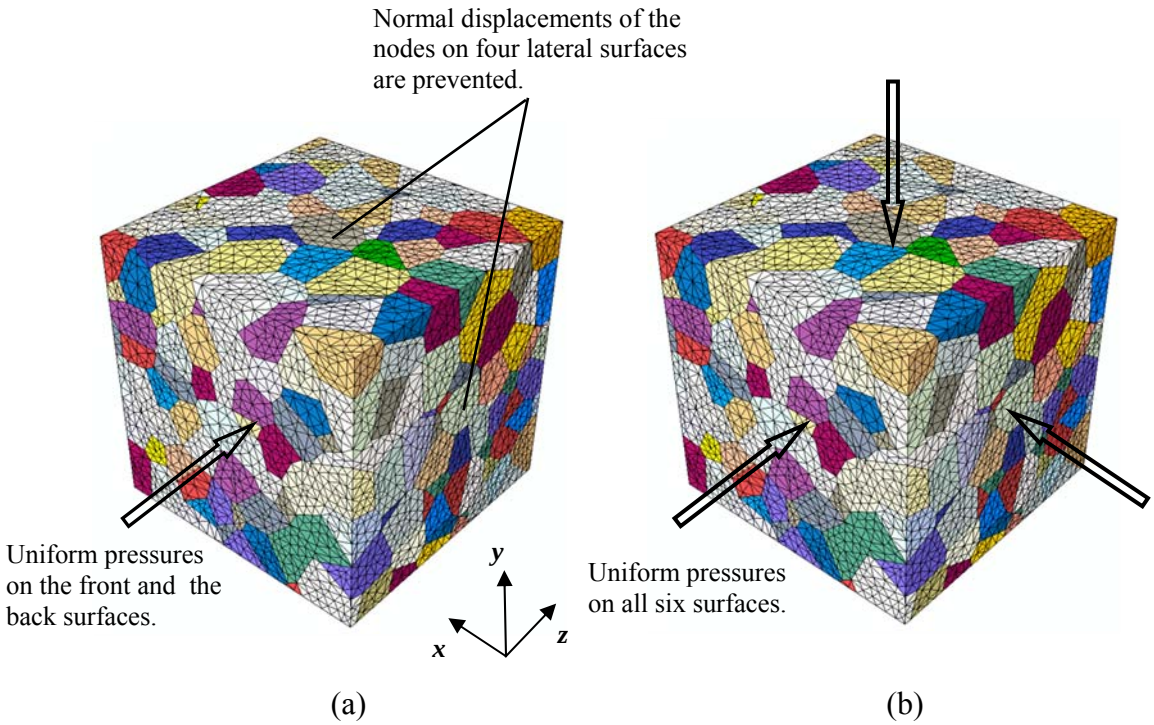

Figure 5.8: 3-D polycrystal, microstructure-preserving FE mesh, and applied loading conditions (a) uniaxial-stain compression and (b) hydrostatic strain compression.

For microplasticity analysis, the material model considers nonlinear anisotropic crystal elasticity and crystal plasticity. The slip system $\{111\}\langle 110\rangle$ is considered in the investigation. The nonlinear elasticity and crystal plasticity modeling and the solution technique by FE method have been introduced in Section 2.3. The loading condition is uniaxial-strain compression.

3-D FE mesh preserving the polycrystalline microstructure (Figure 5.8), material model and loading conditions are implemented into the commercial FE code, the ABAQUS/Standard for numerical analysis. The procedure of the elastic calculations and

the results are presented below are presented in Section 5.3.2. Microplasticity analysis and the results are presented in Section 5.3.3.

5.3.2 Elastic Calculations and Results

Numerical simulations to determine the elastic constants C_{11}, C_{12} and C_{44} of polycrystalline AlON under uniaxial-strain and hydrostatic-strain compressions are performed using a 600-grain 3-D VP-FE model and the ABAQUS/Standard FE analysis. The procedure to determine C_{11}, C_{12} and C_{44} is as follows.

Trial sets of parameters C_{11}, C_{12} and C_{44} for calculations are selected first. For a cubic material, $C_{44} \neq (C_{11} - C_{22})/2$ in general. Parameters C_{11}, C_{12} and C_{44} of its crystals may be approximated by the following equations (Frank et al., 1996)

$$\begin{cases} C_{11} = L - \dfrac{2}{5}H \\ C_{12} = L - 2\mu + \dfrac{1}{5}H \\ C_{44} = \mu + \dfrac{1}{5}H \end{cases}, \tag{5.4}$$

where L and μ are the longitudinal modulus and shear modulus of the polycrystalline bulk form of the material, respectively; H is the characteristic parameter for cubic material. In the current study, the values of H are selected from -100 GPa to 100 GPa (except for 0 GPa) in 10 GPa step. So there are totally 20 sets of parameters for calculations.

The calculations under the two type loading conditions (uniaxial-strain and hydrostatic-strain compressions) are then performed. For a trial set of C_{11}, C_{12} and C_{44}, the ratio of volume-averaged longitudinal stress over volume-averaged longitudinal strain, that of volume-averaged mean stress over volume-averaged volumetric strain, and that of volume-averaged normal stress difference over volume-averaged normal strain difference from the uniaxial-strain compression calculation gives respectively the resulting longitudinal modulus L', bulk modulus K', and shear modulus μ' of the polycrystalline material corresponding to the trial set of parameters. The hydrostatic compression calculation yields only the bulk modulus of the trial polycrystal. The result provides an independent check for the bulk modulus. The shear modulus of the trial polycrystal can be checked independently using μ' $[= 3(L' - K')/4]$.

Three small load levels of 0.5 GPa, 2 GPa and 5 GPa are used for each type loading condition to examine the effect of load level. The modulus results of the trial polycrystal need to compare with a reference or experimental data. The values of $L = 388\,\text{GPa}$, $\mu = 126.5\,\text{GPa}$ and $K = 219.3\,\text{GPa}$ (McCauley, 2006) are selected as the reference moduli. There are totally 120 sets of results (not shown in this chapter) obtained. From the analysis of the results, we find, when H is equal to -60 GPa ($C_{11} = 412.0GPa$, $C_{12} = 123.0GPa$ and $C_{44} = 114.0GPa$), the results are close to the reference data. For a better match with the reference data, parameter C_{44} is further changed from 114.0 GPa to 118.0 GPa because the crystal shear modulus makes the biggest difference in the resulting polycrystal moduli. The results of this set of parameters: $C_{11} = 412.0\,\text{GPa}$, $C_{12} = 123.0\,\text{GPa}$ and $C_{44} = 118.0\,\text{GPa}$ are shown in Table 5.4. The

following three significant points can be made. First the results can match well with reference data. Second, the result can be verified through different loading conditions of uniaxial-strain compressions and hydrostatic-strain compressions. There have some differences between them, but they are not significant. Third, with load increasing, the differences between the predicted results and the reference data increase only slightly. The effect of load level is also small. This set of parameters $C_{11} = 412.0\,\text{GPa}$, $C_{12} = 123.0\ \text{GPa}$ and $C_{44} = 118.0\,\text{GPa}$ can be used as the ambient elastic constants of polycrystalline AlON.

Table 5.4: Some results of elastic analysis for AlON.

($C_{11} = 412.0\,\text{GPa}$, $C_{12} = 123.0\,\text{GPa}$ and $C_{44} = 118.0\,\text{GPa}$; $L = 388\ \text{GPa}$,

$\mu = 126.5\,\text{GPa}$ and $K = 219.3\,\text{GPa}$)

Loading Conditions	Uniaxial-Strain Compressions			Hydrostatic Compressions		
Loads (GPa)	0.5	2.0	5.0	0.5	2.0	5.0
L' (GPa)	388.04	387.74	385.55			
μ' (GPa)	126.55	126.40	124.99			
K' (GPa)	219.34	219.21	218.90	219.33	218.94	218.41

5.3.3 Microplasticity Analysis

The modeling methodology consists of three components: (1) a realistic 3-D model of polycrystalline microstructure, (2) a material model including compression-dependent elastic stiffening and crystal plasticity, and (3) a solution algorithm to implement the microstructure and material model into the commercial FE code the ABAQUS/Standard for numerical analysis.

The polycrystalline microstructure is modeled using a cubic (3-D) VP-FE model with 600 grains, as shown in Figure 5.8 (a). Since the loading condition is uniaxial-strain compression, uniform pressure is applied on the front surface and the back surface of the polycrystal and the transverse displacements are prevented at the four lateral surfaces.

Focusing on the effects of microplasticity in polycrystalline AlON under uniaxial-strain compression, the elastic properties of shocked AlON, C_{ij} ($C_{11} = 412.0\,\text{GPa}$, $C_{12} = 123.0\,\text{GPa}$ and $C_{44} = 118.0\,\text{GPa}$) which obtained through previous elastic analysis are used. The material modeling of nonlinear elasticity and crystal plasticity and the solution technique by FE method have been introduced in Section 2.3.

The nonlinear elastic model is described in Eqs. (2.4a)-(2.4c), and the model parameter A = 4.3 is determined by fitting a linear function to the bulk modulus-volumetric compression relationship derived from the 2-D plate impact simulation of the mean stress response of a polycrystalline AlON under plane shock wave compression.

The slip system $\{111\}\langle 110\rangle$ is considered in the microplasticity analysis. This is the primary slip system of spinel ceramic crystals (Hornstra, 1960; Mitchell, 1999). The

slip plane and the slip direction are shown in Figure 5.9. The selection of constitutive parameters for crystal plasticity is based on the assumptions of rate-independent and non-hardening plasticity similar to those used for polycrystalline Al_2O_3 [see Section 3.2.3].

Model predictions of macroscopic longitudinal and mean stresses (volume-

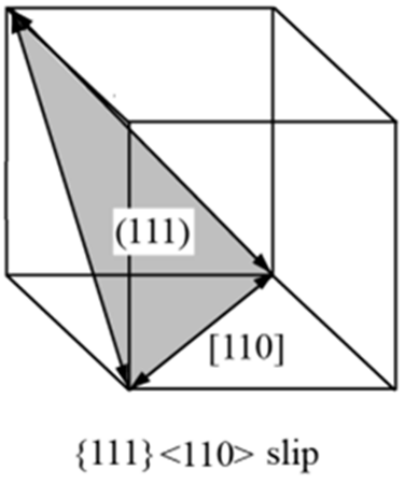

Figure 5.9: The slip system in AlON (spinel ceramic) crystals.

averaged values) from the 3-D microplasticity analysis are plotted in Figure 5.10. Each calculation obtains a point, shown as a black circle in the figure. Longitudinal stress response by 2-D plate impact experimental simulations and mean stress data are shown in the figure for comparison. For the presumed the slip system $\{111\}\langle 110\rangle$, an optimized CRSS value of $\tau_c = 3.35$ GPa is obtained by matching the macroscopic response results of the 3-D ploycrystal model simulations with those of the 2-D plate impact experimental simulations. The microplasticity model prediction captures the transition to the softer

response at HEL, and the calculated value for HEL agrees well with the experimental data of 10.37 GPa.

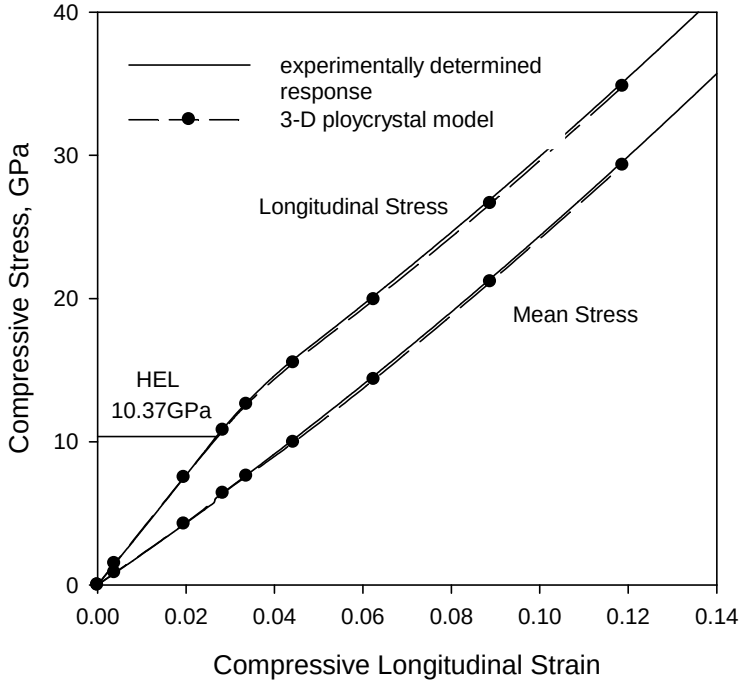

Figure 5.10: Macroscopic compressive longitudinal and mean stresses response of 3-D microplasticity analysis and experimentally determined response on AlON.

According the results of plate impact experimental simulations, the preliminary 3-D microplasticity analysis is simply studied. Since the results of strength of polycrystalline AlON need to be verified by the experiment data, we will consider the detailed investigations, such as the different slip systems, the values of CRSS's parameters τ_c and effective plastic strain distributions, in the future works after the

experiments for measuring the effective compressive strength of AlON. The next step of the future works is to design the experimental measurement for the shock strength for polycrystalline AlON. Since the simulations of 3-D analyses provide the first round for material selection and configuration design. A method using a pressure manganin gauge to measure the high strengths of polycrystalline ceramics is suggested and it is used for polycrystaliine SiC-N. The detail of experimental design and gauge simulations for polycrystalline SiC-N are presented in the Chapter 6.

5.4 Summary

In this chapter, plate impact experimental simulations and 3-D polycrystal analysis have been carried out to investigate the strength of polycrystalline AlON under shock compression. The plate impact experimental simulations employ FE models of published experiments, and consider the pressure–dependent shock strength model that combines the Drucker-Prager plasticity with a limited strength cap and the model of nonlinear compression dependence bulk modulus as the material model. FE models and the material model are implemented into ABAQUS/Explicit code with User-material Subroutine for finite element analysis. A series of wave profiles simulations of plate impact experiments on ALON are performed. The 3-D polycrystal analysis employs a 600-grain cubic VP-FE model. Material models consider elasticity and crystal plasticity. FE models and the material model are implemented into ABAQUS/Standard code with User-material Subroutine for finite element analysis. Elastic calculations and

microplasticity analysis are performed. The results of strength of polycrystalline AlON and strength properties are obtained.

Numerical results for plate impact experimental simulations show that: (1) the wave profiles of AlON-LiF interfacial velocities compare very well with the experimental measurements, (2) material strength model compares very well with the experimental data, and the optimized parameters for the strength model are: $p_0 = -0.35\,\text{GPa}$, $\beta = 32.14^\circ$, $q_0 = 5.06\,\text{GPa}$, $\alpha = 1.8$, and $\lambda_0 = 126.33\,\text{GPa}$, $\mu_0 = 126.5\,\text{GPa}$, $B = 4.25$, (3) the macroscopic response of longitudinal stress and mean stress are obtained, longitudinal stress response is consistent with the mean stress response, the HEL of AlON is 10.37 GPa, and the relationship of the shock velocity U_s and the particle velocity u_p is $U_s = 7.564 + 0.857u_p$, and (4) the relationship of longitudinal stress and particle velocity is obtained.

Numerical results of elastic calculation for polycrystalline AlON show the followings. First the results can match well with reference data. Second, the result can be verified through different loading conditions of uniaxial-strain compressions and hydrostatic-strain compressions. Third, with the loads increasing, the differences between the results of the moduli and reference data increase, but the effect of the loads is not big. This set of this set of parameters $C_{11} = 412.0\,\text{GPa}$, $C_{12} = 123.0\,\text{GPa}$ and $C_{44} = 118.0\,\text{GPa}$ can be used as the elastic constants of polycrystalline AlON.

Numerical results show that 3-D ploycrystal modeling and microplasticity analysis for polycrystalline AlON by using a nonlinear elasticity parameter A = 4.3 and the slip system $\{111\}\langle 110\rangle$ with the CRSS's value of τ_c = 3.35 GPa can match the macroscopic response determined by the plate impact experimental simulations. The calculated value for HEL is 10.37 GPa, which agrees well with the analyzed experimental data (10.37 GPa). To measure the strength of shocked polycrystalline AlON directly, a method using manganin stress gauges in both the longitudinal and lateral configurations is suggested. The gauge calibrations for the two configurations are determined from numerical simulations of the calibration experiments on a polycrystalline a-6H silicon carbide (SiC-N), for which the shock response and strength are known. The details of experimental design and simulations of gauge calibration experiments on SiC-N are presented in Chapter 6.

CHAPTER 6

NEW FINITE ELEMENT PIEZORESISTANCE MODEL AND GAUGE SIMULATIONS

6.1 Introduction

The shear strength of a solid under shock wave compression is critically important for its applications in impact engineering. However, if the material's inelastic response differs from that of the classical plasticity as observed for ceramics and other brittle solids, the material shear strength in the shocked state cannot be uniquely determined from a conventional plate impact shock wave experiment that measures only the longitudinal stress or particle velocity (one can be determined from the other through the momentum equation) (Feng et al., 1997). The macroscopic loading condition in such an experiment is that of uniaxial strain, which, for an isotropic material, gives rise to one longitudinal principal stress in the shock wave direction and two equal-magnitude lateral principal stresses in the two orthogonal transverse directions. Hence, the maximum shear stress sustained by the material in the shocked state is one half of the difference between the longitudinal and lateral principal stresses. In other words, the shear strength of the

material in the shocked state can be determined from a plate impact experiment if both the longitudinal and lateral stresses measured.

Thin piezoresistance foils have been widely used as stress gauges in shock wave experiments. Although embedding such a gauge in a solid sample introduces a heterogeneous layer (composed of gauge foil, packaging material and bonding material) into the sample, its adverse effects are limited to the rise of measured stress profile when the embedding layer is facing the shock wave direction. The steady state gauge response in this longitudinal gauge configuration can be experimentally calibrated and uniquely related to the sample material's longitudinal stress under uniaxial-strain shock compression through the gauge calibration. It would seem a natural and straightforward extension of the longitudinal gauge technique to embed a piezoresistance stress gauge transversely in a solid sample to measure its lateral stress in the shocked state. In fact, such a lateral gauge technique has been studied extensively (Feng et al., 1997; Hammond et al., 2004; Winter et al., 2008). Unfortunately, it has been found that unlike a longitudinal gauge layer a transverse gauge installation layer makes the sample material loading condition in the vicinity of the layer deviate from that of uniaxial strain (Feng et al., 1997; Hammond et al., 2004). Consequently, the lateral stress measured the gauge may differ from the desired uniaxial-strain lateral stress. The error in the shear strength determined with such a measurement increases with the layer thickness and the impedance difference between the sample and the layer.

An iterative lateral gauge analysis procedure based on accurate two-dimensional computational modeling of the interactions of lateral gauge with bonding epoxy and shocked solid sample was proposed to deal with this issue (Feng et al., 1997) and applied successfully in a series of lateral manganin gauge experiments for measuring the lateral stress in a polycrystalline α–6H silicon carbide (Cercom SiC-B material) under shock compression (Feng et al., 1998). The gauge analysis is however specialized for a particular type of low-impedance manganin gauges fabricated in the Institute for Shock Physics at the Washington State University. Accurate model of the manganin foil's elastoplastic response and determination of its piezoresistivity tensor are prerequisites of the analysis. Neither is available for commercial manganin gauges, which are standardized and convenient to use. In particular, VISHAY 580SF manganin gauge with 200 μm effective width and 5 μm thickness as shown in Figure 6.1 is configurationally optimized for lateral gauge applications. However, a reliable method for using this type of gauges to accurately determine the lateral stresses in solids under *uniaxial-strain* shock compression is lacking.

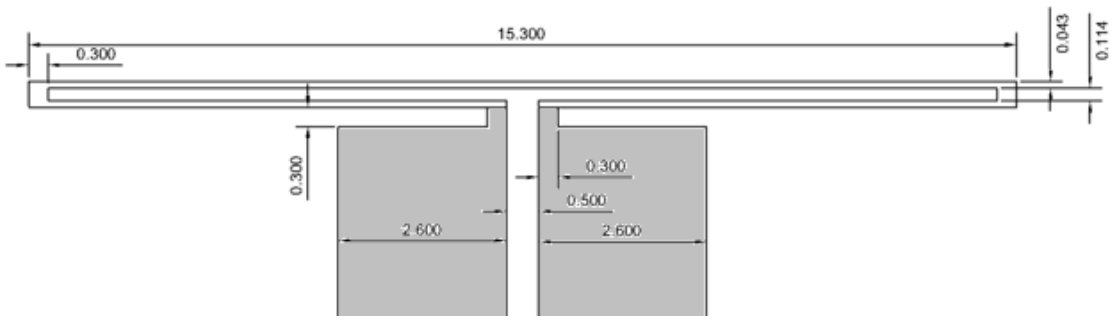

Figure 6.1: Dimensions of the manganin element of VISHAY 580SF gauge in mm

The objectives of this joint research project are to develop a gauge analysis method that can accurately interpret the measurements of VISHAY 580SF manganin gauges in the lateral gauge configuration and reliably infer from them the lateral stress reposnse of the sample material under shock wave compression, and to apply the method to determine the shear strength of shocked ceramics. The plate impact shock wave experiments necessary to complete this project were carried out and will be completed by the colleagues at U.S. Army Research Laboratory. Presented in this chapter are the iterative gauge analysis procedure, gauge piezoresistance model, and three-dimensional (3D) finite element (FE) gauge model developed for VISHAY 580SF manganin gauge as well as the preliminary results for the gauge piezoresistance model calibration and the lateral gauge response simulations.

The iterative gauge analysis procedure considered in this work is based on 3D FE modeling of a VISHAY 580SF manganin gauge embedded transversely in a solid subjected to prescribed shock compression and a trial lateral gauge calibration. First, the lateral gauge measurements obtained in the material intended to characterize will be converted to the *trial* lateral stress response by using the trial lateral gauge calibration. The results, in conjunction with the known longitudinal stress response in the shocked state (which may be determined independently from conventional plate impact shock wave experiment on the material), will then be used to construct a trial shear strength model for the material. Next, numerical simulations with this trial strength model and the 3D FE model for the gauge-sample assembly will be carried out to compute the lateral gauge output for the loading condition of each of the lateral gauge experiments. If the

computed lateral gauge response matches the experimental measurements, the trial strength model is a proven good representation of the shear strength of the material under shock wave compression. Otherwise, the trial lateral stress response will be modified accordingly and the next round iteration proceeds.

Unlike the work reported in Feng et al., 1998. where the initial trial lateral gauge calibration was calculated from the known elastoplastic and piezoresistive responses of the gauge material, the mechanical and piezoresistive properties of VISHAY 580SF gauge material, a thin layer of manganin printed on a polymeric backing material are not exactly known and are very difficult to measure independently. Therefore, we consider an empirical piezoresistance model for VISHAY 580 SF gauge, calibrate the model and determine the needed initial trial lateral gauge calibration through combined gauge calibration experiments using a matrix material whose shock strength behavior is known and 3D FE modeling of the experiments. Since the technique will be used primarily for determining the shear strength of shocked brittle solids, polycrystalline α–6H silicon carbide is used as the matrix for the calibration experiments.

New finite element piezoresistance modeling is developed in Section 6.2. Three-dimensional (3-D) finite element gauge model developed for VISHAY 580SF manganin gauge and gauge simulations are presented in Section 6.3. The preliminary results for the gauge piezoresistance model calibration and the lateral gauge response simulations are presented in Section 6.4. Section 6.5 summarizes the key findings of gauge simulations presented in this chapter.

6.2 New Finite Element Piezoresistance Model

Piezoresistance Model for Foil Gauge. The resistance of a homogeneous conductor with uniform cross section can be related to the conductor material resistivity ρ, the conductor length l and the conductor cross-sectional area A as follows:

$$R = \rho l/A. \tag{6.1}$$

The interpretation for ρ is not unique in the literature and the one given by Arlt states:

$$\text{Conductivity} \equiv \frac{1}{\rho} = \frac{Nn_c e\psi}{V}, \tag{6.2}$$

where N is the absolute number of atoms in the conductor, n_c the number of free electrons per atom, e the electronic charge, ψ the electron mobility, and V the conductor volume. Substituting Eq. (6.2) into Eq. (6.1) and noticing that $V = lA$ gives

$$R = (l^2/Nn_c e)(1/\psi). \tag{6.3}$$

For the range of loading conditions of interest, the product of $Nn_c e$ is constant. Hence,

$$\Delta R/R_0 = (l/l_0)^2(\psi_0/\psi) - 1, \tag{6.4}$$

where $\Delta R \equiv R - R_0$ and subsprit 0 denotes the quantities in the initial undeformed state. The above resistance change equation for a homogeneous and uniform conductor is different from that of the conventional strain gauge theory and that of the previous model for piezoresistance gauges (Feng et al., 1997) in that it does not explicitly involve strains in the directions tranverse to the electric current direction. The normalized

resistance change $\Delta R/R_0$ depends on the current direction conductor stretch squared and on the ratio of the electron mobility in initial undeformed lattice to that in the deformed lattice. The lattice deformation can be related unique to the elastic strain of the conductor and thus to its stress state. In other word, the gauge resistance change is sensitive to both conductor strain and stress. Since a stress state can be fully characterized by the corresponding principal stresses, the mobility ratio ψ_0/ψ may be written as

$$\psi_0/\psi = f(\sigma_1, \sigma_2, \sigma_3\,). \tag{6.5}$$

Along a given loading path, for which the stress normal to the conductor σ_{N} dictates the variations of the principal stresses, we may reasonably approximate *f* with the following relation:

$$f = \pi\sigma_{\mathrm{N}} + 1, \tag{6.6}$$

where π is the effective piezoresistivity coefficient along the loading path and can be a function of σ_{N}. Since the existence of unique longitudinal gauge calibration is a widely observed fact, the above approximation is appropriate for a piezoresistance gauge in the longitudinal gauge configuration. The validity of Eq. (6.6) for a piezoresistance gauge in the lateral gauge configuration will be examined in the current work. Substituting Eqs. (6.5) and (6.6) into Eq. (6.4) yields

$$\Delta R/R_0 = (l/l_0)^2(\pi\sigma_{\mathrm{N}} + 1) - 1. \tag{6.7}$$

New FE piezoresistance model for VISHAY 580SF manganin gauge. The manganin pressure gauge is one of the most used sensors in shock wave experiments. Manganin is a copper–manganese-nickel alloy with low strain sensitivity, but a relatively

high sensitivity to hydrostatic pressure. Resistance change as a function of applied pressure is linear to extremely high pressure. Manganin pressure gauges are special–purpose sensor with manganin foil grid for measuring hydrostatic pressure and for shock wave studies. The VISHAY 580SF pattern of manganin pressure gauge is chosen for the experiment because it is designed especially for investigating the effects of sweeping explosive waves. A typical manganin 580SF gauge is shown in Figure 6.1. During the experiment, the manganin gauge is embedded in the sample. The resistance change history is recorded. Hence, new FE piezoresistance model for numerical method to calculate the gauge resistance change is developed. In the numerical calculations, different elements representing the gauge foil have different mechanical states resulting in different values of resistance change. The active foil of manganin gauge with elements is shown in Figure 6.2. The gauge foil has an initial total length L_0 with total N segments. In the jth segment, it has an initial length $L_0^{(j)}$ with n_j parallel elements. The new FE piezoresistance model is derivate as the follows.

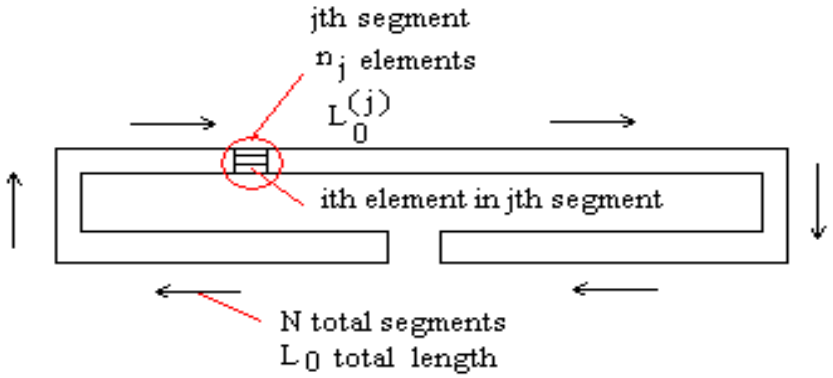

Figure 6.2: Schematic view of gauge foil with elements.

In the numerical calculations by using new FE piezoresistance model, the relative gauge resistance change, Eq.(6.7), can be written as

$$\frac{\Delta R}{R_0} = \frac{R - R_0}{R_0} = \left(\frac{L}{L_0}\right)^2 (\alpha\sigma_z + 1) - 1 . \qquad (6.8\ a)$$

where R is the current gauge resistance, R_0 is the initial gauge resistance, $\frac{\Delta R}{R_0}$ is the gauge resistance change, L_0 is the initial total length, L is the current total length, α is the parameter, and σ_z is the stress in the gauge with z axis being in the direction of electrical current. So, the rate between the current resistance and initial resistance can be written as

$$\frac{R}{R_0} = \left(\frac{L}{L_0}\right)^2 (\alpha\sigma_z + 1) . \qquad (6.8\ b)$$

The initial resistance and current resistance of the No. *jth* segment are calculated by

$$\frac{1}{R_0^{(j)}} = \sum_{i=1}^{n_j} \frac{1}{R_{0i}^{(j)}} \qquad \Rightarrow \qquad R_0^{(j)} = \frac{R_{0i}^{(j)}}{n_j} , \qquad (6.9\ a)$$

and

$$\frac{1}{R^{(j)}} = \sum_{i=1}^{n_j} \frac{1}{R_i^{(j)}} \qquad \Rightarrow \qquad R^{(j)} = \frac{1}{\sum_{i=1}^{n_j} \frac{1}{R_i^{(j)}}} . \qquad (6.9\ b)$$

where $R_0^{(j)}$ is the initial resistance of *jth* segment, $R^{(j)}$ is the current resistance of *jth* segment, n_j is the total number of elements in *jth* segment, *i* is the No. *ith* element in *jth*

segment, $R_{0i}^{(j)}$ is the initial resistance of *ith* element in *jth* segment (it is equal for all the n_j elements), $R_i^{(j)}$ is the current resistance of *ith* element in *jth* segment.

Then the current resistance and initial resistance of the whole gauge foil are calculated by

$$R = \sum_{j=1}^{N} R^{(j)} \quad \overset{(Eq.6.9b)}{\Rightarrow} \quad R = \sum_{j=1}^{N} \frac{1}{\sum_{i=1}^{n_j} \frac{1}{R_i^{(j)}}}, \tag{6.10a}$$

and

$$R_0 = \frac{L_0}{L_0^{(j)}} R_0^{(j)} \quad \overset{(Eq.6.9a)}{\Rightarrow} \quad R_0 = \frac{L_0}{L_0^{(j)}} \frac{R_{0i}^{(j)}}{n_j}. \tag{6.10b}$$

where $L_0^{(j)}$ is the initial length of the *jth* segment, N is the total number of segments. So, the rate between the current resistance and initial resistance can be written as

$$\frac{R}{R_0} = \sum_{j=1}^{N} \frac{1}{R_0 \sum_{i=1}^{n_j} \frac{1}{R_i^{(j)}}} = \sum_{j=1}^{N} \frac{n_j L_0^{(j)}}{L_0 \sum_{i=1}^{n_j} \frac{R_{0i}^{(j)}}{R_i^{(j)}}}. \tag{6.11}$$

For the *ith* element in *jth* segment, the rate of the initial resistance and current resistance can be written as Eq. (6.8b) by

$$\frac{R_i^{(j)}}{R_{0i}^{(j)}} = \left(\frac{L_i^{(j)}}{L_{0i}^{(j)}} \right)^2 (\alpha \sigma_{zi}^{(j)} + 1). \tag{6.12}$$

where $L_{0i}^{(j)}$ is the initial length of *ith* element in *jth* segment, $L_i^{(j)}$ is the current length of *ith* element in *jth* segment, and $\sigma_{zi}^{(j)}$ is the stress of *ith* element in *jth* segment with z axis being in the direction of electrical current.

For the *ith* element in *jth* segment, the strain can be written as

$$\varepsilon_{li}^{(j)} = \ln\left(\frac{L_i^{(j)}}{L_{0i}^{(j)}}\right) \qquad \Rightarrow \frac{L_i^{(j)}}{L_{0i}^{(j)}} = \exp\left[\varepsilon_{li}^{(j)}\right]. \tag{6.13}$$

Substituting Eqs. (6.12) and (6.13) into Eq. (6.11), the rate between the current resistance and initial resistance can be written as

$$\frac{R}{R_0} = \sum_{j=1}^{N} \frac{n_j L_0^{(j)}}{L_0 \sum_{i=1}^{n_j} \frac{R_{0i}^{(j)}}{R_i^{(j)}}} = \sum_{j=1}^{N} \frac{n_j L_0^{(j)}}{L_0 \sum_{i=1}^{n_j} \frac{1}{\exp[2\varepsilon_{li}^{(j)}](\alpha\sigma_{zi}^{(j)} + 1)}}. \tag{6.14}$$

The gauge resistance change of the whole gauge foil can be obtained by

$$\frac{\Delta R}{R_0} = \frac{1}{L_0} \sum_{j=1}^{N} \frac{n_j L_0^{(j)}}{A} - 1, \tag{6.15}$$

where $A = \sum_{i=1}^{n_j} \frac{1}{\exp[2\varepsilon_{li}^{(j)}](\alpha\sigma_{zi}^{(j)} + 1)}$.

6.3 3-D Finite Element Modeling and Gauge Simulations

6.3.1 Longitudinal Gauge Simulation

The configuration of a typical longitudinal gauge experiment is shown schematically in Figure 6.3 (a). The impactor is copper with 5.9 mm thick. The target is ceramic sample - manganin gauge sandwich. A schematic view of ceramic sample - manganin gauge assembly is shown in Fig.3 (b). The front sample plate is 5.83mm thick and the black sample plate is 13.12mm thick. A manganin foil gauge (0.01mm thick) is

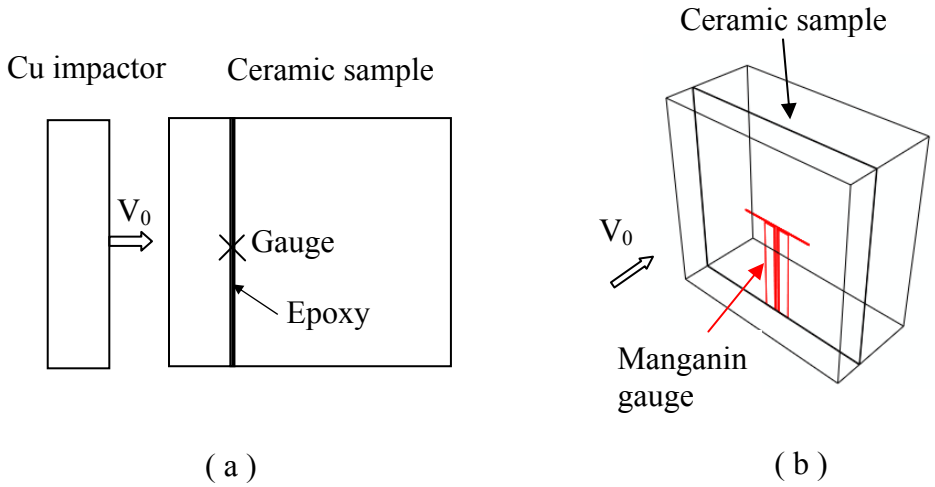

Figure 6.3: Schematic view of a longitudinal gauge experiment. (a) Impact configuration, (b) ceramics sample- manganin gauge assembly.

glued between two plates of the ceramic sample with a thin layer of epoxy. The total thickness of the epoxy-gauge layer is approximately 0.14 mm. The impact velocity is V_0.

3-D Finite element model for the configuration of a typical longitudinal gauge experiment is developed. The epoxy-gauge bond part is modeled three layers: the front epoxy (0.06 mm thick), the middle layer with the gauge (0.01 mm thick) and the back

epoxy (0.07mm thick). The constraint of ABAQUS/Explicit Tie is used to assemble all the epoxy layers and two samples together. The interaction of the impactor and the front sample is modeled as ABAQUS/Explicit Surface to Surface Contact. The mesh of the model is shown in Figure 6.4 (a), a zoom view of the epoxy–gauge three layers (in y-z plane) is shown in Figure 6.4 (b), and partial mesh of manganin gauge is shown in Figure 6.4 (c). All the elements are 3-D solid 8- node elements.

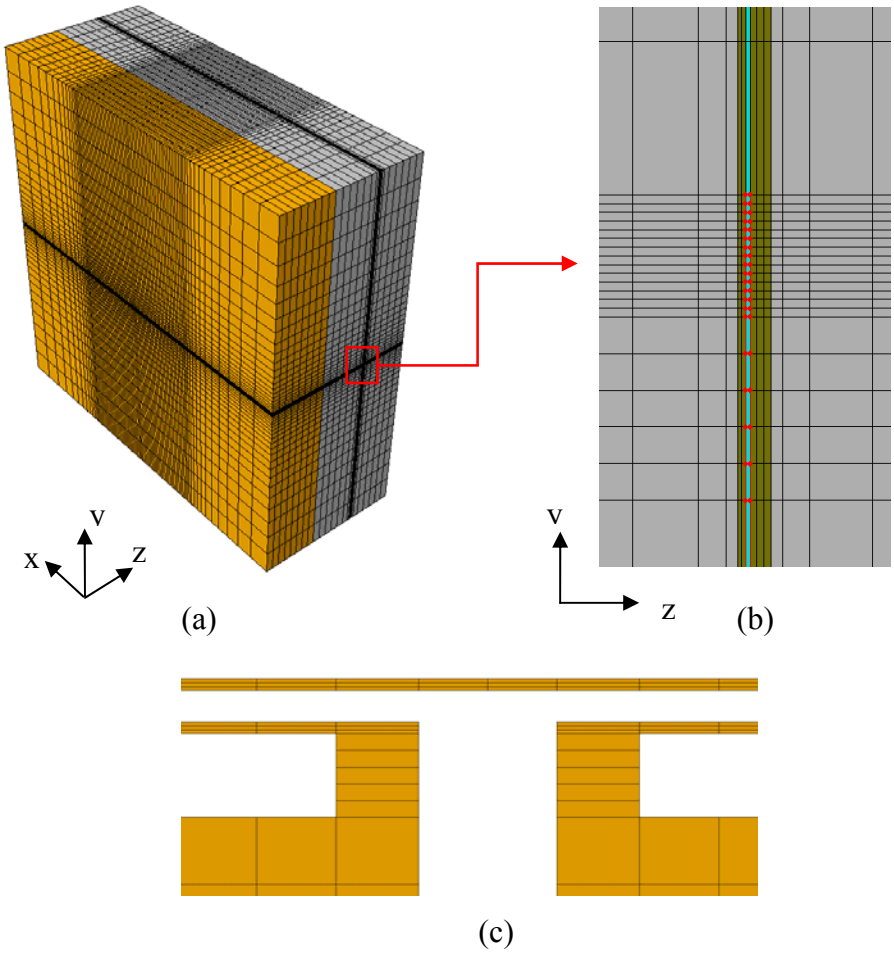

Figure 6.4: 3-D FE model for longitudinal gauge experiment. (a)model mesh, (b) a zoom view of the epoxy three layers, and (c) partial mesh of manganin gauge.

The copper is employed as the hydrodynamic models (Feng and Gupta, 1994 & 1996). The parameters of the cooper material model are shown in Table 5.2. The epoxy is modeled as an elastic-plastic material with a constant strength of 0.05GPa. An initial density of 1184 kg/m^3 is assumed. The manganin foil is modeled as a cooper material. The 3-D FE model and material models are implemented into ABAQUS/Explicit code for FE analysis. The results of longitudinal stress response are obtained and gauge resistance changes are calculated by Eq.(6.15). The details of results are presented in Section 4.4.

6.3.2 Lateral Gauge Simulation

The configuration of a typical Lateral gauge experiment is shown schematically in Figure 6.5 (a). The impactor is copper with 5.9 mm thick. The target is ceramic buffet and sample-manganin gauge assembly. Ceramic buffer is 2.5 mm thick. The thickness of

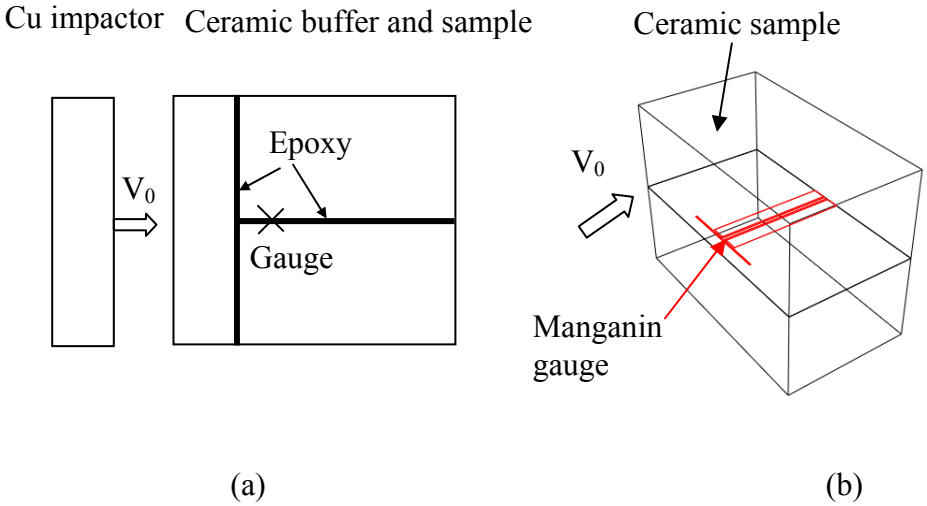

Figure 6.5: Schematic view of a lateral gauge experiment. (a) Impact configuration, (b) ceramics sample- manganin gauge assembly.

ceramic sample is 22.0 mm including the top and bottom two slabs. The manganin gauge (0.01mm thick, 2 mm away from the back edge of ceramic buffet) is directly glued between the two slabs of the ceramic sample with a thin layer of epoxy, shown in Figure 6.5 (b), and then the sample-manganin gauge assembly and the buffer are glue together. The total thickness of the epoxy-gauge layer is approximately 0.14 mm. The impact velocity is V_0.

3-D Finite element model for the configuration of a typical lateral gauge experiment is developed. The epoxy-gauge bond part is modeled three layers: the top layer (0.06 mm thick), the middle layer with the gauge (0.01 mm thick) and the bottom layer (0.07mm thick). The constraint of ABAQUS/Explicit Tie is used to assemble the epoxy-gauge bond part and two slabs of the ceramic sample together, as well as the sample-manganin gauge assembly, epoxy, and the buffer. The interaction of the impactor and the front of ceramic buffer is modeled as ABAQUS/Explicit Surface to Surface Contact. The mesh of the model is shown in Figure 6.6 (a), a zoom view of the epoxy–gauge three layers (in y-z plane) is shown in Figure 6.6 (b), and partial mesh of manganin gauge is shown in Figure 6.6 (c). All the elements are 3-D solid 8- node elements.

The copper is employed as the hydrodynamic model (Feng and Gupta, 1994 & 1996). The parameters of the cooper material model are shown in Table 5.2. The manganin foil is modeled as a cooper material. The epoxy is modeled as an elastic-plastic material with a constant strength of 0.05GPa. An initial density of 1184 kg/m^3 is assumed. The other parameters of epoxy are: $c_0 = 2727\, m/s$, $s = 1.469$, $\Gamma_0 = 0.742$ and $G = 2.0$ GPa.

The 3-D FE model and material models are implemented into ABAQUS/Explicit code for FE analysis. The results of lateral stress response are obtained and gauge resistance changes are calculated by Eq.(6.15). The details of results are presented in Section 4.4.

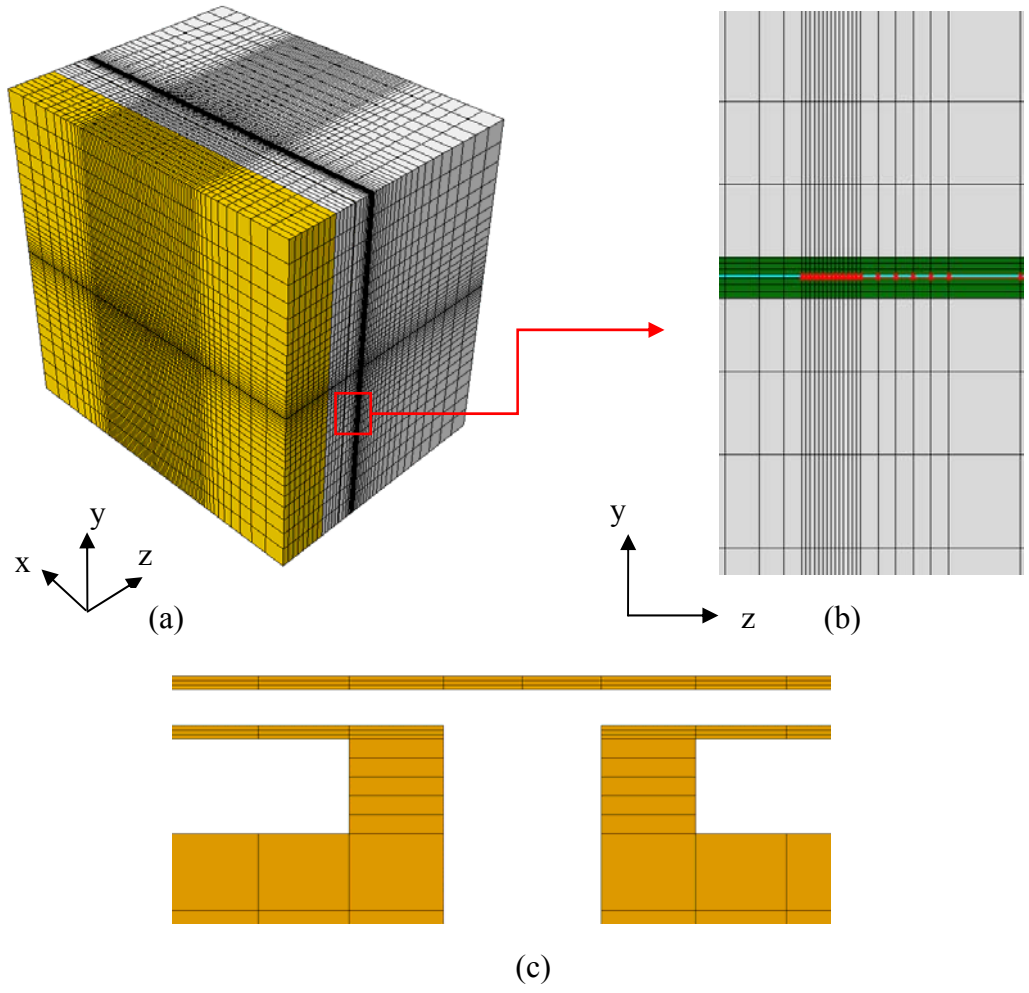

Figure 6.6: 3-D FE model for lateral gauge experiment. (a) model mesh, (b) a zoom view of the epoxy three layers, and (c) partial mesh of manganin gauge.

6.4 The results for the gauge simulations

A sample test of longitudinal gauge on SiC-N sample is carried out at the lower impact velocity. V_0 is equal to 314m/s. Model prediction of gauge resistance change for this sample test compares well with the experimental data. In addition, numerical simulations of longitudinal and lateral gauge experiments at other higher impact velocity are carried out. The simulation results of longitudinal and lateral stresses response provide the important information for performing the gauge experiments. The preliminary simulation result of the sample test for piezoresistance model calibration is presented in Section 6.4.1. The simulation results of longitudinal gauge experiments are presented in Section 6.4.2. Section 6.4.3 shows the simulation results of lateral gauge experiments.

6.4.1 The Preliminary Simulation Result of a Sample Test

A test of longitudinal gauge on SiC-N sample is carried out at the impact velocity 314m/s by using the configuration of a longitudinal gauge experiment shown in Figure 6.3. The gauge resistance change is record. The numerical simulation of this test is carried out. The material model of SiC-N is employed as effective strength model and nonlinear bulk modulus, which are described in Section 5.2.1. The parameters are obtained by plate impact simulation of the experiment by Volger et al. (Volger et al., 2006). The results of the parameters are: $\rho_0 = 3.227\,\mathrm{g/cm^3}$, $\lambda_0 = 95.153\,\mathrm{GPa}$, $\mu_0 = 195.024\,\mathrm{GPa}$ and $p_0 = -5.2\,\mathrm{GPa}$, $\beta = 26.356^\circ$, $q_0 = 7.5\,\mathrm{GPa}$, $\alpha = 2.4$, $B = 4.52$.

Model prediction of longitudinal stress response is obtained and the gauge resistance change is calculated by Eq. (6.15). The result is shown in Figure 6.7 with the comparison of the experimental data. The simulation result of gauge resistance change compares the experimental data well when the calibrated parameter α is equal to –0.91.

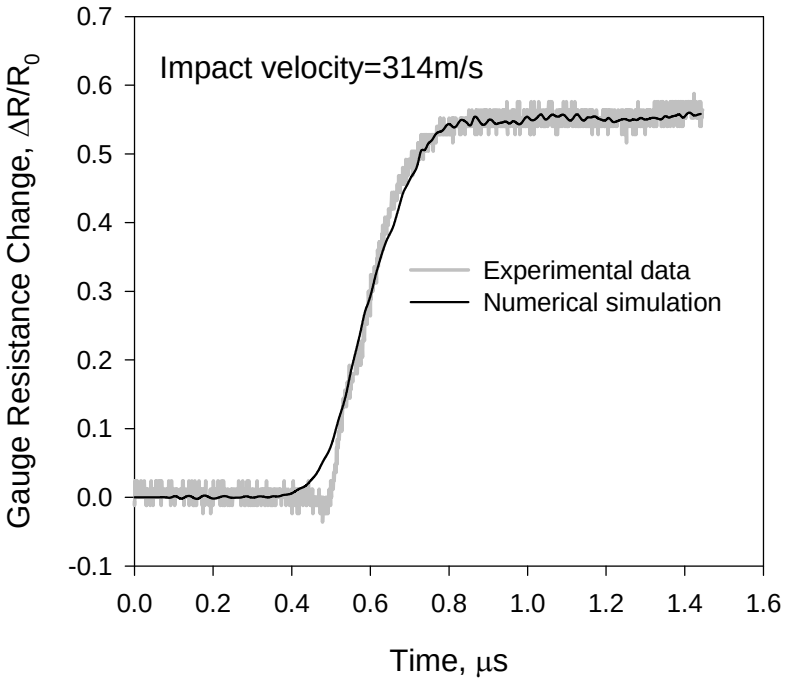

Figure 6.7: Comparison of computed and measured resistance change of a longitudinal manganin gauge in SiC-N sample under shock compression.

6.4.2 The Results of Longitudinal Gauge Simulation

The numerical simulations of longitudinal gauge experiment are carried out. Model predictions of longitudinal stress response at four impact velocity: V_0 = 314 m/s,

600 m/s, 1250 m/s and 1800 m/s are plotted in Figure 6.8(a), and the relative gauge resistance changes calculated by Eq.6.15 are shown in Figure 6.8(b).

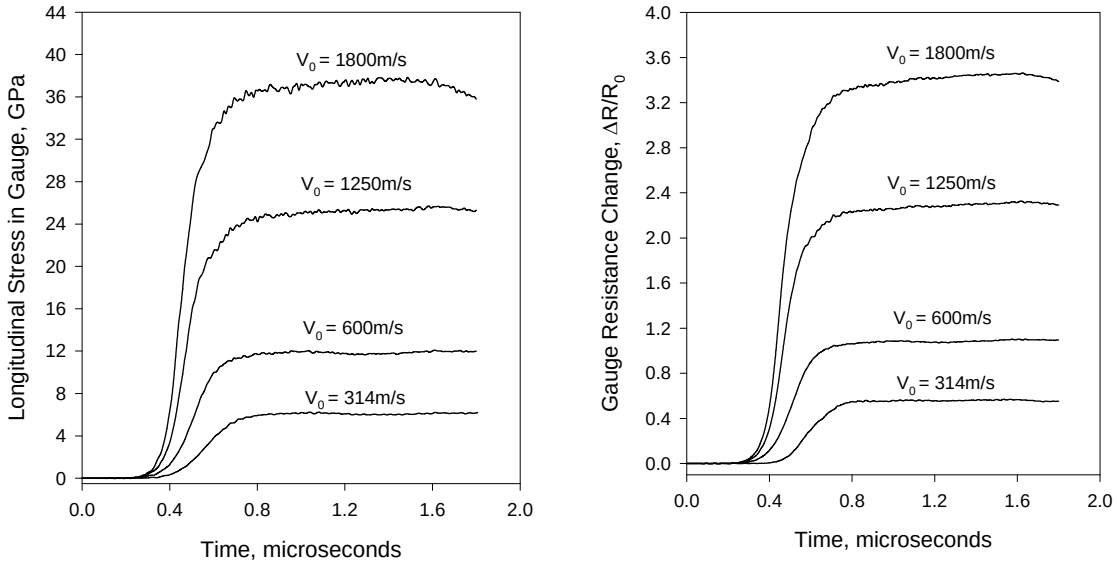

(a) Longitudinal stresses (b) Gauge resistance changes

Figure 6.8: The results for longitudinal gauge experiment simulations.

6.4.3 The Results of Lateral Gauge Simulation

The numerical simulations of lateral gauge experiment are carried out. Model predictions of loateral stress response at three impact velocities (V_0 = 314 m/s, 600 m/s and 1250 m/s) are plotted in Figure 6.9(a), and the relative gauge resistance changes calculated by Eq.(6.15) are shown in Figure 6.9(b).The peak lateral stress in gauge, corresponding uniaxial longitudinal stress and lateral stress are summarized in Table 6.1.

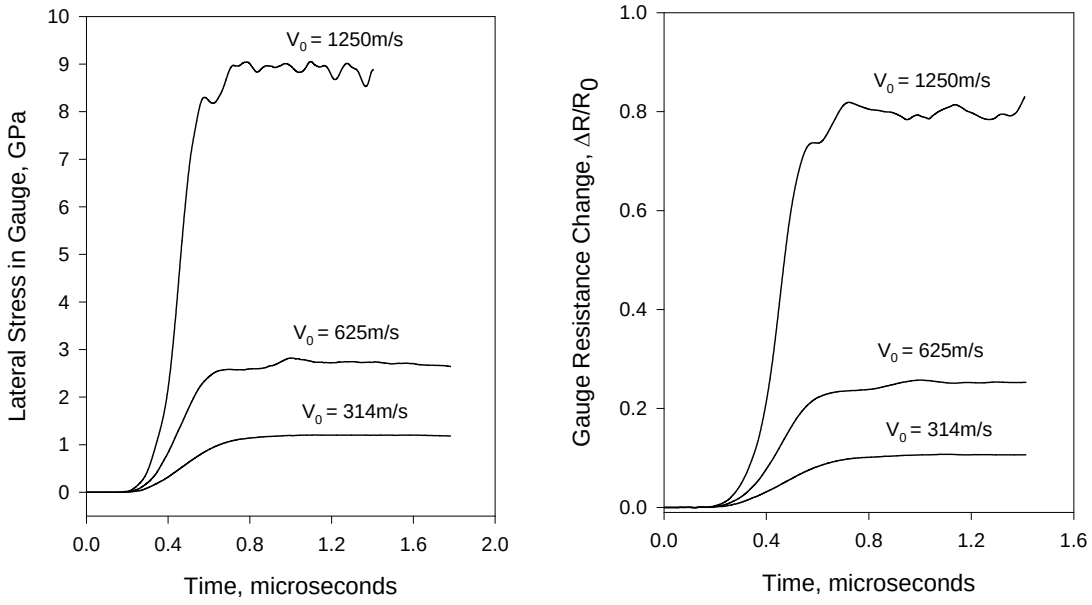

(a) The lateral stresses (b) Gauge resistance changes

Figure 6.9: The results for lateral gauge experiment simulations.

Table 6.1: Summary of lateral gauge experimental simulations

Simulation number	Impact Velocity (m/s)	Lateral stress in gauge(GPa) (peak)	$\Delta R / R_0$ (peak)	Corresponding uniaxial longitudinal stress(GPa) (peak)	Corresponding uniaxial lateral stress(GPa) (peak)
1	314	1.20	0.1074	6.36	1.29
2	625	2.82	0.2574	12.55	2.74
3	1250	9.04	0.8302	25.65	8.73

At the peak stress state, resistance change values are obtained from more gauge simulations at different impact velocities, shown in Figure 6.10 with the different peak stress levels of longitudinal and lateral stresses. To get the relationship of resistance change and stress response, for high-strength ceramics, a least square fit is needed to obtain the calibration curve (Feng et al., 1997). The fit curves are also shown in Figure 6.10 and the equations for manganin foil gauge calibration are obtained by:

For longitudinal stress simulation,

$$\frac{\Delta R}{R_0} = 9.360\times10^{-2}\sigma_z - 2.631\times10^{-4}\sigma_z^2, \tag{6.16a}$$

and for longitudinal stress simulation,

$$\frac{\Delta R}{R_0} = 7.558\times10^{-2}\sigma_z + 4.014\times10^{-4}\sigma_z^2. \tag{6.16b}$$

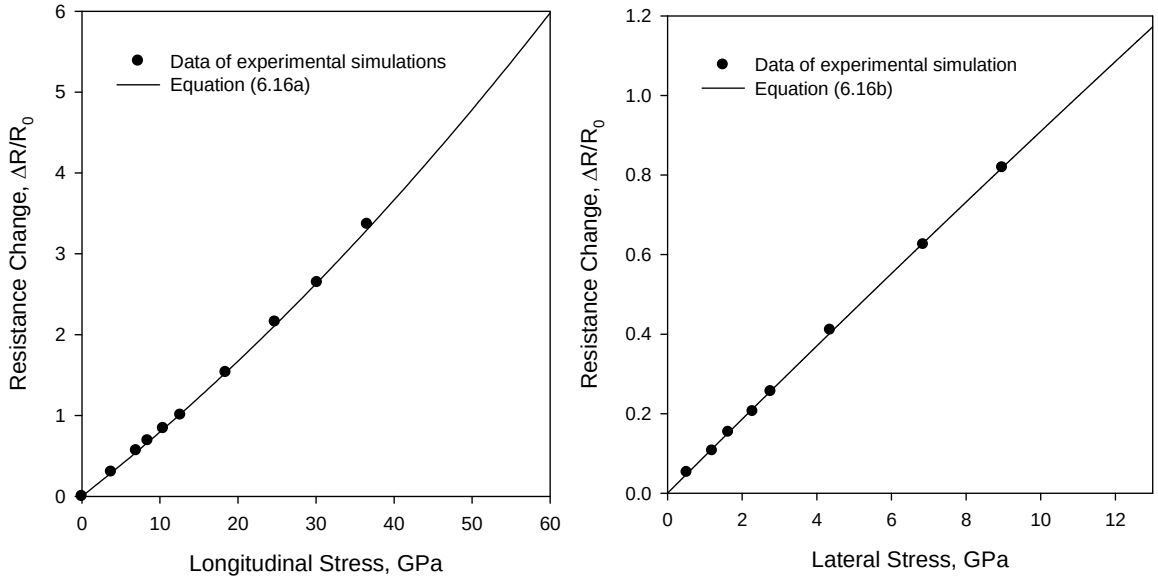

Figure 6.10: Calibrations of the manganin gauge response.

6.5 Summary

In this chapter, a new finite element piezoresistance model for interpreting the measurement of a commercial manganin stress gauge embedded in a plate impact target is developed and numerical method to calculate the gauge resistance change is derivate and the relative gauge resistance changes for longitudinal and lateral stress response are obtained.

The configurations of longitudinal and lateral gauge simulation including ceramics sample – manganin gauge assembly are designed. 3-D plate impact FE models for the configurations of longitudinal and lateral gauge experiments are developed. The sample – gauge assembly is modeled as ABAQUS/Explicit Tie, and the interaction of impact and target is modeled as ABAQUS/Explicit Surface to Surface Contact. The material models of copper, epoxy and manganin gauge are employed as hydrodynamic models. The 3-D FE models and material models are implemented into ABAQUS /Explicit code for FE analysis.

Calibrated with the longitudinal gauge measurements obtained in the shock-compressed SiC-N. From the model simulations, the calibrations for the gauge in both the longitudinal and lateral configurations are obtained. This enables the determination of ceramic shock strength directly from the gauge measurements in the two configurations. Although this study is on ceramic SiC-N material, the simulation results of longitudinal and lateral stresses response provide the important information for performing the gauge experiments. The configurations of longitudinal and lateral gauge experiments are recommended for the experiments on AlON.

CHAPTER 7

CONCLUSIONS

In this research, a computational polycrystal modeling technique, which combines Voroni polycrystal simulation with finite element analysis, has been applied to study the effects of polycrystalline microstructure, crystal anisotropy, porosity, and their interactions with microscopic deformation/damage mechanisms on the responses of several polycrystalline ceramics under shock compression and to extract their strength properties in conjunction with the available shock compression data or with macroscopic effective property modeling and simulations of the related plate impact shock wave experiments.

Square-plate Voronoi polycrystal-finite element (VP-FE) models with 200 2-D grains or cubic VP-FE models with 600 3-D grains are generated for topologically accurate microstructure modeling. It is shown that good statistical representations can be achieved with these VP-FE models. A concurrent multiscale modeling technique is employed to examine the loading range, over which the volume-averaged responses of the mesoscopic VP-FE models to prescribed uniform boundary displacement or traction are good representations of the macroscopic material behavior. It is found that accurate

representations can be achieved for shock stresses up to twice the Hugoniot elastic limit (HEL).

The mesoscopic VP-FE models have been applied to examine the roles of intragranular microplasticity and deformation twinning, intergranular microdamage, and voids in the inelastic deformations and shock strengths of two polycrystalline α–phase aluminum oxides, Lucalox (99.9% pure and dense) and AD995 (99.5% pure and 97% dense). For Lucalox, 3-D analysis with a 600-grain cubic VP-FE model and material models considering nonlinear elasticity and crystal plasticity by the activation of prismatic slip or combined prismatic (primary) and basal (secondary) slips has been performed. The results show that: (1) Microplasticity by prismatic slip alone is adequate only near the HEL but underestimates post-HEL softening; (2) Model prediction by combined prismatic and basal slips compares well with the experimental data up to a shock stress of 20 GPa or about 2.2 times the HEL.

For AD995, 2-D analysis with porous VP-FE models has been performed to investigate the causes for observed signification reductions in HEL and post-HEL strength of the shocked material and to understand the difference between the inelastic deformation of shocked AD995 and that of shocked Lucalox. The studies performed and the results are as follows:

(1) Three types of 2-D porous VP-FE models have been constructed and examined for their performances and mesh dependencies for modeling and analysis of microplasticity-driven void collapsing in AD995 under shock compression. Numerical results of void modeling study show: (a) Triangular voids are so rigid to be collapsed and

may be inadequate for intense plastic deformation near voids, and the longitudinal stress response of porous polycrystal model with 3% triangular voids displays almost the same behavior as that of Lucalox; (b) Random-shaped voids are found to be the most advantageous, providing relative ease in construction, more realistic void shape modeling, and good ability for capturing void collapsing process, and the longitudinal stress response of porous polycrystal model with 3% random-shaped voids displays much more softened behavior than that of Lucalox; (c) Good statistical representation is achieved with the porous polycrystal model with 3% random-shaped voids.

(2) The results of the studies to examine the roles of glassy grain boundaries and voids in the inelastic deformation and strength of shocked AD995 show that: (a) Weaker grain boundary cannot explain the observed HEL and post-HEL response of shocked AD995; (b) It is the voids in AD995 that responsible for its lower shock strength than Lucalox; (c) Microplasticity becomes easier to initiate near the voids, evolves with the deformation band, and leads to void collapsing.

(3) Numerical results for various microplasticity models show that: (a) Model prediction based on prismatic primary slip at $\tau_{cp} = 2.7$ GPa and basal secondary slip at $\tau_{cb} = 3.3$ GPa cannot match the experimental data; (b) Model prediction based both basal deformation twinning at $\tau_{ctw} = 2.7$ GPa and prismatic slip at $\tau_{cp} = 3.3$ GPa can match the experimental data up to HEL, but cannot match the post-HEL data; (c) The macroscopic shock response of AD995 is well captured by model prediction based on basal deformation twinning at $\tau_{ctw} = 2.0$ GPa and prismatic slip at $\tau_{cp} = 2.4$ GPa for shock

stresses up to 14 GPa or about twice the HEL; (d) The evolution of effective plasticity strain based on both basal deformation twinning and prismatic slip with lower thresholds becomes rapid both for intensity and for volume of participating material when shocked to about 12 GPa, which can explain the abrupt post-HEL softening observed for AD995.

Both macroscopic effective strength modeling and mesoscopic analyses based of 3-D VP-FE models have been performed for polycrystalline aluminum oxynitride (AlON), a newly developed transparent polycrystalline ceramic. First, wave profile simulations with a macroscopically homogeneous model considering compression-dependent nonlinear elasticity and pressure-dependent effective strength have been carried out to interpret a series of plate impact experiments on AlON. The results show that: (1) The simulated wave profiles with the optimized model parameters compare very well with the experimental measurements; (2) The material has a HEL of 10.37 GPa and retains post-HEL effective strength for the range of shock compression examined (up to 93 GPa shock stress) contrary to the shock strength loss results from the previous jump condition analysis for the same experiments (Thornhill et al., 2005); (3) The relationship between the shock velocity U_s and the particle velocity u_p is $U_s = 7.564 + 0.857u_p$. The relationship between the longitudinal stress and the particle velocity is also obtained.

Next, 3-D mesoscopic analyses with a 600-grain cubic VP-FE model have been conducted to extract the crystal elasticity and crystal plasticity properties of AlON. The numerical results show that: (1) Ambient crystal elasticity constants of $C_{11} = 412.0\,\text{GPa}$, $C_{12} = 123.0\,\text{GPa}$, and $C_{44} = 118.0\,\text{GPa}$ yield the best match to the elastic modulii of polycrystalline AlON determined by the ultrasonic measurements; (2) The shock

response and effective shock strength of AlON can be very well described by the combination compression-dependent dilatational elasticity with a stiffening parameter of $A = 4.3$ and $\{111\}\langle 110\rangle$ crystal slip at a CRSS value of $\tau_c = 3.35$ GPa.

Finally, a new finite element piezoresistance model for interpreting the measurement of a commercial manganin stress gauge embedded in a plate impact target has been developed and calibrated with the longitudinal gauge measurements obtained in a shock-compressed polycrystalline α-6H silicon carbide (SiC-N). From the model simulations, the calibrations for the gauge in both the longitudinal and lateral configurations are obtained. This enables the determination of ceramic shock strength directly from the gauge measurements in the two configurations. Although the calibration is done for SiC-N material, the method is expected to be useful for measuring the longitudinal and lateral stresses of other similar polycrystalline ceramics. The simulation results also provide important information for performing the gauge experiment.

BIBLOGRAPHY

ABAQUS Manuals, V6.5~6.9, 2005~2009.

Addessio, F.L. and Johnson, J.N., 1990. A constitutive model for the dynamic response of brittle materials. Journal of Applied Physics, Vol. 67, 3275-3266.

Alexander, C.S., Reinhart,W.D. and Thornhill, T.F., 2010. Armor options: a comparison of the dynamic response of materials in the aluminum oxide-aluminum nitride family. International Journal of Applied Ceramic Technology, Vol. 7, 587-594.

Anand, L. and Kothari, M., 1996. A computational procedure for rate-independent crystal plasticity. Journal of the Mechanics and Physics of Solids, Vol. 44, 525-558.

Asaro, R.J., 1983. Crystal plasticity. Journal of Applied Mechanics, Vol. 50, 921-934.

Asay, J. R., Chhabildas, L. C., Kerley, G. 1. and Trucano, T .G., 1985. High Pressure Strength of Shocked Aluminum. Shock Waves in Condensed Matter, Gupta, Y.M., eds., 145-149.

Castaing, J., Cadoz, J. and Kirby, S.H., 1981. Prismatic slip of Al_2O_3 single crystals below 1000°C in compression under hydrostatic pressure. Journal of the American Ceramic Society, Vol. 64, 504-511.

Castaing, J., He, A. and Heuer, A. H., 2003. Deformation of sappjire by basal slip and basal twinning below 700°C. Philosophical Magazine, Vol. 84, 1113-1125.

Cazamias, J. U., Fiske, P. S. and Bless,S. J., 2001. The Hugoniot Elastic Limit of AlON. Shock Compression Condens. Matter, Vol. 1, 767–770.

Cazamias, J. U., Fiske, P. S. and Bless,S. J., 2006. Shock properities of AlON: Fundamental issure and applications of shock-wave and high-strain-rate phenomena, (editors: staudhammer, K.p., Mutt, L.E. and Mcyers, M.A.) @2001 Elsevier Science LTd. 181-188.

Chen, M. W., McCauley, J. W., Dandekar, D. P. and Bourne, N. K., 2006. Dynamic plasticity and failure of high purity alumina under shock loading. Nature Material, Vol 5, 614–618.

Dandekar, D.P. and Bartkowski, P., 1994. Shock response of AD995 alumina. AIP Conference Proceedings, No. 309, 733-736.

Daridon, L., Oussouaddi, O. and Ahzi, S., 2004. Influence of the material constitutive models on the adiabatic shear band spacing: MTS, power law and Johnson-Cook models. International Journal of Solids and Structures, Vol. 41, 3109-3124.

Feng, R. and Gupta, Y.M., 1994. Material model for 6061-T6 Aluminum for use in shock wave experiments and calculations. Shock Dynamics Center internal Report 94-01.

Feng, R. and Gupta, Y.M., 1994. Material model for OFHC copper for use in shock wave experiments and calculations. Shock Dynamics Center internal Report 94-02.

Feng, R. and Gupta, Y.M., 1994. Material model for PMMA for use in shock wave experiments and calculations. Shock Dynamics Center internal Report 94-04.

Feng, R. and Gupta, Y.M., 1996. Material model for Sapphire –quartz, Lithium Fluoride and Fused Silica for use in shock wave experiments and calculations. Shock Dynamics Center internal Report 94-xx.

Feng, R., Gupta, Y.M. and Wong, M.K.W., 1997. Dynamic analysis of the response of lateral piezoresistance gauges in shocked ceramics. Journal of Applied Physics, Vol. 82, 2845-2854.

Feng, R., Raiser, G.F. and Gupta, Y.M., 1996. Shock response of polycrystalline silicon carbibe undergoing inelastic deformation. Journal of Applied Physics, Vol. 79, 1378-1387.

Feng, R., Raiser, G.F., and Gupta, Y.M., 1998. Material strength and inelastic deformation of silicon carbide under shock wave compression. Journal of Applied Physics, Vol. 83, 79-86.

Frank R., and Nunes N., 1996. Theory of crystal dislocations. Publisher Clarendon P. The University of California.

Ghosh, S., Nowak, Z. and Lee, K., 1997. Quantitative characterization and modeling of composite microstructures by Voronoi cells. Acta Metallurgica, Vol. 45, 2215-2234.

Grady, D. E. and Moody, R. L., 1996. Shock Compression Profiles in Ceramics, Sandia National Laboratories Report, SAND96-0551.

Grady, D. E. 1995. Dynamic Properties of Ceramic Materials. Sandia National Laboratories Report, SAND88-3266.

Graham, E. K., Munly, W. C., McCauley, J. W. and Corbin, N. D., 1988. Elastic properties of polycrystalline aluminum oxynitride spinel and their dependence on pressure, Temperature, and Composition. Journal of the American Ceramic Socirty, Vol. 71, 807–812 .

Gust, W.H. and Royce, E.B., 1971. Dynamic yield strengths of B_4C, BeO, and Al_2O_3 ceramics. Journal of Applied Physics, Vol. 42, 276-295.

Hankey, R.E. and Schuele, D.E., 1970. Third-order elastic constants of Al_2O_3. The Journal of Acoustical Society of America, Vol. 48, 190-202.

Heuer, A.H., Firestone, R.F., Snow, J.D. and Tullis, J.D., 1971. In Proceedings of the 2nd International Conference on Strength of Metals and Alloys, Vol. III. The American Society for Metals, Metals Park, OH, 1165-1169.

Hirth, J.P. and Lothe, J., 1992. Theory of dislocations, reprint ed. Krieger Publishing Company, Malabar.

HyperMesh Manuals, V5.1~8.0, 2003~2007.

Jiao, T., Li, Y. and Ramesh, K. T., 2004. High rate response and dynamic failure of structural ceramics. Applied Ceramic Technology, Vol. 1 243–253.

Johnson, G.R., Holmquist, T.J. Lankford, J., Anderson, C.E. and Walker, J., 1990. A computational constitutive model and test data for ceramics subjected to large strain, high

strain rates, and high pressures. Final technical report for Optional Task 1, Contract DE-AC04-87AL-42550, Los Alamos National Laboratory, Los Alamos, NM.

Johnson, G.R. and Holmquist, T.J., 1994. An improved computational constitutive model for brittle materials. In High Pressure Science and Technology-1993 (Edited by S.C. Schmidt, J.W. Shaner, G.A. Samara and M. Ross), AIP, New York, 981-984.

Kipp, M.E. and Grady, D.E., 1989. Shock compression and release in high-strength ceramics. Sandia Report N0. SAN89-1461, Sandia National Laboratories, Albuquerque, NM.

Kumar, S. and Kurtz, S.K., 1994. Simulation of material microstructure using a 3D Voronoi tessellation: Calculation of effective thermal expansion coefficient of polycrystalline materials. Acta Metallurgica, Vol. 42, 3917-3927.

Longy, F. and Cagnoux, J., 1989. Plasticity and microcracking in shock-loaded alumina. Journal of the American Ceramic Society, Vol. 72, 971-979.

Loret, B. and Prevost, J.H., 1986. Accurate numerical solutions for Drucker-Prager elastic-plastic models. Computer Methods in Applied Mechanics and Engineering, Vol. 54, 259-277.

McCauley, J. W., 2001. Structure and properties of Aluminum Nitride and AlON ceramics. in Elsevier's Encyclopedia of Materials: Science and Technology, Edited by J. W. McCauley. Elsevier Science Ltd., Amsterdam, 2001, 127–132.

Munson, D.E. and Lawrence, R.J., 1979. Dynamic deformation of polycrystalline alumina. Journal of Applied Physics, Vol. 50, 6272-6282.

Paliwal, B., Ramesh, K.T., McCauley, J.W. and Chen, M., 2008. Dynamic compressive failure of AlON under controlled planar confinement. Journal of the American Ceramic Socirty, Vol. 91, 3619-3629.

Paliwal, B., Ramesh, K.T. and McCauley, J.W. 2006. Direct observation of the dynamic compressive failure of a transparent polycrystalline ceramic (AlON). Journal of the American Ceramic Socirty, Vol. 89, 2128–2133.

Pirouz, P., Lawlor, B.F., Geipel, T., Heuer, A.H. and LagerLof, K.P.D., 1994. On basal slip and basal twinning in sapphire-II. A new model of basal twinning. Acta Materialia, Vol. 44, 2153-2164.

Reinhart, W. D., Chhabildas, L.C., Grady, D.E. and Mahsimo, T., 2002. Shock Compression and Release Properties of Coors AD995 Alumina. Ceramic armor materials by design, Vol. 134, 233–247.

W.D. Reinhart, Shock compression and release properties of Coors AD995 Alumina, Ceramic armor materials by design. The American Ceramics Society (2002) p. 233–47.

Reinhart, W. D. and Chhabildas, L. C., 2003. Strength properties of Coors AD995 alumina in the shocked state. International Journal of Impact Engineering, Vol. 29, 601–619.

Salem, A.A., Kalidindi, S.R. and Semiatin, S.L., 2005. Strain hardening due to deformation twinning in α–titanium: Constitutive relations and crystal-plasticity modeling. Acta Materialia, Vol.53, 3495-3502.

Thornhill, T.F., Voger, T.J., Reinhart, W.D. and Chhabildas, L.C., 2005. Polycrystalline aluminum oxynitride hugoniot and optical Properties, Shock Compression of Condensed Matter-2005, AIP Conference Proceedings, 845, 143-146.

Viechnicki, D.J., Slavin, M.J. and Kliman M.I., 1991. Development and current status of armor ceramics. Ceramic Bulletin, Vol. 70, 1035-1039.

Volger, T.J., Reinhart, W.D., Chhabildas, L.C. and Dandekar, D.P., 2006. Hugoniot and strength behavior of silicon carbide. Journal of Applied Physics, Vol.99, 023512(1-15).

Xue, S., 2003. Polycrytal modeling and micromechanical analysis of ceramics. Master Thesis. University of Nebraska-Linclon.

Yuan, G., Feng, R. and Gupta, Y.M., 2001. Compression and shear wave measurements to characterize the shocked state in silicon carbide. Journal of Applied Physics, Vol. 89, 5372-5380.

Zhang, D., 2005. High-pressure deformation and failure of polycrystalline ceramics. Ph.D dissertation. University of Nebraska-Linclon.

Zhang, D. and Feng, R., 2005. Polycrystal modeling to determine the strengths of shocked ceramics. Shock Compression of Condensed Matter-2005, AIP Conference Proceedings, 845, 377-380.

Zhang, K.S., Wu, M.S. and Feng, R., 2005. Simulation of microplasticity-induced deformation in uniaxially strained ceramics by 3-D Voronoi polycrystal modeling. International Journal of Plasticity, Vol. 21, 801-834.

APPENDICES

A-1 The algorithm for constructing polycrystal model

The algorithm for constructing a 3-D Voronoi polycrystal in a unit cube is as follows:

1. Generate N "controlled" random points in a unit cube, where "controlled" means that a newly generated point is accepted only if the distance between the point and each of the other existing points is not less than the allowable minimum distance. All of the permissible points are regarded as the Voronoi cell nuclei.

2. Select a radius r to define the size of local search sphere S, where r is a parameter determined through test.

3. Draw a line connecting the *i*th nucleus N_i, where i = 1, 2, 3, … , N, with any other nucleus in the sphere S centered at N_i. Suppose there are M points (nuclei) besides N_i in the sphere S, therefore, M lines are obtained ($M < N$). For each of these lines, construct a perpendicular plane bisecting the line so that M planes are obtained. In addition, the six planes of the unit cube are added into the set of planes.

4. Find the intersection point for each combination of three planes belonging to the set, say, point P.

5. Compare the values of D_{ip} with D_{jp} where D_{ip} and D_{jp} denote, respectively, the distance between N_i and P and that between P and N_j ($j = 1, 2, \ldots, M$, $j \neq i$). If D_{ip} is smaller than all of D_{jp}, then, P is a vertex of the Voronoi cell associated with N_i. In addition, the three planes intersect at P are the planes containing the three faces of that cell. Otherwise, P is discarded and the search goes on. In this way, all of the vertices and face planes of the cell are found. Let the number of vertices and that of face planes of the *i*th cell be V_i and F_i, respectively ($i = 1, 2, \ldots, N$).

6. Repeat steps 3-5 for each of the other nuclei to determine the vertices and face planes associated with each of the N cells in the unit cube.

7. Sequence all vertices on each face plane to define each edge of the face and thus the face itself for each cell. Let the number of edges of the *i*th cell be E_i ($i = 1, 2, \ldots, N$).

8. Check whether the following Eqs. (2.1) and (2.2) are satisfied by V_i, F_i and E_i ($i = 1, 2, \ldots, N$).

Any cell in a 3-D Voronoi tessellation satisfies the Euler's criterion (Wu and Guo, 2000)

$$V - E + F = 2 \tag{2.1}$$

and the relation

$$V = 2F - 4, \tag{2.2}$$

where V, E, and F denote respectively the number of vertices, edges, and faces associated with the cell.

9. A microstructure-preserving numerical mesh is laid, which is described in Section 2.2.2.

10. Assign randomly selected crystallographic orientation to each of the cells.

After the above steps, a cubic Voronoi polycrystal model with microstructure-preserving numerical mesh is constructed. When the FE method is used for numerical solution, the model is termed as the Voronoi polycrystal-finite element (VP-FE) model.

The algorithm for constructing square (2-D) Voronoi polycrystal model is similar to that for the 3-D model. The difference is that all planes degenerate to lines and that each vertex is obtained from line intersection.

A-2 The solution procedure and iteration scheme of crystal plasticity model.

Let left superscripts "t" and "$t+\Delta t$" denote the quantities associated with the material configurations before and after an infinitesimally small time increment, respectively. Then, Eq. (2.3) can be discretized in time as (Hughes and Winget, 1980; ABAQUS Manual, 2004)

$$^{t+\Delta t}\boldsymbol{\sigma} = {}^{t}\boldsymbol{\sigma} + \mathbf{C} : (\Delta\boldsymbol{\varepsilon} - \Delta\boldsymbol{\varepsilon}^{p}), \tag{2.12}$$

with

$$^{t}\boldsymbol{\sigma} = \Delta\mathbf{R}\,{}^{t}\boldsymbol{\sigma}'\Delta\mathbf{R}^{T}, \tag{2.13}$$

and

$$\Delta\mathbf{R} = \left(\mathbf{I} - \Delta\boldsymbol{\omega}/2\right)^{-1} \cdot \left(\mathbf{I} + \Delta\boldsymbol{\omega}/2\right), \tag{2.14}$$

where $^{t}\boldsymbol{\sigma}'$ is the stress at time t but defined with respect to the previous local crystallographic base, and superscript T represents transpose operation. Equations (2.13) and (2.14) transform the stress at time t from the previous crystallographic base to the current one. Plastic strain increment can be calculated from Eq. (2.5) as

$$\Delta\boldsymbol{\varepsilon}^{p} = \sum_{\alpha=1}^{n} \mathbf{P}^{(\alpha)} \Delta\gamma^{(\alpha)}. \tag{2.15}$$

Therefore, Eq. (2.12) can be rewritten as

$$^{t+\Delta t}\boldsymbol{\sigma} = {}^{t}\boldsymbol{\sigma} + \mathbf{C} : \left(\Delta\boldsymbol{\varepsilon} - \sum_{\alpha=1}^{n} \mathbf{P}^{(\alpha)} \Delta\gamma^{(\alpha)}\right). \tag{2.16}$$

Shear strain increment $\Delta\gamma^{(\alpha)}$ can be calculated using a control parameter η in the range of (0, 1] as

$$\Delta\gamma^{(\alpha)} = [(1-\eta)^{t}\dot{\gamma}^{(\alpha)} + \eta^{t+\Delta t}\dot{\gamma}^{(\alpha)}]\Delta t\,, \tag{2.17}$$

with
$$^{t}\dot{\gamma}^{(\alpha)} = \dot{\gamma}_0\,\mathrm{sgn}(^{t}\tau^{(\alpha)})\left|\frac{^{t}\tau^{(\alpha)}}{^{t}g^{(\alpha)}}\right|^{k}, \tag{2.18}$$

and
$$^{t+\Delta t}\dot{\gamma}^{(\alpha)} = \dot{\gamma}_0\,\mathrm{sgn}(^{t+\Delta t}\tau^{(\alpha)})\left|\frac{^{t+\Delta t}\tau^{(\alpha)}}{^{t+\Delta t}g^{(\alpha)}}\right|^{k}. \tag{2.19}$$

Combining Eqs. (2.16), (2.17) and (2.19), the following stress-based iterative equation can be obtained to solve the stress for a given time increment:

$$^{t+\Delta t}\boldsymbol{\sigma} = {}^{t}\boldsymbol{\sigma} + \mathbf{C} : \left\{\Delta\boldsymbol{\varepsilon} - \Delta t\left[(1-\eta)\sum_{\alpha=1}^{n}\mathbf{P}^{(\alpha)}\,{}^{t}\dot{\gamma}^{(\alpha)}\right.\right.$$

$$\left.\left. + \eta\dot{\gamma}_0\sum_{\alpha=1}^{n}\mathbf{P}^{(\alpha)}\,\mathrm{sgn}(^{t+\Delta t}\tau^{(\alpha)})\left(\frac{\left|\mathbf{P}^{(\alpha)} : {}^{t+\Delta t}\boldsymbol{\sigma}\right|}{^{t+\Delta t}g^{(\alpha)}}\right)^{k}\right]\right\}. \tag{2.20}$$

For the convenience of implementing the Newton-Raphson iteration algorithm in ABAQUS/Standard and ABAQUS/Explicit, Eq. (2.20) is recasted into the matrix form:

$$\mathbf{f} = {}^{t+\Delta t}\hat{\boldsymbol{\sigma}} + \lambda_1\hat{\mathbf{C}}\left[\sum_{\alpha=1}^{n}\hat{\mathbf{P}}^{(\alpha)}\lambda_2^{(\alpha)}(\hat{\mathbf{P}}^{(\alpha)T}\,{}^{t+\Delta t}\hat{\boldsymbol{\sigma}})\left|\lambda_2^{(\alpha)}\hat{\mathbf{P}}^{(\alpha)T}\,{}^{t+\Delta t}\hat{\boldsymbol{\sigma}}\right|^{k-1}\right] - \mathbf{r} = \mathbf{0}\,, \tag{2.21}$$

with
$$\lambda_1 = \eta\dot{\gamma}_0\Delta t\,,\ \lambda_2^{(\alpha)} = 1/{}^{t}g^{(\alpha)}\,, \tag{2.22}$$

and
$$\mathbf{r} = {}^{t}\hat{\boldsymbol{\sigma}} + \hat{\mathbf{C}}\left[\Delta\hat{\boldsymbol{\varepsilon}} - (1-\eta)\Delta t\sum_{\alpha=1}^{n}\hat{\mathbf{P}}^{(\alpha)}\,{}^{t}\dot{\gamma}^{(\alpha)}\right], \tag{2.23}$$

where $\hat{\mathbf{C}}$ is the 6 × 6 matrix of tangent elastic constants of the crystal as described in Eq. (2.4), and $\hat{\mathbf{P}}^{(\alpha)}$, $\hat{\boldsymbol{\sigma}}$ and $\Delta\hat{\boldsymbol{\varepsilon}}$ are 6 × 1 matrices, given by

$$\hat{\mathbf{C}} = \begin{bmatrix} C_{1111} & C_{1122} & C_{1133} & C_{1112} & C_{1113} & C_{1123} \\ & C_{2222} & C_{2233} & C_{2212} & C_{2213} & C_{2223} \\ & & C_{3333} & C_{3312} & C_{3313} & C_{3323} \\ & & & C_{1212} & C_{1213} & C_{1223} \\ & \textit{sym.} & & & C_{1313} & C_{1323} \\ & & & & & C_{2323} \end{bmatrix}, \tag{2.24}$$

and

$$\hat{\mathbf{P}}^{(\alpha)} = \begin{Bmatrix} P_{11} \\ P_{22} \\ P_{33} \\ 2P_{12} \\ 2P_{13} \\ 2P_{23} \end{Bmatrix}, \ \hat{\boldsymbol{\sigma}} = \begin{Bmatrix} \sigma_{11} \\ \sigma_{22} \\ \sigma_{33} \\ \sigma_{12} \\ \sigma_{13} \\ \sigma_{23} \end{Bmatrix}, \ \Delta\hat{\boldsymbol{\varepsilon}} = \begin{Bmatrix} \Delta\varepsilon_{11} \\ \Delta\varepsilon_{22} \\ \Delta\varepsilon_{33} \\ 2\Delta\varepsilon_{12} \\ 2\Delta\varepsilon_{13} \\ 2\Delta\varepsilon_{23} \end{Bmatrix}. \tag{2.25}$$

The Newton-Raphson iteration can then be written as

$$\mathbf{f}\left({}^{t+\Delta t}\hat{\boldsymbol{\sigma}}^{m}\right) + \frac{\partial \mathbf{f}}{\partial\left({}^{t+\Delta t}\hat{\boldsymbol{\sigma}}^{m}\right)}\delta\left({}^{t+\Delta t}\hat{\boldsymbol{\sigma}}^{m}\right) = \mathbf{0}, \tag{2.26}$$

With $$\mathbf{f}\left({}^{t+\Delta t}\hat{\boldsymbol{\sigma}}^{m}\right) = {}^{t+\Delta t}\hat{\boldsymbol{\sigma}}^{m} + \lambda_1\hat{\mathbf{C}}\left[\sum_{\alpha=1}^{n}\hat{\mathbf{P}}^{(\alpha)}\lambda_2^{(\alpha)}(\hat{\mathbf{P}}^{(\alpha)T}\,{}^{t+\Delta t}\hat{\boldsymbol{\sigma}}^{m})\left|\lambda_2^{(\alpha)}\hat{\mathbf{P}}^{(\alpha)T}\,{}^{t+\Delta t}\hat{\boldsymbol{\sigma}}^{m}\right|^{k-1}\right], \tag{2.27}$$

and $$\frac{\partial \mathbf{f}}{\partial\left({}^{t+\Delta t}\hat{\boldsymbol{\sigma}}^{m}\right)} = \mathbf{I} + \lambda_1\hat{\mathbf{C}}\left[\sum_{\alpha=1}^{n}\hat{\mathbf{P}}^{(\alpha)}\left(k\left|\lambda_2^{(\alpha)}\hat{\mathbf{P}}^{(\alpha)T}\,{}^{t+\Delta t}\hat{\boldsymbol{\sigma}}^{m}\right|^{k-1}\lambda_2^{(\alpha)}\right)\hat{\mathbf{P}}^{(\alpha)T}\right], \tag{2.28}$$

where *m* is the index for iteration. Stress variation $\delta\left({}^{t+\Delta t}\hat{\boldsymbol{\sigma}}^{m}\right)$ is determined by solving Eq. (2.26), and the stress is updated as

$$ {}^{t+\Delta t}\hat{\boldsymbol{\sigma}}^{m+1} = {}^{t+\Delta t}\hat{\boldsymbol{\sigma}}^{m} + \delta\left({}^{t+\Delta t}\hat{\boldsymbol{\sigma}}^{m}\right). \tag{2.29} $$

Stress ${}^{t+\Delta t}\hat{\boldsymbol{\sigma}}$ iterates with the initial value of ${}^{t}\hat{\boldsymbol{\sigma}}$, and is assumed to converge when the absolute values of $\mathbf{f}\left({}^{t+\Delta t}\hat{\boldsymbol{\sigma}}^{m+1}\right)$ and $\delta\left({}^{t+\Delta t}\hat{\boldsymbol{\sigma}}^{m+1}\right)$ are less than very small positive values. Then the rate of shear strain can be updated using

$$ {}^{t+\Delta t}\dot{\gamma}^{(\alpha)} = \dot{\gamma}_0 \left(\lambda_2^{(\alpha)} \hat{\mathbf{P}}^{(\alpha)T}\, {}^{t+\Delta t}\hat{\boldsymbol{\sigma}}\right) \left|\lambda_2^{(\alpha)} \hat{\mathbf{P}}^{(\alpha)T}\, {}^{t+\Delta t}\hat{\boldsymbol{\sigma}}\right|^{k-1}. \tag{2.30} $$

Shear strain increment of α-slip system can be obtained by Eq. (2.17). Using Eq. (2.15), plastic strain increment with respect to current local crystallographic base is determined. Finally, $g^{(\alpha)}$ can be updated through

$$ {}^{t+\Delta t}g^{(\alpha)} = {}^{t}g^{(\alpha)} + \sum_{\beta=1}^{n} \int_{t}^{t+\Delta t} h_{\alpha\beta} \left| d\gamma^{(\beta)} \right|. \tag{2.31} $$

This iterative solution scheme is implemented in ABAQUS/Explicit through User-defined subroutine - VUMAT